INTERNATIONAL UNIVERSITY LIAISON INDONESIA (IULI)

HEAVY LIFT MOBILITY PLATFORM

Presented to 2023-2024 AIAA
Aircraft Design Competition

By
The Ravens Orion

May 12, 2024

Executive Summary

The worldwide logistics market had substantial growth, reaching a valuation of $5.4 trillion in 2023 [1]. Because aircraft facilitate the rapid transportation of commodities across international borders, cargo aircraft play a crucial role in the global economy. At present, the C-17 and C-5M are the two main cargo aircraft variants used by the United States Air Force (USAF). It is anticipated that both aircraft will continue to be in service well into the 2040s. However, it is imperative that these aircraft be replaced in order to avoid a capability gap. The next generation of cargo aircraft has to have improved features, like a bigger cargo bay that can hold greater payloads and more endurance for travel around the globe.

A proposed design intended to replace the C-17 and C-5M platforms is the BUING aircraft (Building Unity in Engineering Integrity). The vehicle is meant to meet three main mission profiles: the first is the ability to move three 71.2-ton M-1 Abrams tanks; the second is the ability to hold 48 463L pallets; and the third is the capability to carry up to 430 passengers. At maximum payload, this new Heavy-lift Aircraft (HLA) variant can reach a range of 3088 nautical miles (plus reserves).

The four Rolls-Royce Trent 1000 engines that power the BUING aircraft's propulsion system have a combined thrust of 1 440 000 N. With a total fuel capacity of 234,455 kg, the aircraft can accommodate heavy lifting and a long operational range. Utilizing cutting-edge aircraft technology, its design ensures efficiency and versatility in situations involving worldwide deployment while meeting the changing demands of military operations for strategic transport.

IMPORTANT

This report was crafted using LaTeX, with a font size of 11 points and double spacing for enhanced readability. For transparency and accessibility, all the files utilized in this project are publicly available for inspection through the following links:

- Manuscript: `https://tinyurl.com/24qj5zuz`.
- CAD: Airframe (`https://tinyurl.com/2b9kuceo`), Landing Gear (`https://tinyurl.com/2coujqho`), Cockpit (`https://tinyurl.com/24koyp77`), Seat (`https://tinyurl.com/254rw9fs`)
- Supporting files, e.g. XLFR5, OpenVSP, `https://tinyurl.com/246umrhe`.
- In house Python codes: `https://tinyurl.com/252yzsu4`.

Table 1: BUING Specification

Crew	4 (1 Pilot, 1 Co-pilot, 2 Loadmasters)
Dimensions	• Height: 10 918 mm (ground to top of fuselage), 17 287 mm (ground to top of vertical stabilizer) • Width: 74650 mm • Length: 81680 mm
Speed	• Maximum Speed : 476 kt • Total Endurance : 11 hours
Range	• Unrefueled Range: 5720 km • Ferry Range: 15014 km
Payload	• 3 M1A2 Abrams Main Battle Tanks (71,200 kg each) • 48 463L pallets (4,500 kg maximum payload) • One hundred (100) passengers or fully equipped troops/paratroops on a separate deck or compartment from the main cargo bay(s); and three hundred-thirty (330) troops on the main cargo deck bay(s).
Engines	4 x Rolls-Royce Trent-1000
Weight	• Empty Weight: 205,453 kg • MTOW: 550,453 kg
Fuel	Maximum Capacity 234,455 kg (291,763 m^3)
Service Ceiling	10274 m (Refer to climbing performance at 75% MTOW)
Takeoff Distance	2611 m BFL
Landing Distance	630 m (landing thrust at 10%) at BFL 3170 m
BFL	3170 m
Certifications	• FAA FAR 25 • MIL-SPECS applicable and DoD qualified
Production	Minimum 90

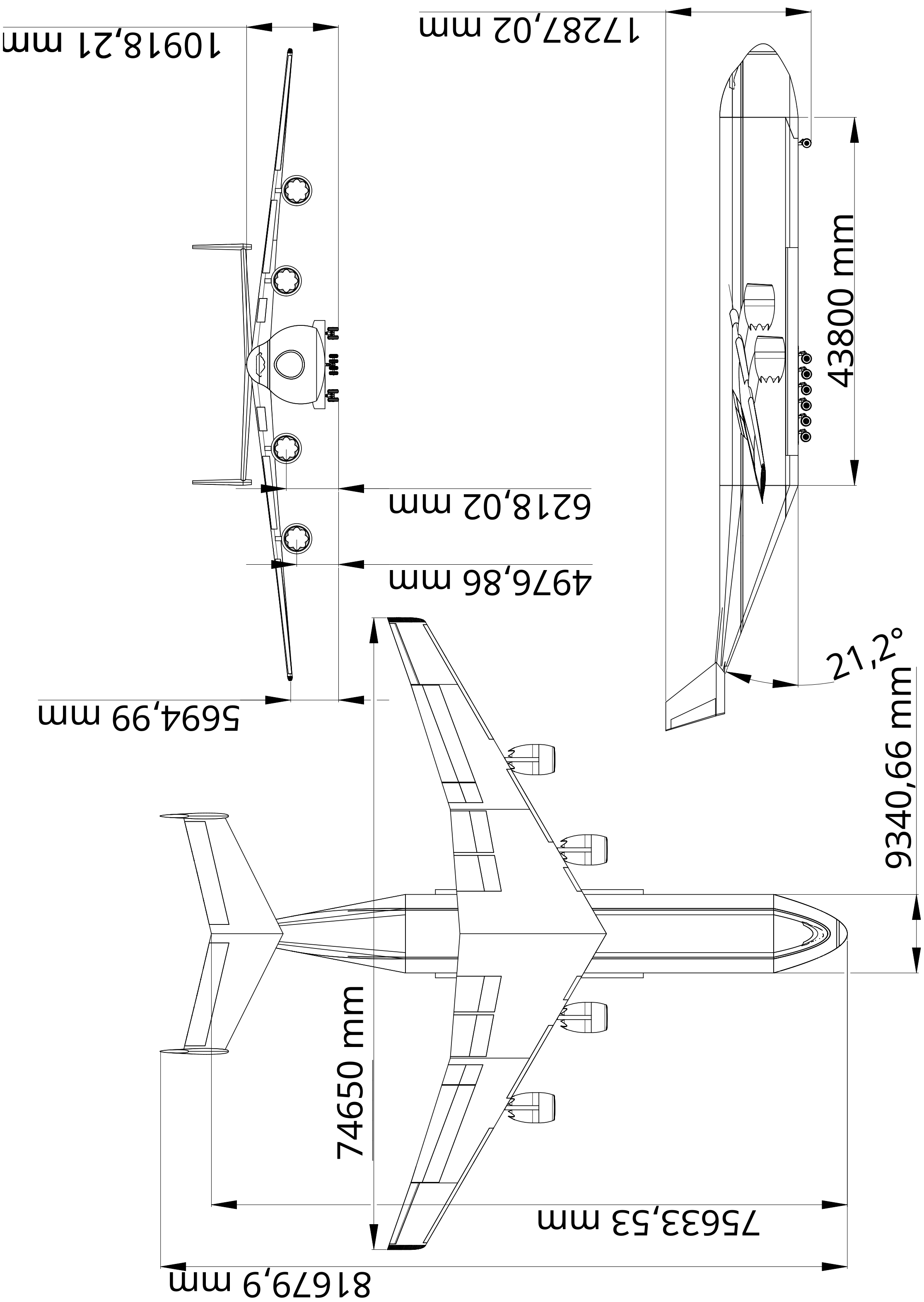

Figure 1: Three-view drawing of BUING

The Ravens Orion


Samuel Theofilus Tamonob
Team Lead
Stability & Control

AIAA Number : 1602282


Muhammad Rizky Permana
Co-Lead
Aero-Performance

AIAA Number : 1601470


Renggani Ghifari
Aero-Performance

AIAA Number : 1602523


M. Bimo Adjie Athallah
Structure

AIAA Number : 1538412


Odyseus Lorenzo
Structure

AIAA Number : 1602518


Patrick Kevin Rahangiar
Structure (Landing Gear)

AIAA Number : 1602584


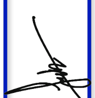

Eugenius Fabian Setia
Atmadja
Structure (Cockpit)

AIAA Number : 1603001


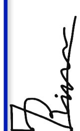

Richard Ilhami Reinida
Nayoan
Cost Analysis

AIAA Number : 1603300


Talal Mohamad Ali Bin Snkar
Propulsion

AIAA Number : 1603277

Triwanto Simanjuntak, PhD
Faculty Advisor

AIAA Number : 1345661

Dr. Eng. Ressa Octavianty
Project Advisor

AIAA Number : 1345663

Acknowledgements

This report paper represents as the pinnacle of our academic journey at International University Liaison Indonesia (IULI), and currently majoring in Aviation Engineering undergraduate program. We are grateful for the significant influence that education has had on us as we consider the time we spent as undergraduates. We are incredibly appreciative of it for giving us a lifelong passion for the quest for knowledge.

The constant support and knowledgeable direction we have received from the Aviation Engineering Department faculty members has greatly influenced our journey up to this point. We are grateful to them for their commitment and support.

We would like to express our deepest appreciation to Dr. Ressa Octavianty, and Dr. Triwanto Simanjuntak, for their remarkable mentorship during the BUING project's growth. Their insightful critiques and kind criticism have been tremendously beneficial in improving our design to professional standards. In addition, their insightful advice was essential in helping us overcome the obstacles we encountered and succeed. We are incredibly grateful for their generosity for their graciousness in sharing their expertise and experience, which has been crucial to our development and accomplishments.

TABLE OF CONTENTS

LIST OF FIGURES

LIST OF TABLES

CHAPTER 1 INTRODUCTION

1.1 Introduction

The United States Air Force (USAF) now operates two main platforms of strategic transport aircraft, the C-17 and the C-5M. Both aircraft are considered fully developed and mature platforms. But whereas the C-17 hasn't changed much from its basic configuration, the C-5M version has undergone a thorough redesign and refurbishment that makes use of 52 previous airframes. Even though both models are still viable today and will continue to be so far into the 2040s and beyond, it is evident that they must be replaced with more sophisticated versions.

Both of the current aircraft are designed with the primary goal of allowing rapid global mobility, which will allow forces to be rapidly mobilized and maintained anywhere in the world. This includes using the entire range of capabilities provided by each platform to move soldiers, artillery, armor, and support equipment. The upcoming heavy-lift aircraft (HLA) generation needs to be in line with these international demands, which means that it needs to have enough capacity to quickly accumulate substantial assets and long-range capabilities appropriate for operations in the Pacific.

High performance standards are outlined in the new HLA's Request for Proposal (RFP). A payload of 430,000 lbs must be delivered by the aircraft over a minimum unrefueled range of 2,500 nm; a reduced payload of 295,000 lbs may be delivered over a maximum 5,000 nm distance. Notably, the HLA is anticipated to carry up to three M-1 Abrams Main Battle Tanks (MBTs) at once, surpassing the capability of the C-5M. Furthermore, as has been the case in the past with the C-5 class, direct entrance into hazard zones must be avoided; hence, longer, paved runways must be assumed for operational safety.

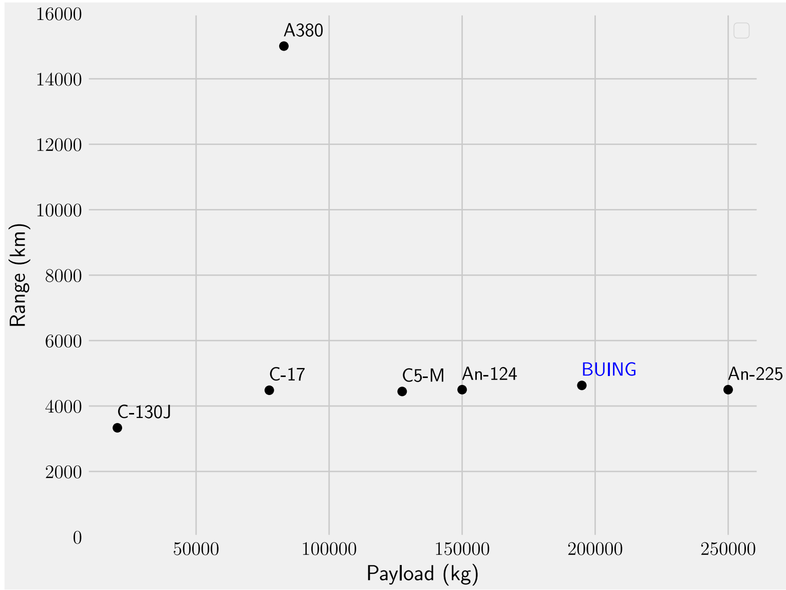

Figure 1.1: Payload capacity against range for similar aircraft.

Another crucial need is enhanced self-sufficiency, which calls for effective loading and unloading capabilities at forward deployment locations. To emulate the C-5's simplified ground operations, as little ground equipment as possible should be required, with low main deck ground clearance being especially important. Additionally, in order to guarantee the aircraft's compliance with the current infrastructure, its total dimensions must meet the requirements of major ICAO class F airports, which allow for an aircraft's limited span of 80 meters while parked.

The suggested HLA will make use of current engines from the military or the commercial transport industry, utilizing tried-and-true technology to maximize efficiency and dependability. Production of the new type is expected to comprise 160 units for the USAF and its military allies, and a further 20 units designated for sales in specific niche commercial markets, leveraging its distinctive outsized cargo capacities.

1.2 Market Analysis

The market analysis for the BUING aircraft entails a thorough examination of the prevailing market conditions, demand projections, competitive landscape, and strategic imperatives within the dynamic military cargo aircraft sector. This analysis serves as a foundational framework for understanding market dynamics, identifying growth opportunities and formulating strategic initiatives to position the BUING aircraft effectively in the competitive marketplace.

1.2.1 Analysis of Comparative Aircraft Specifications

The given Fig. 1.1 shows that the aircraft that most closely match the specifications are located within the range that the AN-124 and AN-225 models indicate. Unexpectedly, these aircraft have payload and range limits of 77,519 kg to 250,000 kg and 4,445 km to 15,000 km,respectively. These values that have been seen align with the specifications specified in the Request for Proposal (RFP). As a result, locating such aircraft offers an ideal opportunity to close the current capability gap and maybe replace the functions that the C-17 and C-5M aircraft currently perform with the intended BUING aircraft.

1.2.2 Current Market Condition

The military cargo aircraft market operates within a complex and ever-evolving global landscape characterized by geopolitical uncertainties, shifting defense priorities, and technological advancements. With diverse operational requirements ranging from tactical airlift missions to strategic logistics support, military cargo aircraft play a pivotal role in facilitating rapid deployment, humanitarian assistance, and disaster relief efforts worldwide. Major industry players, including Lockheed Martin, Boeing, and Airbus Defense & Space, continually innovate to meet the evolving needs of defense agencies and adapt to emerging trends shaping the market. Recent developments underscore the increasing emphasis on sustainability, digitalization, and multi-mission capabilities within the military cargo aircraft sector. As defense agencies seek to enhance operational efficiency, reduce environmental footprint, and maximize mission flexibility, manufacturers are tasked with delivering innovative solutions that offer enhanced performance, reliability, and cost-effectiveness. Furthermore, the growing integration of unmanned aerial systems (UAS) and autonomous technologies presents both challenges and opportunities for traditional cargo aircraft platforms, necessitating agile adaptation and strategic foresight to remain competitive in the rapidly evolving market landscape.

1.2.3 Demand Projections

Projections for the demand of military cargo aircraft over the next decade reflect a mix of geopolitical realities, defense modernization initiatives, and operational requirements across various theaters of operation. While precise demand figures may fluctuate in response to geopolitical developments, defense budget allocations, and emergent threats, industry forecasts indicate a sustained need for strategic airlift capabilities to support expeditionary operations, peacekeeping missions, and humanitarian endeavors. The projected demand for the BUING aircraft is estimated to range between 2 to 4 units over the forecast period, with potential variations influenced by regional security dynamics, coalition partnerships, and technological advancements.

1.2.4 Competitive Landscape

The competitive landscape of the military cargo aircraft market is characterized by intense rivalry among industry incumbents vying for market share, contract opportunities, and technological leadership. Established manufacturers leverage their extensive experience, engineering expertise, and global supply chain networks to deliver cutting-edge solutions that meet the diverse needs of defense customers. The BUING aircraft aims to carve out a distinct niche in the market by offering superior performance capabilities, operational flexibility, and cost-effectiveness compared to existing platforms. By focusing on innovation, customer-centric design, and strategic partnerships, the BUING seeks to position itself as a preferred choice for defense agencies seeking reliable and versatile transport solutions tailored to their mission requirements.

1.2.5 Purpose Built Military Cargo Aircraft

Military cargo aircraft serve a crucial purpose in facilitating the rapid and efficient transport of personnel, equipment, supplies, and humanitarian aid worldwide. With strategic mobility capabilities, they enable defense agencies to project power, deter aggression, and support allied nations in times of crisis or conflict. These aircraft play a pivotal role in tactical airlift operations, delivering troops, vehicles, and cargo directly to theaters of operation to sustain combat missions, peacekeeping efforts, and humanitarian relief. Additionally, they provide logistical support by transporting critical supplies and equipment to forward operating bases and combat zones, ensuring the continuous flow of resources necessary for operational readiness. Military cargo aircraft also contribute to humanitarian assistance and disaster relief by airlifting relief supplies and medical equipment to affected areas, facilitating rapid response and coordination among relief organizations and military forces. Their strategic airlift capabilities further enable the swift deployment of forces in response to emerging threats, crises, or contingencies, enhancing national and international security. Overall, military cargo aircraft are indispensable assets, providing versatility, reliability, and operational capabilities to address a wide range of security challenges and humanitarian crises effectively.

1.2.6 Market Forecast for Military Cargo Aircraft (2022-2035)

The military cargo aircraft market is poised for steady growth and significant opportunities from 2022 to 2035. Demand for these aircraft is expected to rise steadily, fueled by factors such as geopolitical tensions, defense modernization initiatives, and increased requirements for strategic airlift capabilities worldwide. Emerging security challenges, regional conflicts, and peacekeeping operations will drive the need for rapid mobility and logistical support, spurring demand for modernized and versatile transport solutions. Manufacturers are anticipated to invest in technological advancements to enhance aircraft performance, fuel efficiency, and mission capabilities.

Integration of advanced materials, autonomous technologies, and digitalization initiatives will further bolster aircraft reliability, maintainability, and operational readiness.

The competitive landscape of the military cargo aircraft market is expected to remain dynamic, with established manufacturers and emerging players vying for market share and contract opportunities. Product innovation, performance capabilities, and cost-effectiveness will be crucial for manufacturers to differentiate themselves and secure long-term partnerships with defense agencies and commercial operators. Close adherence to regulatory requirements, including FAA certification standards and international aviation regulations, will be essential for market entry and operational success. Manufacturers that can adapt to changing market dynamics, leverage technological advancements, and meet customer requirements effectively will be well-positioned to capitalize on emerging opportunities and drive market expansion in the coming years.

The market analysis for the HLA-921 aircraft entails a thorough examination of the prevailing market conditions, demand projections, competitive landscape, and strategic imperatives within the dynamic military cargo aircraft sector. This analysis serves as a foundational framework for understanding the market dynamics, identifying growth opportunities, and formulating strategic initiatives to position the HLA-921 aircraft effectively in the competitive marketplace.x

1.3 Design Requirements and Objectives

Furthermore, to fulfill the criteria outlined in the Request for Proposal (RFP) for the Heavy Lift Aircraft (HLA), specific design requirements were established. The detailed specifications for the BUING design are presented in Table 1.1

1.4 Conceptual Design

After reviewing the features of current heavy lift aircraft, 4 different concepts were generated as part of the ideation process and all 4 were ultimately.

1.4.1 Concept 1

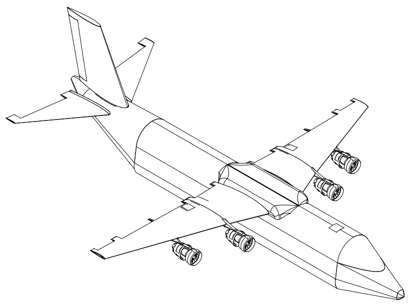

Figure 1.2: Concept 1

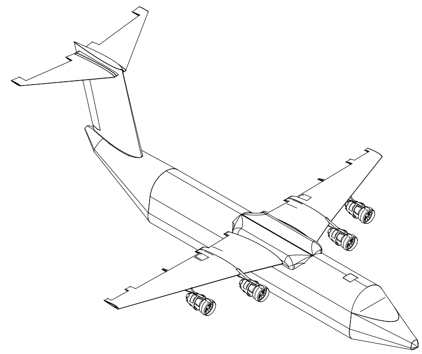

Figure 1.3: Concept 2

The main idea behind the first designs was to produce an aircraft that would give good stability and performance as well as the ability to carry loads in excess of the required minimum.

So the design of concept 1 was quite basic. It is also the base design for the other three modifications that will follow this one. 4 engines, a sharp nose that is very much Boeing 747-esque as well as a conventional tail. At first glance, it gives the impression of similarity to the Ukrainian Antonov AN-124 but with the added benefit of the ability to do mid-air refueling.

This design was scrapped due to the unfavored cross section design of the fuselage which had 'square' walls, as well as the disagreement on the configuration on the tail. A visual representation can be seen in Fig. 1.2.

1.4.2 Concept 2

As previously mentioned, the conventional tail idea was shelved due to it being unfavored by the design group. A high T-tail design was drawn up with the same fuselage and nose, but again was shelved due to the disliked design of the fuselage. At first glance, this would seem similar to the Lockheed C5M, with the difference(s) being that one is larger in size and carrying capacity. A visual representation can be seen in Fig. 1.3.

1.4.3 Concept 3

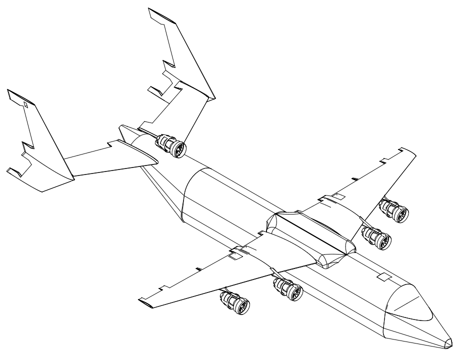

Figure 1.4: Concept 3-5E

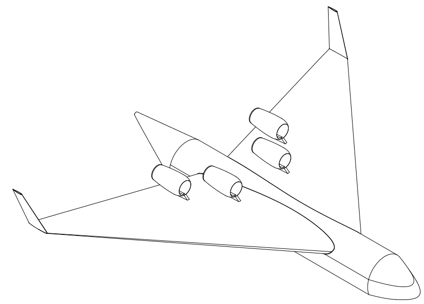

Figure 1.5: Concept X

This one was a more fun concept. Again inspired by the AN225 Mriya, but what if it was not a full six engines. For added power and range, a fifth engine would be placed in between the two horizontal and vertical stabilizers. This would bring back the concept of the ‘trijet’ and is reborn as the ’Quintjet’ (Quint- for the 5 engines). The last aircraft to use an odd number of engine configurations include the Lockheed L1011 TriStar, McDonell Douglas DC-10 and MD-11 as well as the Boeing 727, to name a few. A visual representation can be seen in Fig. 1.4.

1.4.4 Concept 4

Concept X — shown in Fig. 1.5 — takes inspiration from the Blended Wing Body (BWB) UAV that was designed by Boeing and designated as the X-48. It was used as a test bed to investigate the characteristics of BWB aircrafts and was part of a joint research program between Boeing and NASA. Last flown in 2007, the design seemed radical and different, and so was an interesting option to discover. However, this concept was not researched further due to the possible high costs of operating such an aircraft as well as the struggles for maintenance and stability. Here, it features 4 engines and no empennage on the fuselage. Unlike the B-2, this concept features empennage(s) that double as wingtips to increase fuel efficiency. The wing will feature high lift devices, ailerons as well as house the elevators. Access is available via a rear door and the interior is entirely 1 floor, apart from the cockpit that is slightly elevated.

1.5 Initial Sizing

Aircraft	Boeing C-17 Globemaster	AN-225 Mriya	C5-M Super Galaxy	AN-124 Ruslan	Airbus 380
Length (m)	53,04	84	75.53	69.1	73
Height (m)	16.79	18.1	19.84	21.08	24.1
Wingspan (m)	51.766	88.4	67.91	73.3	79.8
Payload Mass (kg)	77,519	250,000	127,460	150,000	83,000
MTOW (kg)	265,351	640,000	381,018	402,000	562,000
Wing Area (m^2)	353	905	576	628	843
Wing Loading (N/m^2)	7,374	6937	6489	628	6540
Loading Access	Aft	Aft & Nose	Nose	Nose & Aft	Aft
Powerplant	PW2040	Ivchenko Progress D-18T	GE CF680C2L1F	Ivchenko Progress D-18T	RR 900 / PW GP7200
Range (km)	4,482	4,500	4,445	4,500	14,800
Ferry Range (km)	11,540	15,400	13,000	16,000	17,960
Takeoff Distance (m)	1,064	3,500	1,646	3,000	2,050
Landing Distance (m)	1,064	3,300	1,097	2,800	2,900
Crew	3-5	3-22	7	8	2

Table 1.2: Specifications for comparative aircraft analysis.

The matching chart and the gross maximum take-off mass (MTOM) estimation contour are shown in Fig. 1.8. The matching chart consists of performance constraints and stall speed graphs, estimated based on Snorri's constraint analysis for turbofan aircraft. The thrust-to-weight ratio T/W of take-off, cruise, turn, climb, ceiling, and landing performances were calculated for various wing loadings W/S. Each line represents T/W required to achieve the parameter values set by the design RFP. The line contour of stall speed V_{stall} was plotted for various $C_{L_{\text{max}}}$ and W/S and drawn along the matching chart to add more information to the overall design space. The feasible design space that gives better performance is shown in the gray area of the plot.

Additionally, a separate calculation was carried out to obtain the gross MTOM (see Eq. 1.1). The calculation was made using Python in-house code (link ...) for various W/S and T/W. The M_{empty} is defined using the empirical model constructed from the benchmark aircraft data (see

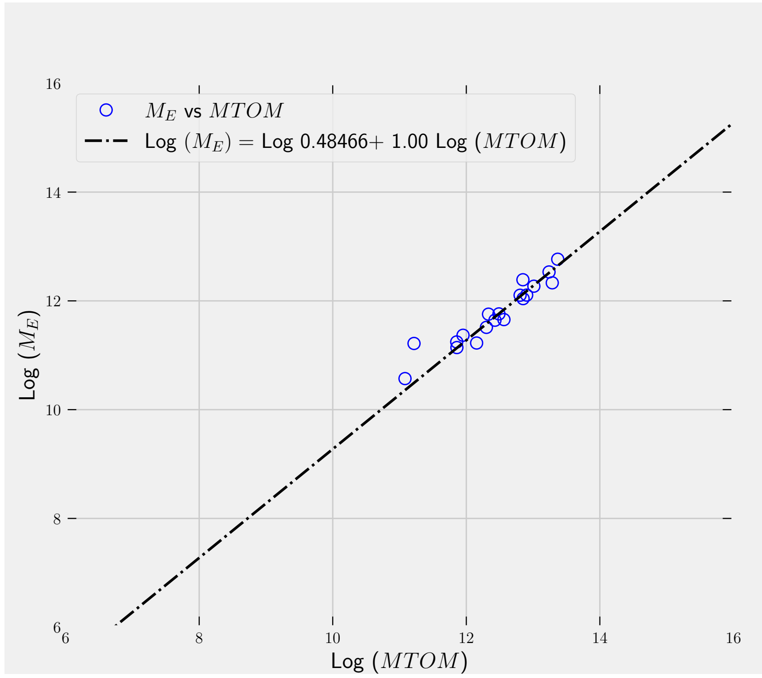

Figure 1.6: Benchmark data of empty mass vs maximum take-off mass.

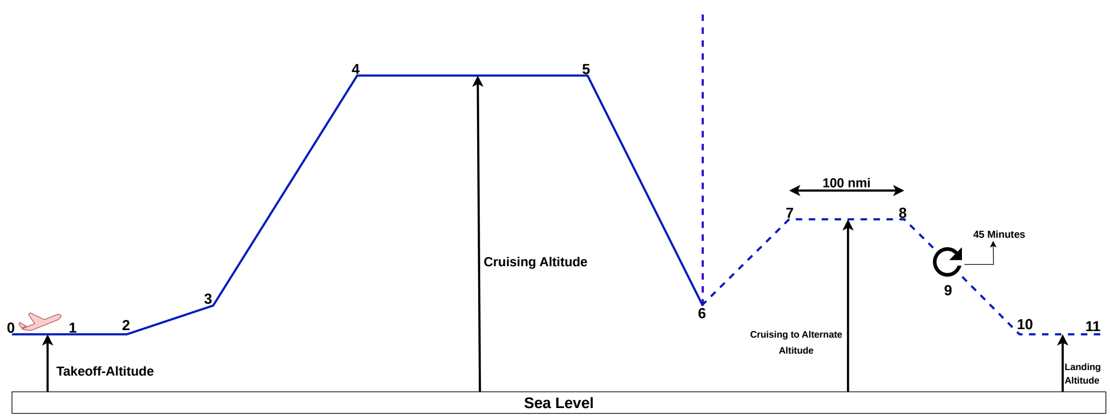

Figure 1.7: Mission profile of BUING.

Fig 1.6). The payload mass M_{payload} is $\sim 195,000$ kg. The fuel mass M_{fuel} is calculated based on the defined mission profile (see Fig. 1.7). The fuel mass fraction for each mission segment was calculated based on Method 3 of Initial Gross Estimation in Snorri's Chapter 6. The lift-to-drag ratios used for cruising flights with a distance of 4630 km (2500 nm) and loitering segments are estimated for various wing areas using the panel method based on Prandt'l Lifting Line Theory, where the $C_{D_{\text{min}}}$ was assumed to be constant, which is ~ 0.025.

Prandtl's compressibility correction was also taken into account for cruise and loitering segments. Here, it is worth noting that other wing geometric parameters, except wing area, are

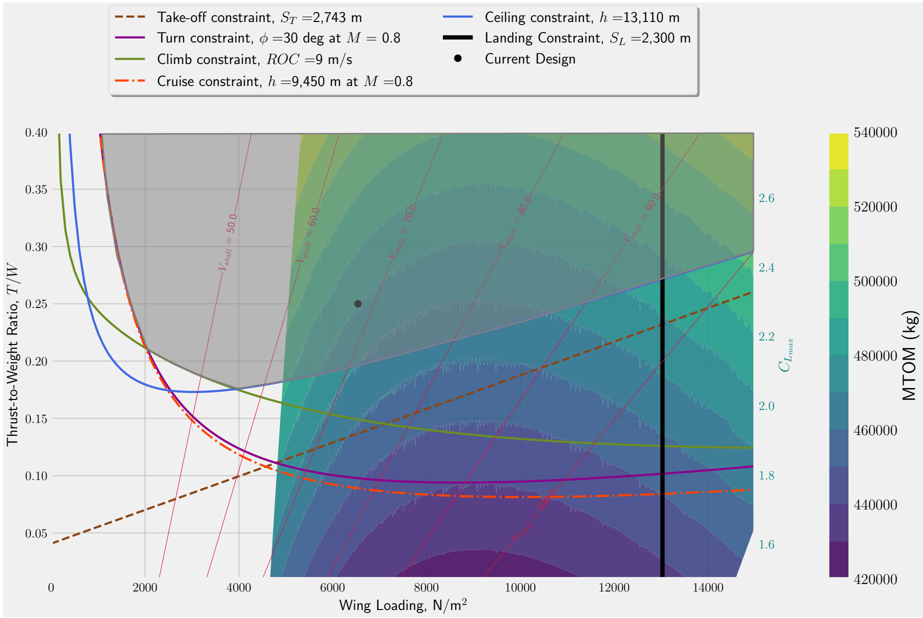

Figure 1.8: Matching Chart and Gross MTOM Estimation Contour; grey color represents the feasible design region.

assumed constant by referring to other aircraft competitors (see InputReq.py for details of the assumed parameters). By assuming the initial MTOM, the iteration will run until the final MTOM is obtained based on Eq. 1.1 was obtain for various wing areas and T/W that are able to meet the design requirement. The gross MTOM results obtained from the calculation are then coincidentally plotted with the matching chart to decide the initial design point for our aircraft. For the initial sizing, the current design is assumed using MTOM$\approx$ $480,000$ kg, $T/W = 0.25$, and $W/S = 6480$ N/m^2 shown by a black point in the Fig. 1.8.

$$MTOM = M_{\text{empty}} + M_{\text{payload}} + M_{\text{fuel}} \tag{1.1}$$

Table 1.1: Table of Requirements and Compliance (RFP)

Description	RFP Requirement	BUING	Met	Section
Aircraft EIS	2033	2033	✓	1.2.6
Engine EIS	Within 5 Years	2006	✓	6.1
HLA Configuration	Fixed Wing	Fixed Wing	✓	2.2, 2.3
Payload	430,000 lbs	482,400	✓	7.3
Payload Type	• 3 Tanks • 48 Pallets • 430 Passengers	• 3 Tanks • 48 Pallets • 449 Passengers	✓	3.7
Crew	• 1 Pilot • 1 Co-pilot • 2 Loadmasters • 4 Backup loadmasters	• 1 Pilot • 1 Co-pilot • 2 Loadmasters • 4 Backup loadmasters	✓	5.1
Wingspan	$\leq$ 80 m when parked	74.65 m	✓	3.2.2
Maximum Payload	2,500 nm (Unrefueled)	3088.5 nm (Unrefueled)	✓	7.1.1
Ferry Range	8,000 nm	8107 nm	✓	7.1.3
Specific Payload	5,000 nm at 295,000 lb	5400 nm at 295,000 lb	✓	7.1.2
Service Ceiling	43,000 ft	33,707 ft @ 75% MTOW	✓	7.5
Cruising Mach & Altitude	0.82 Mach & 31,000 ft	0.75 Mach & 31,000 ft	✓	7.1, 7.1.1
All weather features	all weather type and incorporate deicing, terrain following and terminal avoidance systems	Equipped with deicing, terrain following, and terminal avoidance systems	✓	3.8, 5.5
Autopilot	automated flight control system	Automated algorithms assist in maintaining stable flight, especially with heavy payloads	✓	5.5

CHAPTER 2 AERODYNAMICS

2.1 Airfoil Decision

Fig. 2.1 illustrates the shape of three airfoil candidates for transonic regime with 12% thickness ratio t/c. The x and y are normilized using the chord length c. This particular t/c was selected to accomodate the need to maximize the fuel tanks. Airfoil characteristics, such as $c_l - \alpha$, $c_l - c_d$, and $c_{m_{c/4}} - \alpha$, are shown in Fig 2.2 for three selected airfoil candidates for two Reynolds numbers $Re = 10^6$ and $Re = 5 \times 10^7$. This analysis was done using XFLR5 software at $\alpha = -15 - 25$ deg at and replotted using Matplotlib. The analysis can be accessed at `https://tinyurl.com/25fvycox`. The important characteristics in airfoil selection are tabulated in Table. 2.1 and was score from $1 - 4$, where the score of 4 represents the most desirable quality. Based on the total score of this matrix, the NASA SC(2)-0412 supercritical airfoil was chosen for the wing.

Table 2.1: Airfoil matrix.

No	Airfoil Characteristics	NPL 9510	NASA SC(2)-0412	Lockheed C141	Evaluation Scores		
1	$c_{l_{max}}/c_{d_{min}}$	105.56	118.48	116.29	2	3	2.5
2	Thickness ratio	0.12	0.12	0.12	1	1	1
3	$\alpha_{c_{l_o}}$, deg	-2.051	-2.243	-1.467			
4	$c_{l_{max}}$	1.777	2.172	1.864	2	3	2.5
5	$\alpha_{c_{l_{max}}}$, deg	13.06	15.86	16.23	2	2.5	3
6	Stall characteristics	B	A	A	1	2	2
7	$c_{d_{min}}$	0.00551	0.00538	0.00498	2	2.5	3
8	$(c_l/c_d)_{max}$	163	171	161	2.5	3	2
9	c_l range at drag bucket	-0.241 – 0.237	-0.246 – 0.553	-0.207 – 0.544	2	3	2.5
	Total score				14.5	20	18.5

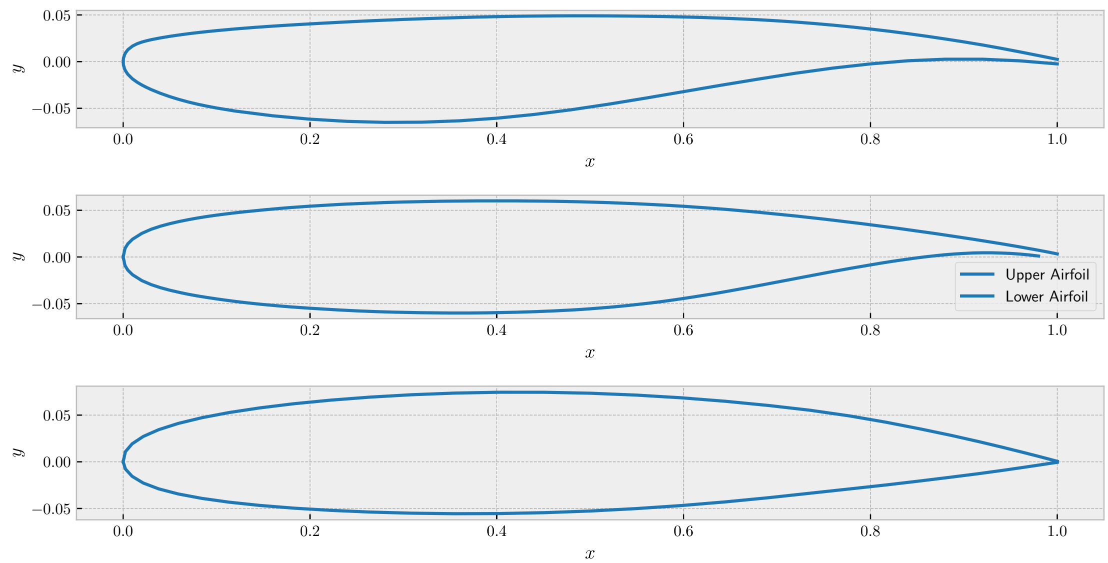

Figure 2.1: Upper, middle, and lower figures are NPL 9510, NASA SC(2)-0412, and Lockheed C141 airfoils, respectively.

2.2 Wing Design

The initial wing gross area were determined by the initial sizing briefly explained in Chapter 1 by using equation $S = \text{MTOM}_{\text{init}}\, g/(W/S)$ from our selected design point, that is $S \sim 720$ m^2. A high-wing configuration was chosen so that the wing root box did not interfere with cargo position for a faster loading and unloading procedures. The wing span length was chosen based on aircraft category for class F Aerodrome, that is < 80 m. A wing with with $\sim 26^o$ sweep angle at the leading edge are chosen which is suitable for a flight in high subsonic regime. The wing dihedral angle was determined to be -6^o based on roll stability calculations and engine ground clearance. The XFLR5 software was used to help in wing design, by ensuring the aircraft is still be able to be trimmed and stable in all longitudinal and lateral-directional modes for the given aircraft MTOM. Detail of the wing geometric parameters are given in Table. 2.2.

The spanwise lift distribution was analyzed at various angle of attack $\alpha = 0, 15,$ and 22 degrees. The sectional lift coefficient along the span position is given in Fig. 2.3. For the wing at $\alpha = 22$ deg, no sectional lift exceeds the $c_{l_{\text{max}}}$ value of airfoil, impliying that no localized stall occurs at this angle, consequently, the stall angle for three-dimensional wing is higher than that airfoil. This wing configuration along with empennages was used to estimate the aircraft aerodynamics using XFLR5.

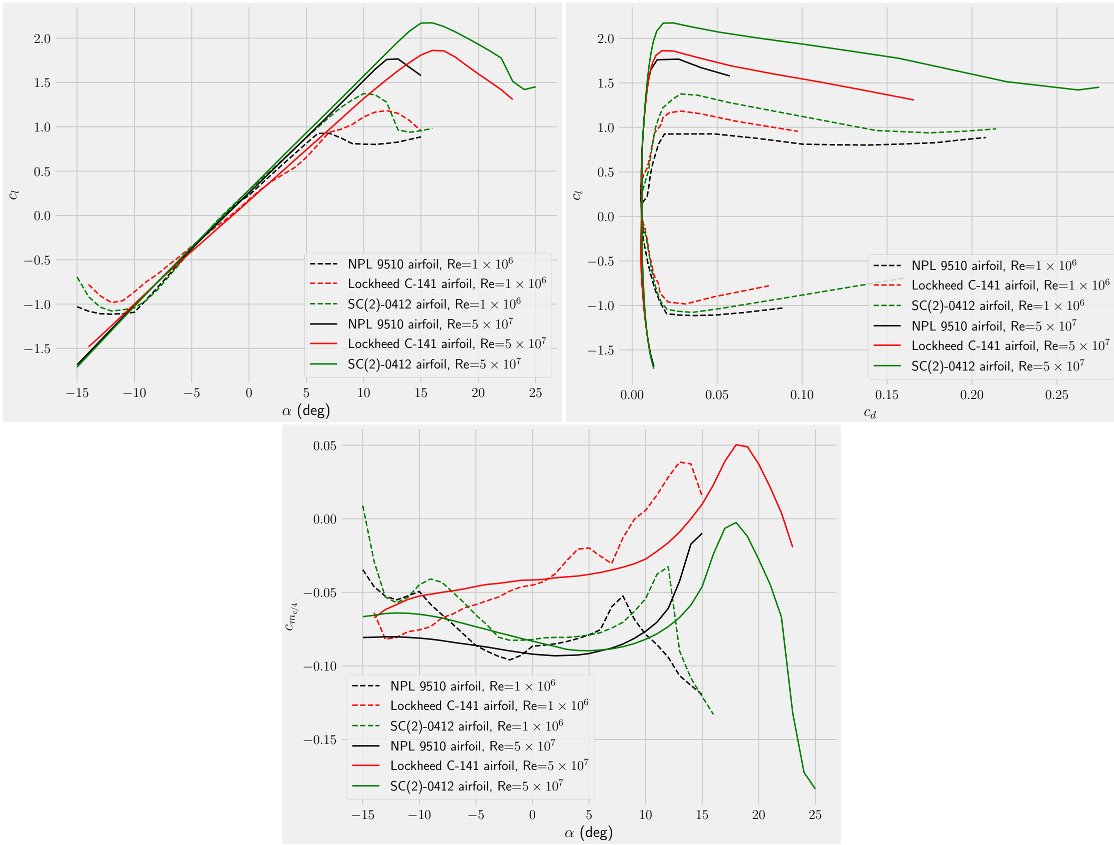

Figure 2.2: Left figure is $c_l - \alpha$, center figure is $c_d - c_l$, and right figure is $c_{m_{c/4}} - \alpha$ for various airfoils at $Re = 1 \times 10^6$ and $Re = 5 \times 10^7$.

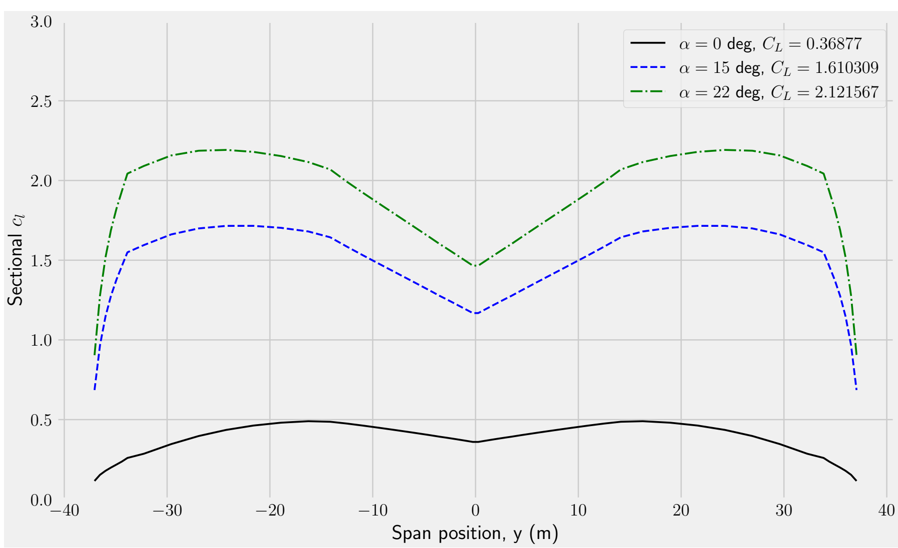

Figure 2.3: Wing lift distribution for various α

Table 2.2: Wing geometric parameters

No	Wing Parameters	Values
1	Airfoil	NASA SC(1)-0412
2	Wing area	728.63 m^2
3	Wing span	74.65 m
4	Aspect Ratio	7.65
5	Chord length at the root	17.5 m
6	Chord length at the tip	4.3 m
7	Mean Aerodynamics Chord (MAC)	11.21 m
8	Taper ratio	0.25
9	Dihedral angle	-6 deg
10	Root-to-tip sweep angle (L.E)	26.15 deg
11	Washout angle at the root	4 deg
12	Washout angle at the tip	-2 deg

2.3 High Lift Devices

The design of high lift devices was driven by the landing and takeoff distance requirements. For this aircraft, the leading edge slats and trailing edge Fowler flap were selected and sized on the basis of a required $C_{L_{\max}}$ at takeoff and landing. The chord length of the slat c_s and the flap c_f are $0.2c$ and $0.7c$, respectively. The layout of the high-lift devices (slat and flap) configuration is shown in Fig. 2.4.

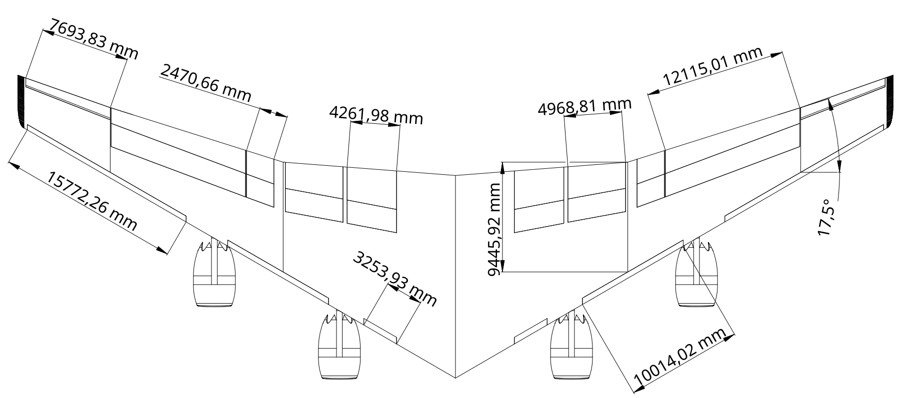

Figure 2.4: Layout of high-lift devices.

2.4 Drag Buildup

Analysis of drag buildup is vital due to its effect on aircraft performance. OpenVSP software was used to construct a model to analyze the drag build-up of each aircraft component. Figure 2.5

shows the aircraft model with all its external components used in the analysis. Here, the coefficient of pressure C_p at $\alpha = 0$ shown as a contour. Using parasite drag analysis, a summary of corresponding drag estimation of the aircraft's main components is displayed in Table 2.3. This data was later inputted into XFLR5 for drag correction in the aerodynamics and and stability analysis of the aircraft.

Table 2.3: Parasite drag of aircraft components.

No	Components	S_{wet} (m^2)	FF	C_f (10^{-3})	C_{D_o}	Contribution (%)
1	Fuselage	1555.4	1.08	1.66	0.00383	23.45
2	Landing Gear	359.52	1.22	1.84	0.00111	7.2
3	Wing	1335.47	1.25	2.14	0.00493	41.26
4	Horizontal Tail	309.9	1.23	2.35	0.00123	8.88
5	Vertical Tail	128.71	1.23	2.41	0.00052	3.8
6	Engines	342.87	1.85	2.43	0.00212	15.42
	Total				0.01374	100

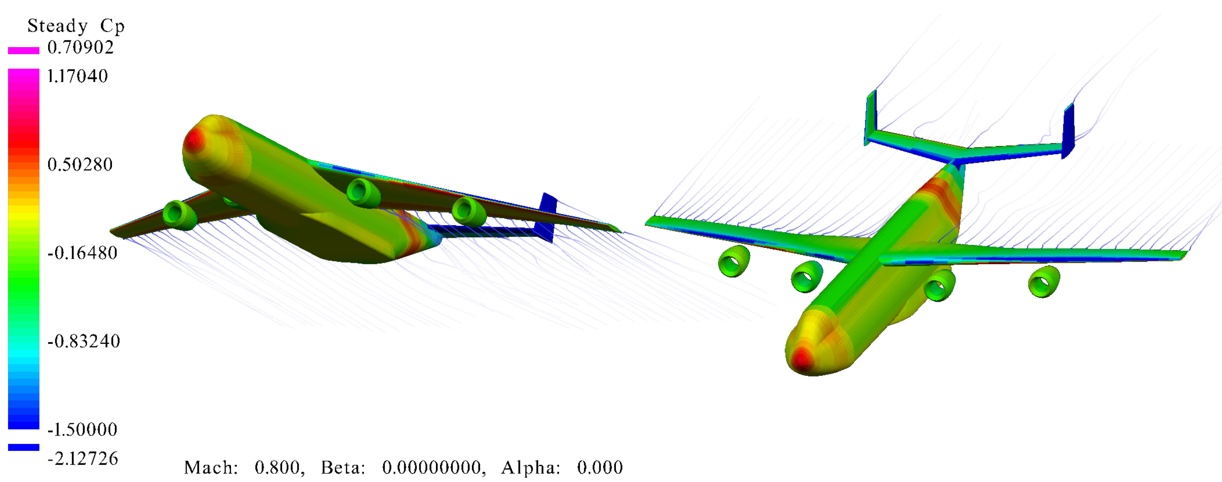

Figure 2.5: OpenVSP model of full aircraft at $\alpha = 0$.

2.5 Aircraft Aerodynamics

With wing and empennage were constructed in XFLR5, the drag correction was made based on the parasite drag estimation from OpenVSP (see Section. 2.4). The XFLR5 model can accurately calculate the wing and empennage without the fuselage, but a correction was required. The aerodynamics profiles of the aircraft for various α are shown in Fig. 2.6. In this graph, the data for landing and take-off configuration are provided as well. For take off configuration, the wing with deflection flap angle $\delta_f = 30^o$ and slat angle of $\delta_s = 15^o$ is set to lift the MTOM$\approx 550,453$ kg. In addition, for landing, the high-lift devices are set at $\delta_s = 15^o$ and $\delta_f = 40^o$. This data in this plot was fitted to linear and quadratic equation to get general aerodynamic equation for performance calculation (see the equations in the plot legends).

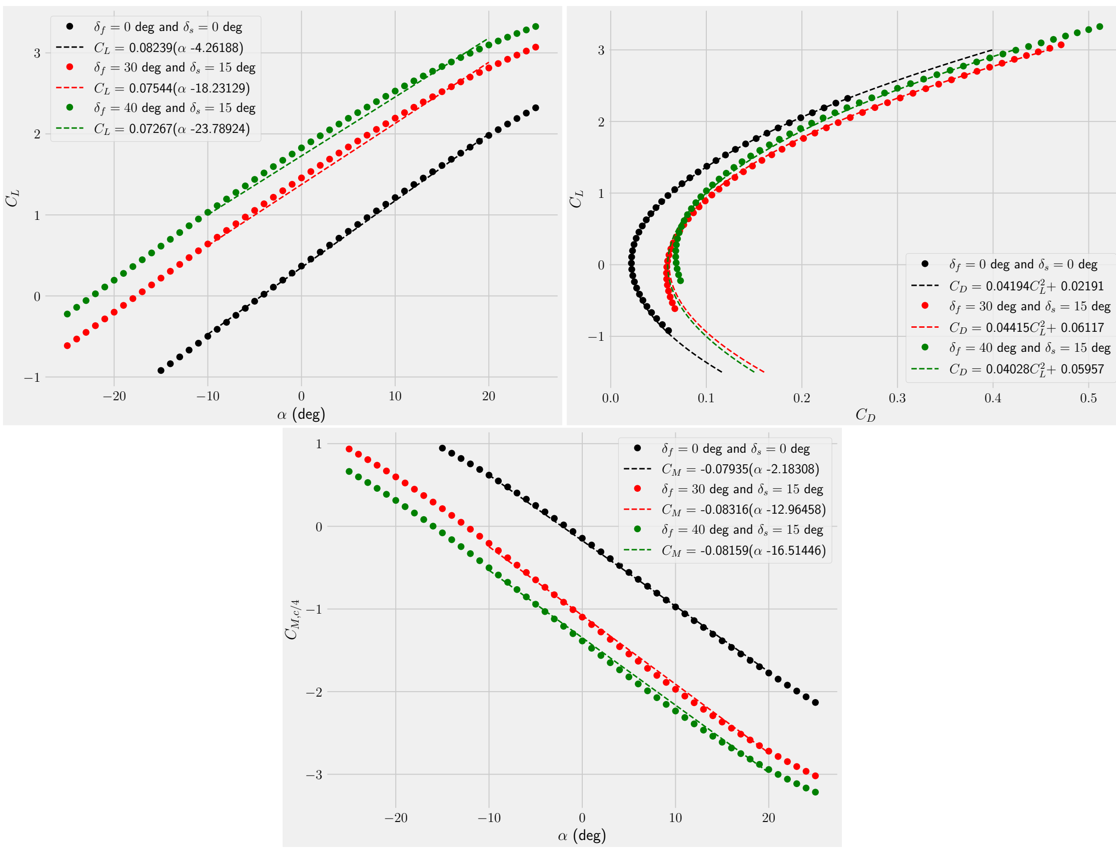

Figure 2.6: Left figure is $C_L - \alpha$, center figure is $C_D - C_L$, and right figure is $C_M - \alpha$ for aircraft at various configurations.

CHAPTER 3 STRUCTURES

A detailed CAD model was created using Onshape CAD software by PTC. This model shows the exact dimensions of the exterior and shows one potential interior layout. The three-view dimensioned drawing and isometric view is shown in Fig. 3.1. A detailed airframe structural design are shown in Section 3.3. Here is the three-view drawing link `https://tinyurl.com/2b9kuceo`.

The structural analysis of the aircraft started with the construction of a V-n diagram for various critical conditions at equivalent airspeed (EAS) with a MTOM of 550 453 kg based on 14 CFR § 25.333. The V-n diagram for the BUING's aircraft is shown in Fig. 3.2. The aircraft is assumed to be in its clean configuration without flaps or slats deployed. The stall, cruise, and dive speeds are 74.75, 278.8, and 348.8 m/s, respectively. Those are defined at normal manuever as well as maximum gust intensity, which ranged from $-17 - 17$ m/s. The manuevering load factor is defined from -1 to 3.8. In order to ensure the aircraft structural integrity, all the subjected loads to the fuselage, wing, and empennage were multiplied by the maximum load factor 3.8 and 1.5 factor of safety. These values were used to preliminarily estimate the structural main component dimensions of the fuselage frame, rib, spar, and stringer.

3.1 Material Selection

Aluminium alloy was chosen as the primary material due to its relatively light weight and high strength. For fuselage, Al2024-T3 was chosen as the fuselage material due to its relatively high yield stress and low mass density (see the properties in Table 3.1, data gathered from MatWeb [8]. Additionally, Al2024-T3 is a reliable material to sustain the periodic tension load due to cabin pressurization, thus less prone to fatigue failure [9].

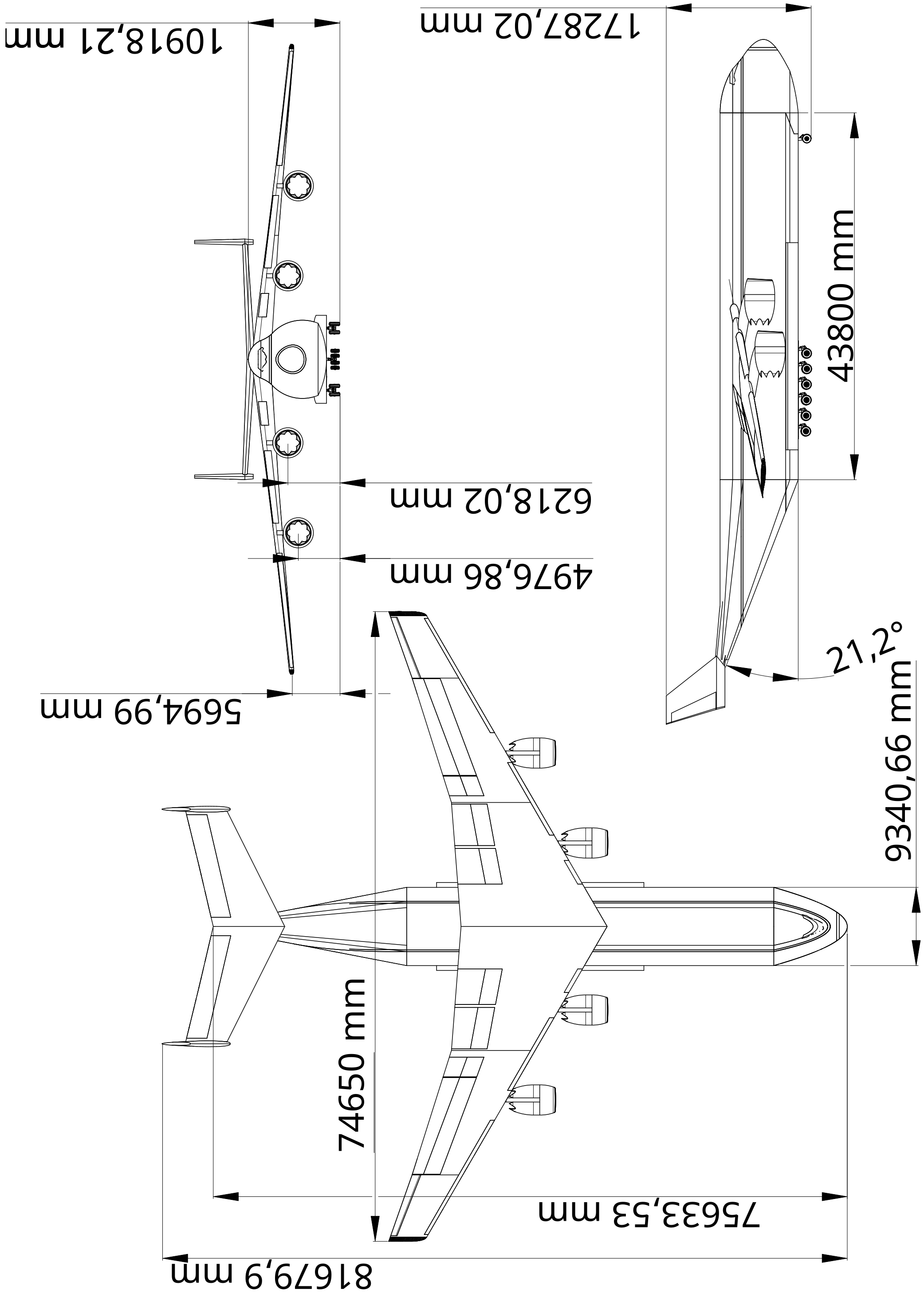

Figure 3.1: Three-view drawing

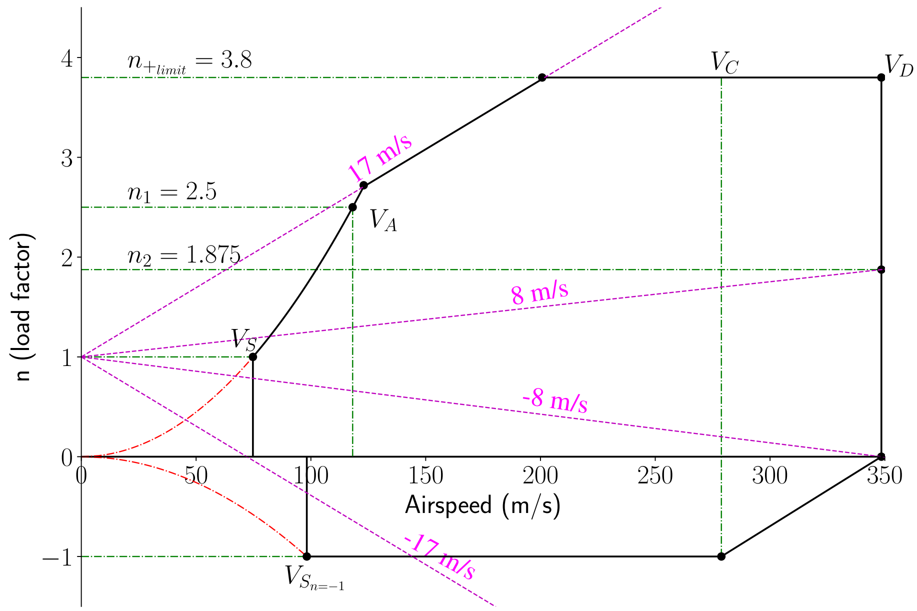

Figure 3.2: V-n diagram. The magenta color represents gust design velocity.

Table 3.1: Material properties

Material	Density (kg/m^3)	Max ultimate tensile strength (MPa)	Max tensile yield strength (MPa)
Carbon fiber epoxy	1700	3792	3013
Al7075-T6	2823	572	503
Al6061-T6	2699	310	276
Al2024-T3	2768	440	290

By comparison, Al7075-T6, another commonly used aluminium alloy in aircraft, is much stiffer and has a much higher tensile strength (see Table. 3.1). Those properties make Al7075-T6 more commonly used in areas where there are high compression stresses such as wings and unpressurized fuselage. Therefore, for the wing and empennage of BUING, we chose Al7075-T6 as its main material. Another consideration of selecting Al7075-T6 is due to its cost effectiveness, favorable properties to heat cyclic-load, higher impact absorbent compared to the Carbon Fiber Epoxy. Regarding the composite material, although it has excellent properties, using it would drastically increase non-recurring costs such as development, material and manufacturing costs [10]. Current modern aircrafts, like Boeing 787 and Airbus A400M, made 30% – 40% of its airframe from the composite to reduce weight. Due to the advancement of the composite health monitoring research, the use of composite material become one of the feasible option for BUING to reduce 10% of its empty mass, which is equivalent to $\sim$ 24 654 – 32 872 kg. By making sure the BUING's stability lies within its static margin (see Chapter 8), the mass reduction will be less challenging.

3.2 External Structural Consideration

3.2.1 Fuselage

A double-decker cylindrical-esque fuselage was chosen. An ovular cross-section would be structurally complex and weigh more, where as a squared-off fuselage would lose plenty of aerodynamic efficiency. The size of the fuselage was determined by cargo requirements as well as the requirement to carry passengers on/in a separate compartment from the main cargo bay. The fuselage dimension is 9.34 m wide and 74.06 m long (see Fig. 3.1). The cargo bay section is 43.8 m long. The belly upsweep angle is 21.2 degree in order to avoid tail strikes on takeoff. The cross section of the fuselage can be seen in Fig. 3.25.

3.2.2 Wing and High-Lift Devices

The wing was initially sized from preliminary study and with wingspan of 74.65 m and total area of 728.63 m^2 provides sufficient lift for the BUING. Detail of wing dimension can be found in Chapter 2.

BUING's wing features a single slotted Fowler flap and leading edge slat, extending from the 10% of the span from the fuselage and out to 79% of the wingspan, leaving about 20-21% span for ailerons and the wingtips, as depicted in Fig. 3.3. The flap chord is 35% of wing chord located at $0.7c$ and is stowed within the wing when not in use, as shown in Fig. 3.3. Detailed of the dimension of high-lift devices can be found in Fig. 2.4. An illustration of a single slotted Fowler flap can be seen in Fig. 3.4 [11].

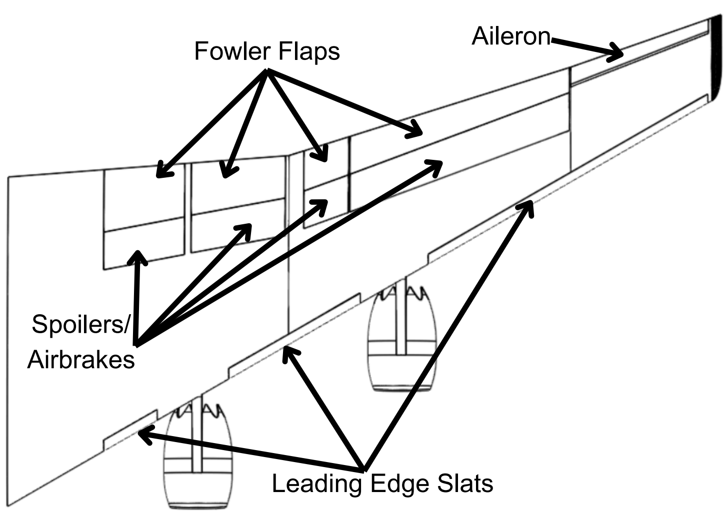

Figure 3.3: High Lift Devices.

Figure 3.4: Illustration of Fowler flap [11].

3.2.3 Empennage

The horizontal and vertical stabilizers will be in a H-Tail configuration. A T-tail was considered but ruled out because of the potential dangers of entering deep stall at high AoA (α). It was decided that a V-tail was not a feasible option for an aircraft of this size. A conventional tail configuration was considered too simple of a concept. A radical flying wing design was thought up, but was ultimately shelved due to concerns of the high costs it may inflict in production and complicated maintenance.

Empennage sizing was determined by stability and control and is discussed further in Chapter 8. The upsweep of the aft section is determined by aerodynamics and landing gear. In order to avoid a tail strike on landing or takeoff, the belly upsweep has been set to 21.2 degree. This can be seen in the three-view drawing in Fig. 3.1.

3.2.4 Doors and Windows

The cabins of the aircraft are accessible from the outside via 4 doors, 1 main cargo door at the nose, 1 passenger boarding door at the front and 2 paratrooper doors towards the rear. Casual boarding will take place at the front left door via an integrated staircase. The other two doors are parachute doors, with no integrated hardware for boarding or de-boarding. A total of 4 emergency escape doors are provided on the upper deck of the aircraft, 2 towards the front and 2 towards the rear. Each door is 1.05 m wide and 1.88 m tall and is certifiable as a Type A emergency exit door [12].

The main cargo bay features 4 access points, 2 paratrooper doors to the rear, 1 normal access door at the front and the main nose door. The cockpit and front cabin features 2 emergency escape doors. While the rear cabin, which houses passenger seating for 107 passengers, also features 2 emergency escape doors. All emergency escape doors, feature an inflatable rubber slide to aid in evacuations in the events of an accident/incident/ditching of aircraft in the water. Rubber life vests are available below the passenger seats and emergency slides are deployable from each emergency door.

The front access door is accessible via an electrically retractable staircase, similar to the ones featured on the Boeing 737, and allows for boarding and de-boarding without the need for external

Figure 3.5: Staircase Example (`https://tinyurl.com/28h8y499`)

aid or infrastructure. A better visual representation can be seen in Fig. 3.5.

3.3 Structural Arrangement

3.3.1 Fuselage Internal Structure

The components of the main structure of the BUING can be found here, including the fuselage, wing, empennage, and horizontal and vertical stabilizers. Each of these components have structural configurations meant to handle and distribute the loads expected through the full flight envelope to ensure failures will not occur. The complete structural configuration of fuselage frame and longeron can be seen in Fig. 3.6. The main structural components of the fuselage consist of the frames, stringers/longeron, bulkheads, and skin. Many of these parameters were determined following approximations found in Roskam Part 3 [6]. The shape and dimension of fuselage's airframe components can be seen in Table 3.2.

Since BUING will be flying at high altitudes up to 41 000 ft, it is essential that the cabin and cargo bay be pressurized to a maximum of 0.8 atm. This means the inside of the aircraft will have to maintain a pressure of around $0.7 - 0.8$ atm throughout the entire flight envelope, with a pressure difference of around 0.4 to 0.5 atm between the interior and atmosphere during cruise. A

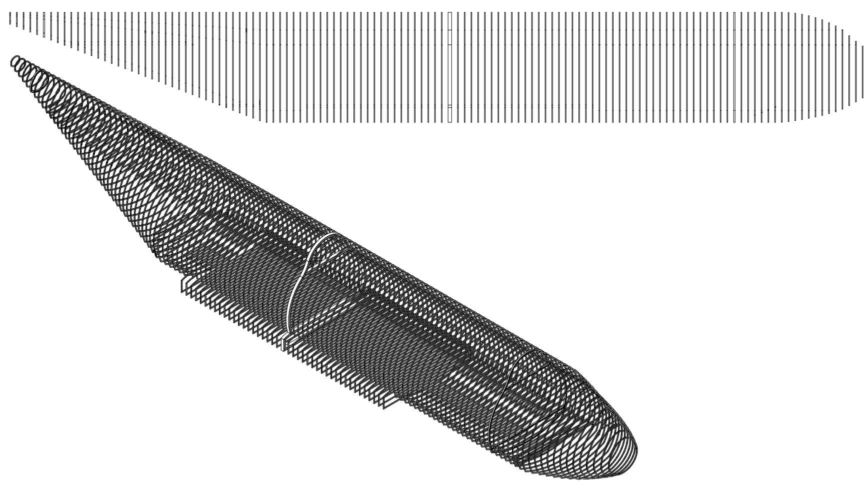

Figure 3.6: Fuselage internal structure with frame arrangements.

Table 3.2: Beam cross-section of frame and stringer.

No.	Components	h (m)	w (m)	t (m)	Note
1	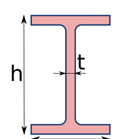	0.14	0.12	0.02	Nose and tail heavy frames
2	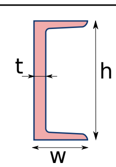	0.08	0.07	0.02	Light frame
3	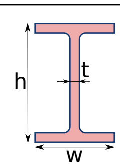	0.24	0.3	0.07	Wing heavy frame
4	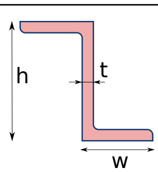	0.01	0.01	0.002	Stringer

total of four bulkheads and three heavy frames were decided to use to distribute the heavy loads on the BUING fuselage. The bulkheads were placed in the nose, tail, rear of the front cabin and front of the rear cabin of the aircraft to maintain pressurization of the fuselage and cabins. The first heavy frames are placed right after the cockpit (near nose landing gear). The second heavy frames are located near the mid spar of the wing box (near the main landing gear) allowing for the loads from the wing and landing gear to be transferred to the rest of the airframe structure. The third heavy frame is located on the front spar of the tailplane. Here, note that the shape selection is not final, but the cross-section represents area and second-moment of inertia that require to sustain the tension/compression, bending moment, and torsion subjected to the sectional fuselage region due to the payload and its distributed mass. The total number of fuselage frame is 178.

3.3.2 Wing Internal Structure

The main wing structure consists of a series of ribs attached to three main spars that run along the wing span and connect at the center in the wing box as shown in Fig. 3.7. Due to the large surface area of the wing and considerations from Roskam [6], a multispar wing box design is chosen, and the overall wing structure is relatively conventional and can be seen in Fig. 3.8. The front spar was placed at 25% of the chord and the rear spar located at 65% of the chord along the span of the wing, while the mid spar is located at 45% of the chord along the wing span. The size of of the spar and rib determines from the aerodynamics load provide from the lift distribution given at $\alpha = 0$ in Fig. 2.3. The inertial load due to fuel is neglecting since the heaviest load occurs when $m_{\text{fuel}} = 0$. The highest values of bending moment, tension/compression, and torsion due to aerodynamics load multiplied by maximum load factor and factor of safety are used as the input to the calculation based on [13]. Here we used a 1.52 meter rib spacing, which give to total number of wing rib is 50 based. For the spar, its width (W) are varied, depending on location, between 0.02 to 0.7 meters, height (H) varies between 0.08 to 0.5 meters and the thickness (T) between 0.003 to 0.086 meters (see Fig. 3.8 for the spar shape and parameters).

3.3.3 Empennage Internal Structure

For the horizontal and vertical stabilizers, two spars are used. The spacing of the ribs in the tail is set to 0.64 m apart. The horizontal tail surface also has a wing box similar to that of the wing, while the vertical tail will be mounted on the tips of each horizontal tail. The horizontal and vertical stabilizers can be seen in Fig. 3.9.

3.4 Internal Volume Requirements

3.4.1 Fuel Tank

Fuel tank is divided into 8-10 integral tanks on each wing. Fuel volume was estimated and calculated from CAD drawing to be 291.763 m^3 at the worst-case scenario. The fuel density is assumed 750 to 840 kg/cubic meter. Fuel tanks are to be housed within the wing and placed

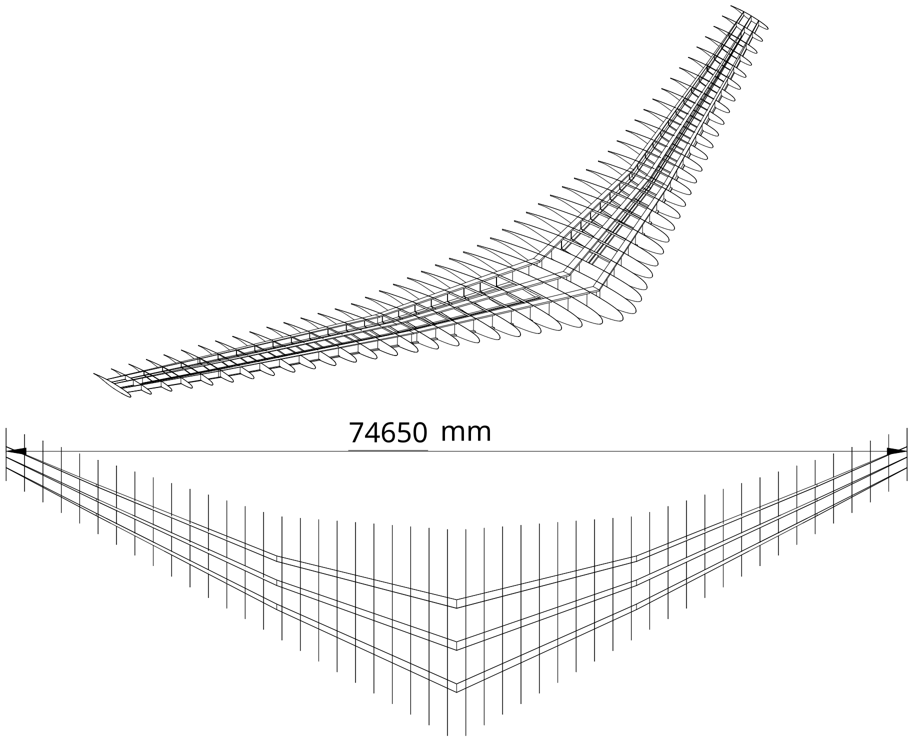

Figure 3.7: Wing internal structure with ribs and spar arrangements.

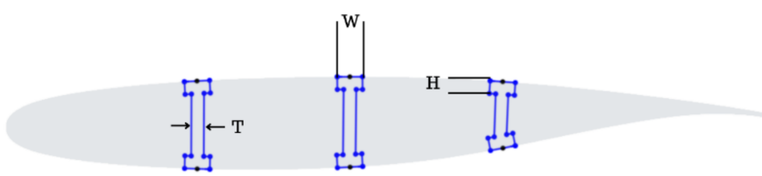

Figure 3.8: Wing Spar Location

as shown in Fig. 3.10. Table 3.3 indicates the available volume of those tanks calculated using Onshape, revealing the total available volume is $\sim$ 291.763 cubic meters or 291 763 liters.

Table 3.3: Tank Info.

No	Tank location	Volume (Litre)
1	Wing Fuel Tank	275 663
2	Vent tank	16 474
	Total volume	291 763

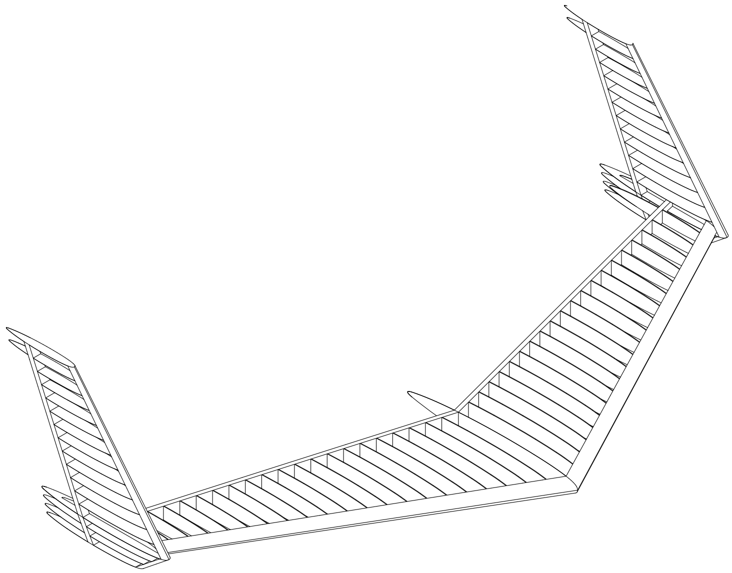

Figure 3.9: H-Tail Structure

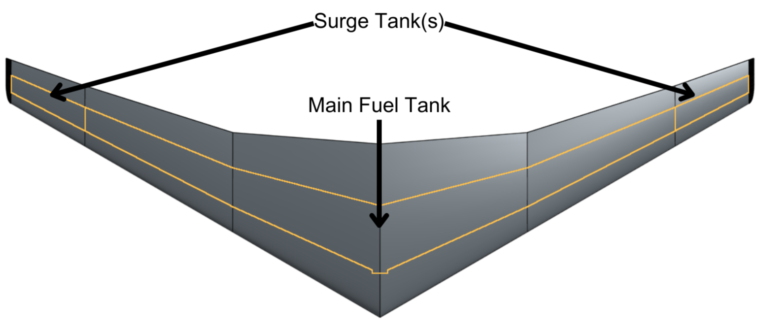

Figure 3.10: Fuel Tank Location

3.4.2 Refuelling System

For BUING's high wing configuration, a refueling inlet is located towards the rear of the aircraft, on the side of the main landing gear housing at the right side of the aircraft (see Fig. 3.11). The port is accessible by any nozzle that is designed per MIL-N-5877E requirements. This offers the least nozzle pressure drop and will ensure quick refueling. The pressure of fuel entering is set by the regulations at a maximum of 379.2 kPa. A backup gravity inlet is provided beneath the left hand side of the wing and is located at the point shown Fig. 3.12.

3.4.3 Mid-Air Refuelling

As a mentioned in the requirement, a refueling port is provided behind the forehead of the cockpit and is accesible by an USAF flying boom type receptacle, but is modifiable to accommodate other types of receptacles. The size of the nozzle envelope is taken from the reference

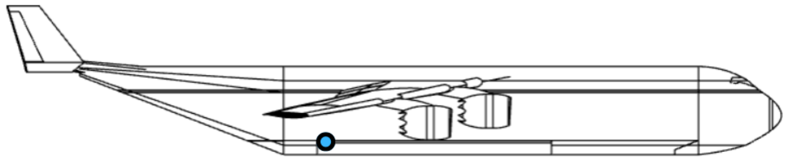

Figure 3.11: Main fuel inlet.

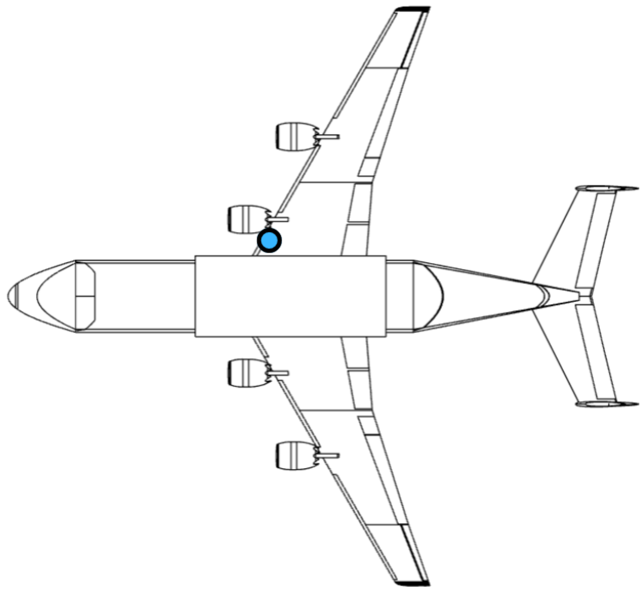

Figure 3.12: Alternate fuel inlet.

provided in Fig. 3.13 from [14].

3.4.4 Extra Fuel Tank

The idea of extra fuel tanks was drawn up and planned for the installation within the structure of the tailplane. It would provide some added benefits to the aircraft and its missions, especially to increase the range. It also can be used as a ballast for balancing the aircraft and shifting the center of gravity either forwards or back. This idea was ultimately cancelled due to the added weight it would bring by modifying the rear structure thus making it much heavier. A rough illustration is provided in Figure 3.14.

3.5 Engine Inlet and Nacelle Design

One of the most important aspects of engine integration is the size of the inlet. In subsonic to transonic operation regimes, the flow which the front of the engine experiences is too fast and needs to be slowed down. Raymer suggests an inlet speed of approximately Mach 0.4 to Mach

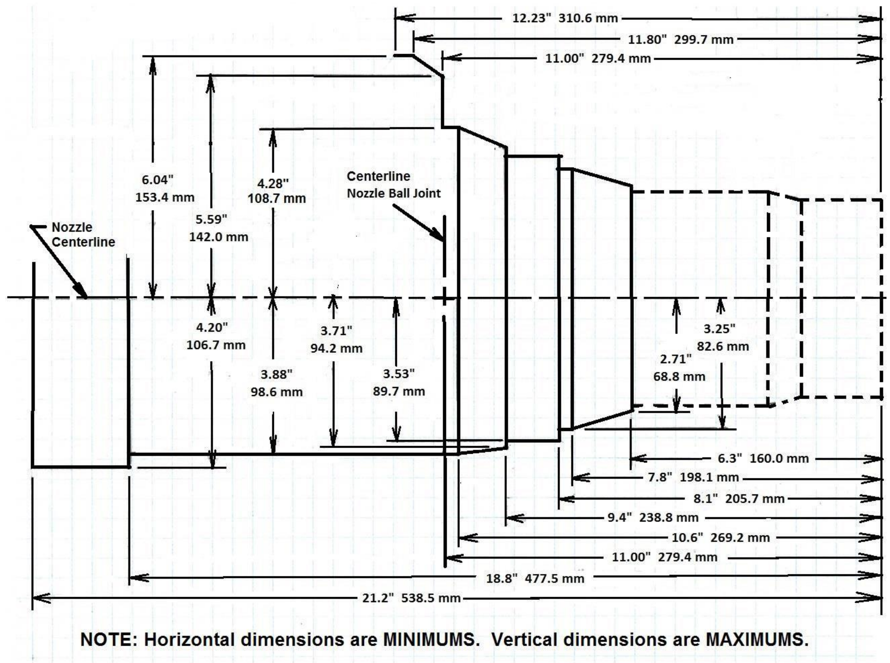

Note: The portion of this diagram below the centerline shall apply to the lower 180 deg. of the nozzle.

Figure 3.13: Mid-air Refuel hole size CITE

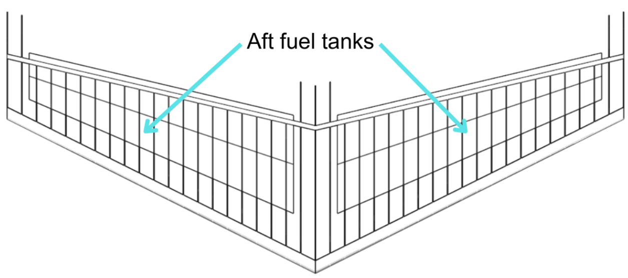

Figure 3.14: Tailplane Fuel Tank

0.6. Since much more compression occurs at the inlet, the inlet needs to be smaller than the fan diameter. Raymer [2] specifies multiple constraints for the nacelle. Firstly, the lip radius of the inlet should be between 3-5% of the radius of the inlet. The inner and outer lip radii were set to 8% and 4% of the inlet radius. This decreases distortion of the air as it enters the inlet. Additionally, nacelle design was derived from existing aircraft with the same engine. A spike was included in the exhaust to reduce noise. Fig. 3.15 shows an engine with integrated nacelle and exhaust chevrons, similar to the ones on the Boeing 787 to reduce the amount of noise produced by the powerplants.

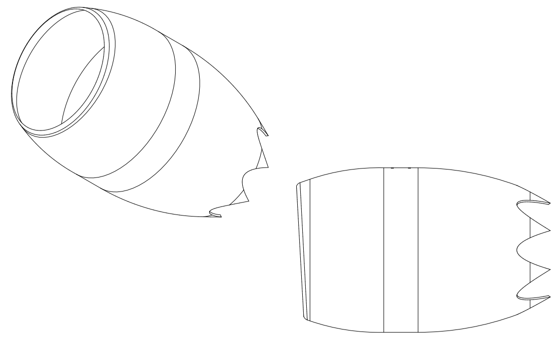

Figure 3.15: Engine Nacelle Desing

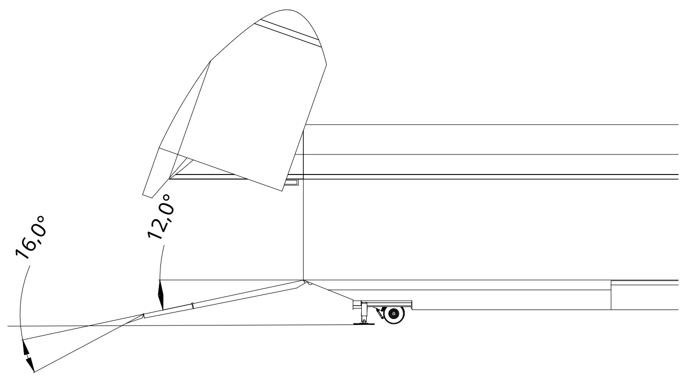

Figure 3.16: Nose Door Ramp

3.6 Cargo Loading

Cargo is to be loaded via a single cargo bay door at the front of the aircraft, behind the nose. Similar to the C5M, however there is no access via the rear of the aircraft. This choice was taken for its simplicity, better structural control of the rear, and less weight.

As part of a requirement, the cargo hold is accessible by a ramp which will deploy at a maximum ramp down angle of no more than 12 degrees with ramp toes being at a down angle of no more than 16 degrees as shown in Fig. 3.16. The ramp comprises of 2 main elements due to storage limitations that will both deploy at a maximum 12 degrees against the cargo bay floor. A small set of ramp toes are attached on the end of the secondary ramp and will be deployed down at a maximum 16 degrees against the ramp. To make this possible, the landing gear retracts slightly and tips down the front to a maximum angle of about 1.5 to 2 degrees.

The dimension of the ramp(s) is 8.77 meters in length and is 8.4 meters wide at the mouth of the cargo bay and 4.3 meters wide at the tip of the tongue. The toes are 4.3 meters wide.

The aircraft's nose doubles as an access door to the cargo bay and is opened via a mechanism that is below the cockpit.

The floor of the cargo bay features a modular floor. This floor allows it to change according to its mission. One configuration is that of rollers that are used to move pallets around and in the cabin and the second configuration is of a flat deck, which allows for the installation of seats or the loading of vehicles and other cargo that are not placed atop a pallet.

3.7 Payload Arrangements

3.7.1 Passenger/Paratroops

The seat for passenger is designed based on the configuration in Raymer's book [2], by considering the seat pitch, seat width, aisle width, aisle height, and head room. The single chair of this aircraft consists of the rear table, arm chair, and the body of the chair, and its dimension is shown in Fig. 3.17. Due to the positioning of other aircraft subsystems, the arrangement slightly different between the front cabin (mainly 3-2 configuration) and the rear cabin (mainly 3-3 configuration). Detail of those arrangement can be seen in Figures 3.18, 3.19, and 3.20. Total number of seats are 107. The link for the aircraft seat, its arrangement, the single seat and the life vest box is https://tinyurl.com/254rw9fs.

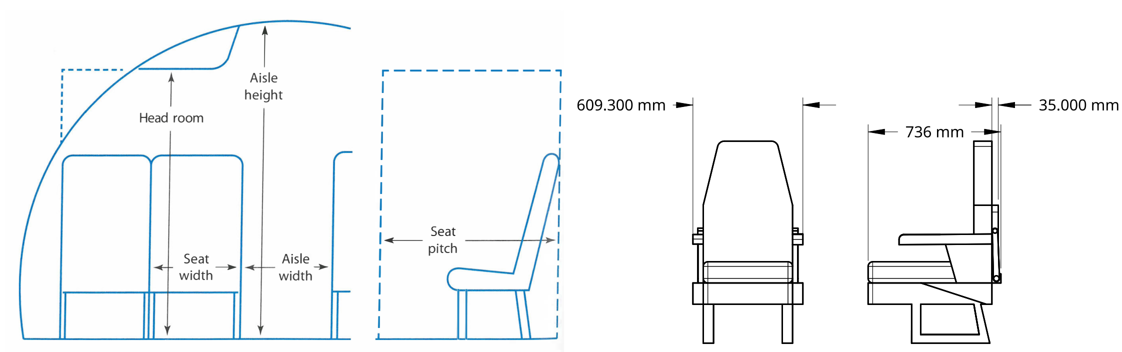

Figure 3.17: Left figure is seat dimension based on Raymer [2] and right figures is single seat configuration and dimension.

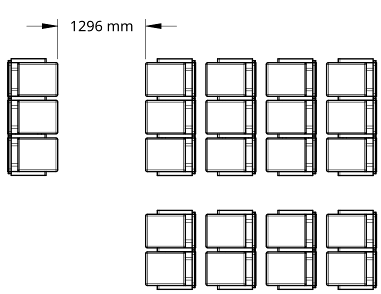

Figure 3.18: Front seat arrangement (top view)

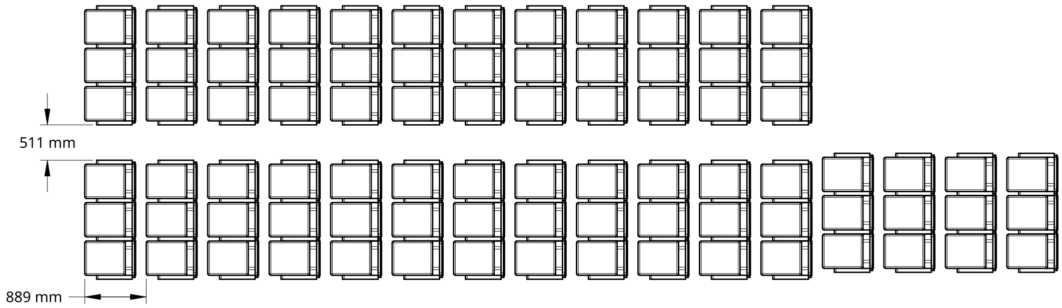

Figure 3.19: Main seat arrangement (top view).

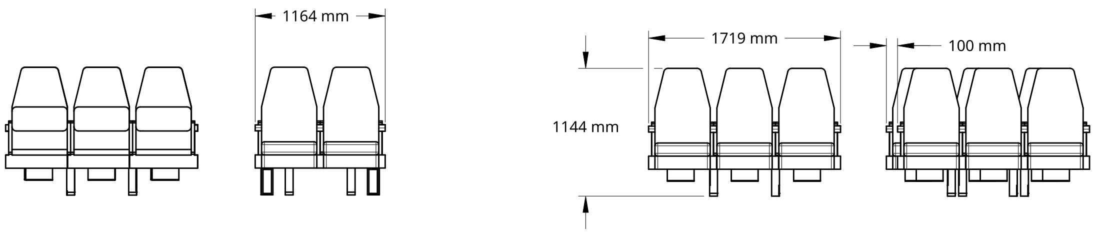

Figure 3.20: The front and main seat arrangements with dimension (front view), respectively.

All of the above seat arrangement is located at the upper deck cabin. Front cabin accomodates 23 passenger in economy seats and 2 crew rest quarters of twin sized bed(s) as well as a storage closet. Two commercial airliner standard galleys are provided also, and 2 lavatories at the rear section of the front cabin. Provisions are available for additional storage rooms or an additional crew rest quarter in the front cabin by removing the 2 abreast seats. Personal belongings can be stowed beneath every seat in either cabin. The rear cabin is able to accommodate 84 passengers. The detail layout of upper deck cabin can be seen in Figures 3.21.

3.7.2 Other Cargos: Pallets, Tanks, Additional Seatings

Figures 3.22, 3.23, 3.24 also show the main dimensions of 3 types of cargos that are able to be carried by the BUING loaded by using the nose cargo door (see Fig. 3.16). The three types of cargo that can be carried by the BUING are 463L Pallets, H-70 Black Hawk helicopter, and M1 Abrams tank, that can be put into 1742.1 cubic meter cargo volume illustrated in Fig. 3.25.

Configuration 1: Pallets

The first configuration is to carry 48 463L Pallets. The placement of the pallets is arranged as such to limit the width of the cargo bay, consequently smaller fuselage width. One pallet is able to carry up to 4500 kg of cargo. Forty-eight pallets are equivalent to around a maximum of 216 000 kg of cargo. The configuration for aligning the cargo pallets are shown below in Figures 3.26

.

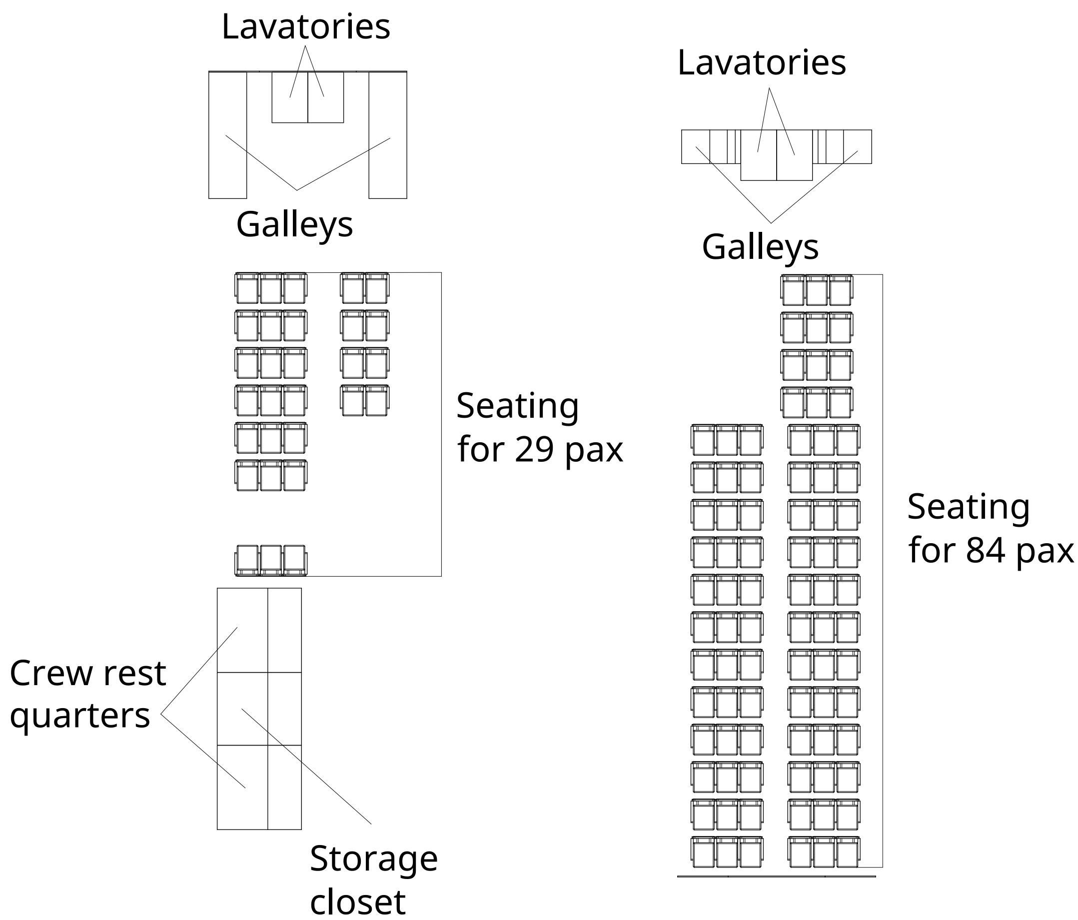

Figure 3.21: Upper deck configuration. The left and right figures are the layout of front and rear upper deck, respectively.

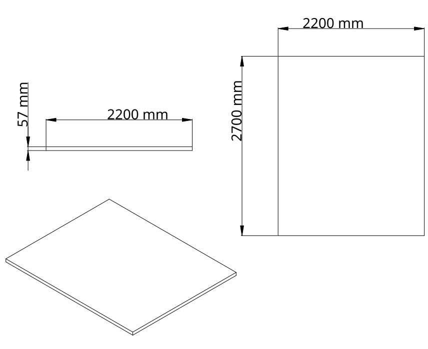

Figure 3.22: Overall pallet dimension.

Configuration 2: M1 Abrams tanks

The second configuration is to carry three M1 Abrams military tanks. It is also possible to carry the three tanks with some extra space for pallets behind the tanks. The total mass of 3 tanks

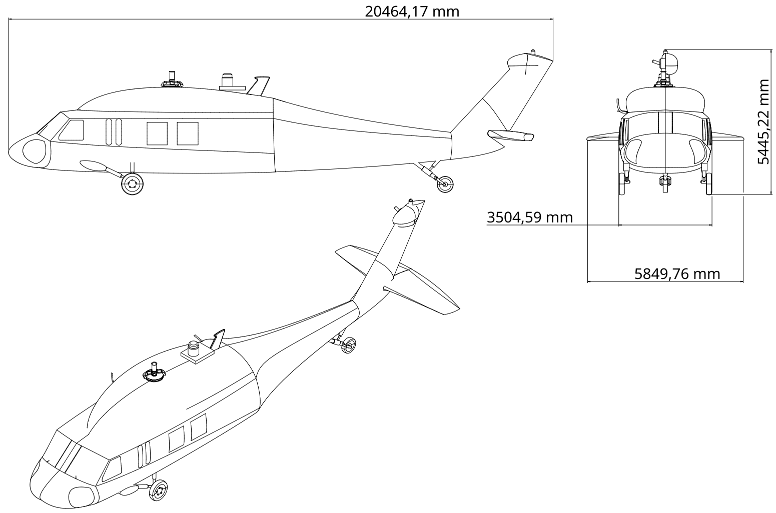

Figure 3.23: Overall H-70 Black Hawk helicopter dimension.

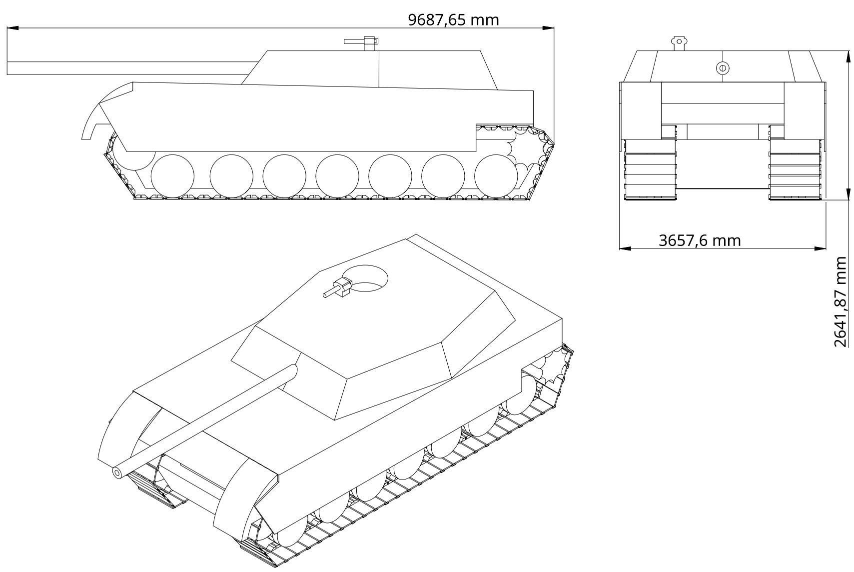

Figure 3.24: Overall M1 Abrams tank dimension.

is 180 000 kg. The configuration on aligning the M1 Abrams tanks can be seen in Figures 3.27.

Configuration 3: Cargo Bay Seating

Based on RFP, the main cargo bay should be able to accommodate for an extra 330 passengers, at least. As seen from the configuration above, almost half is accomodated by deployable fold

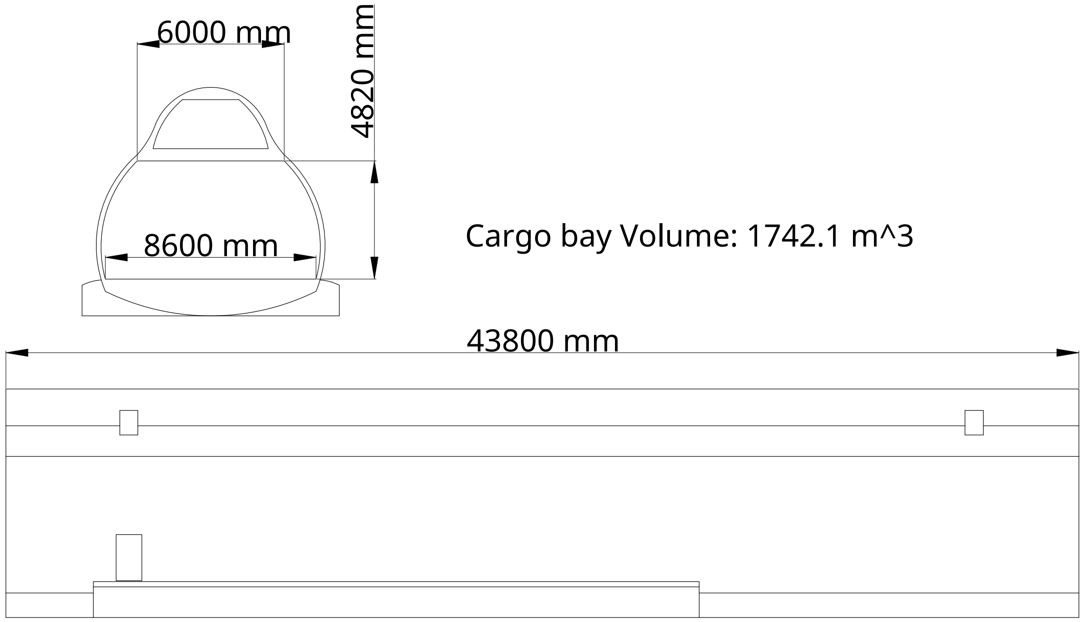

Figure 3.25: Cargo Dimensions

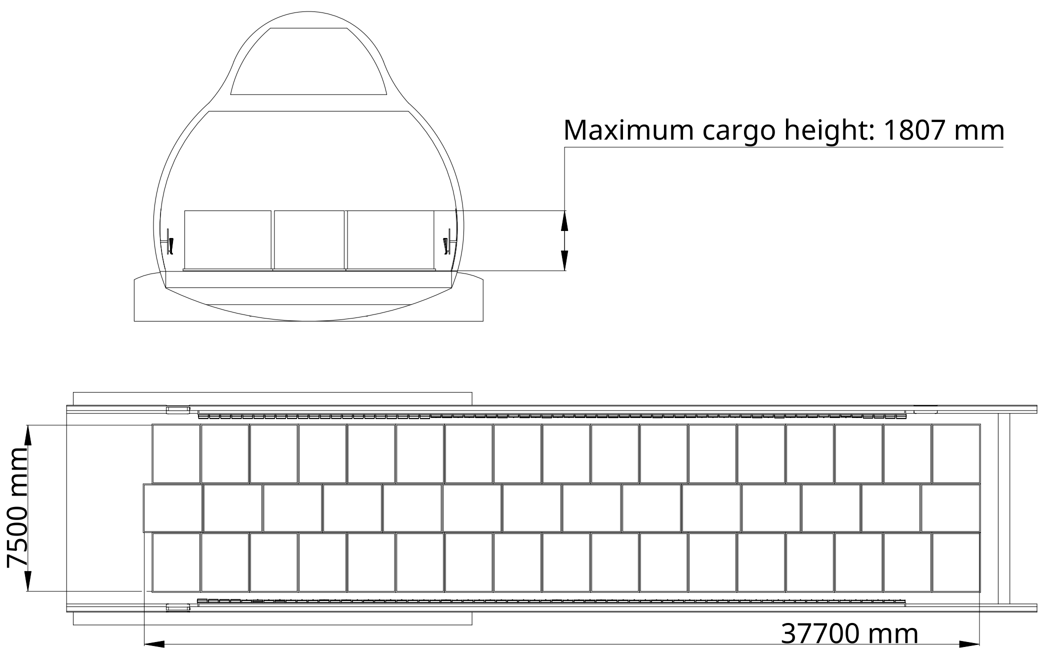

Figure 3.26: Forty-eight of 463L pallets arrangement inside the cargo bay (front and top views).

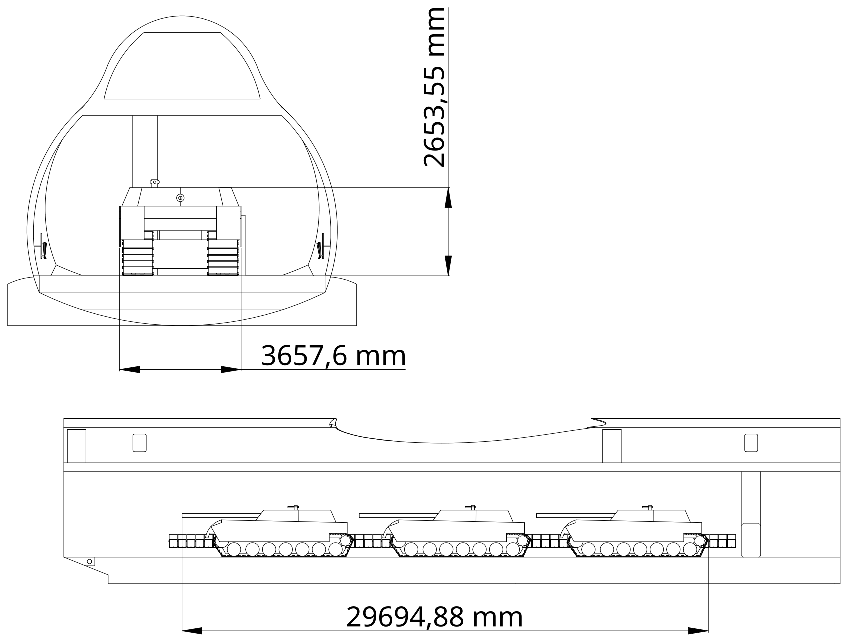

Figure 3.27: Three M1 Abrams tanks arrangement inside the cargo bay (front and side views).

out seats, similar to those found on the Airbus A400M and Chinook Helicopters, that are attached to the walls of the cargo bay. The rest will be accomodated by 11-abreast seating in several rows shown in Figures 3.28. The upper deck arrangements are given in Fig. 3.21.

3.7.3 Area Access of Upper and Lower Cabins

There are 2 ways of accessing the upper deck cabin of BUING. The first is via a staircase near the tail for the access to the 84 passenger seats located at rear upper deck. The second method is via a staircase at the front of the aircraft, near the front ramp, allowing access to the main bridge and cockpit. There is no direct access possible between the two separate cabin areas due to the positioning of the wing, avionics, hydraulics, etc and are separated by 2 bulkheads, 1 in front of the rear cabin and 1 at the rear of the front cabin.

3.8 Hydraulics, Electrical and Environmental Systems

3.8.1 Hydraulics

Four individual hydraulic lines drive the control surfaces, flaps actuation, and landing gear deployment. At least two lines power each control surface, with triple redundancy for the rudder,

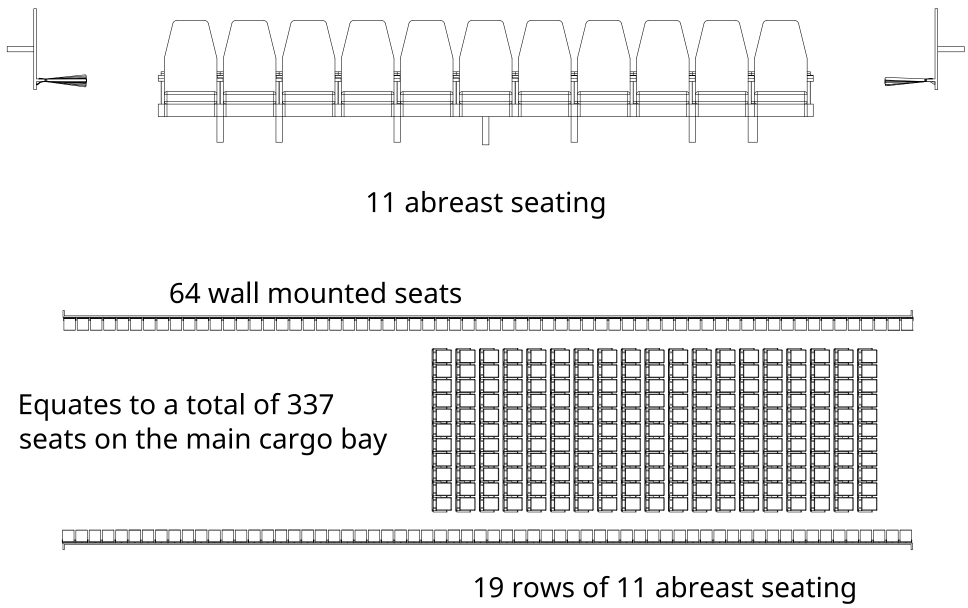

Figure 3.28: Three hundred and thirty passengers seating arrangement inside the cargo bay (front and top views).

due to its importance. Hydraulic pressure is supplied by four engine driven pumps with a backup electric motor pump. To keep the hydraulic fluid clean and consistent, the hydraulic system is installed with filters on the supply and return lines. This system will also incorporate integrated checking systems, such as relief valves to make sure the hydraulic lines do not become over pressurized, which can lead to catastrophic failure in certain, demanding circumstances. Should the hydraulic line that powers all control surfaces be severed, plug valves will ensure that the hydraulic fluid does not leak out. These can be seen in Fig. 3.29.

3.8.2 Electrical

To provide necessary power for various electrical systems, BUING is fitted with redundant energy generation systems. The main energy generation comes from the engines themselves, powering the various flight deck systems. The electric system regulates the hydraulic, engine control, and flight control systems, which are fed via the main electrical power supply. The spatial awareness systems, such as the weather radar and aircraft tracking system, will also be powered by the main power feed. These systems include a weather radar manufactured by Collins Aerospace, to accurately display oncoming weather patterns to the pilots. To start the plane, initial

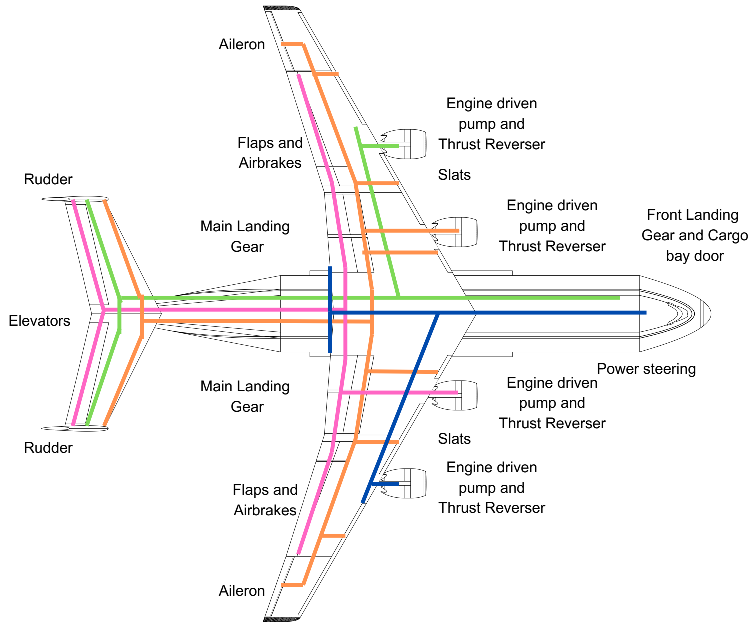

Figure 3.29: Hydraulics Map

electrical power is provided by the on board Honeywell Auxiliary Power Unit (APU), which acts as a smaller turbine engine to provide energy when the engines have been turned off. BUING encourages the traditional centralized method for power distribution where the APU and engine generators feed into a common electronics bay that distributes the power to the on-board electrics. This system is diagrammed in Fig. 3.30.

3.8.3 Environmental

Since BUING will carry passengers in the main Cargo Bay of the fuselage as part of one of its many configurations the Cargo Bay as well as the 2 separate upper cabins are pressurized. A climate control system with air conditioning, heating, and a HEPA filter ensures that the pressurized areas will not become an unworkable setting. The pressurization is achieved using bleed air from the engine's low- and high-pressure compressor stages. The air is first cooled through a precooler, which is an open loop heat exchanger that uses the fan air as the cold fluid that exhausts to the atmosphere. The output air is further cooled through air conditioning packs before passing through a HEPA filter and entering the cabin. The pressurization schematic of BUING is shown below in Fig. 3.31. Additionally, per CFR 14 Part 25 §25.1447, supplemental oxygen is stored in the flight deck as well as rear passenger deck in the event of loss of pressure.

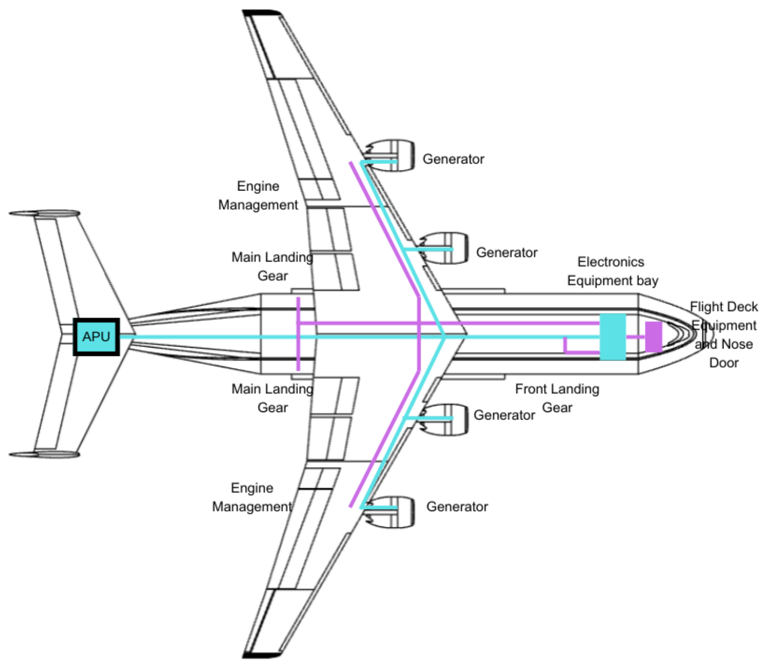

Figure 3.30: Electrical Map

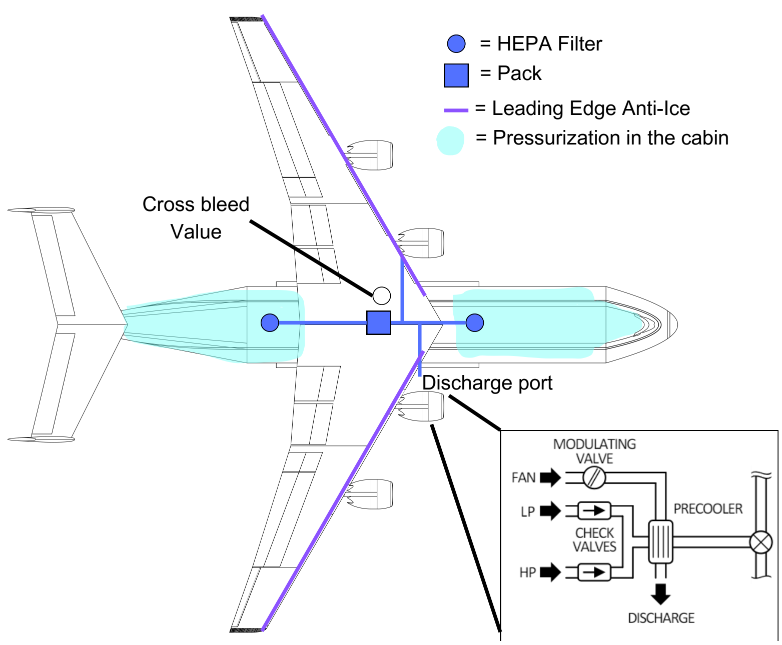

Figure 3.31: Environmental Systems Map

3.9 Emergency System

In the case of flight control failure, there will be redundancy built into this plane's hydraulic systems with backup pumps. In the case of the landing gear is unable to be deployed due to primary hydraulic system failure, a backup compressed air system will be available to the pilots to fire the landing gear into the down and locked position. In another case, if the hydraulics system fails, a secondary set of lines and redundant pump will be included to allow for continued flight control, even if the primary system fails. Targeting a rotor burst case, electrical and hydraulic routing have redundancy built-in through top and bottom mounting as show in Fig. 3.29. In this case, if a rotor burst were to occur, the change of total systems failure would be within 5%. This redundancy is implemented to ensure Valkyrie is certifiable under 14 CFR Part 25 §25.1461. In the event of an unlikely catastrophe, a black box data recording system is fitted towards the rear of the fuselage (more information can be found in [15].

3.10 CG Position of BUING Systems

To estimate the center of gravity (c.g) of the aircraft, the in-built CG location feature on Onshape is used and distributed throughout the cabin. Here, the electrical and pneumatic systems were not included. The tentative location of the c.g of each components is presented in Fig. 3.32. The explanation for the numbering system can be found in Table 3.4.

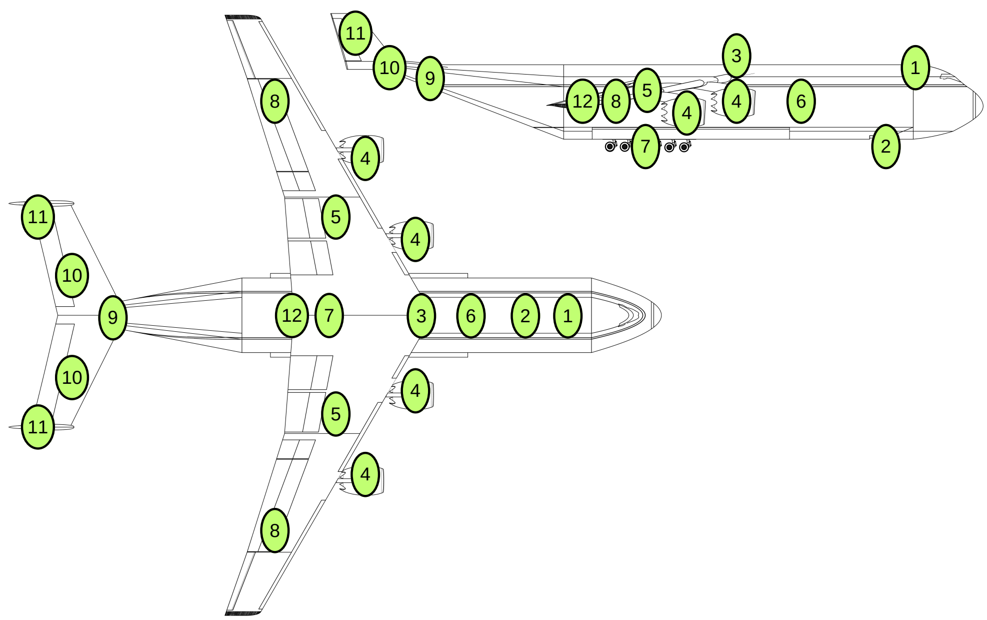

Figure 3.32: Components list - top and side views

Table 3.4: Weight components.

Label No.	Component name
1	Instruments
2	Nose Landing Gear
3	Hydraulics, Electrical and Environmental systems
4	Engines
5	Wing
6	Fuselage
7	Main Landing Gear
8	Fuel System
9	APU
10	Horizontal Stabilizer
11	Vertical Tail
12	Empty Weight Center of Gravity

CHAPTER 4
LANDING GEAR

4.1 Landing Gear Arrangement and Geometry

BUING landing gear will use a tricycle arrangement, just like the Lockheed C-5 Galaxy and Antonov An-225 Mriya. This configuration is practically exclusive to this class of aircraft because of its consistent takeoff, taxiing, and payload loading capabilities. This configuration consists of a large nose landing gear at the front of the aircraft and two main landing gear assemblies under the wings toward the rear of the fuselage. As described in Raymer [2], for aircraft weighing more than 181,440 kg, four bogeys, each with four or six wheels, disperse the entire aircraft load across the runway pavement. It was determined to utilize 12 bogeys, each with 2 wheels, at a design MTOW close to 550,000 kg. This design reduces the pressure on the runway surface during takeoff, landing, and taxiing by distributing the aircraft's weight over a wider area.

Table 4.1: Geometrical parameter of the landing gear.

Parameter	Value
Height (m)	1.5
Tip back angle (degree)	20.89
Clearance angle (degree)	16
Overturn angle (degree)	31.5
Wheelbase (m)	30.11
Wheeltrack (m)	7.11

The landing gear calculations are carried out using the procedures described in Sadrey [16]. The wheelbase, or the distance between the nose and main landing gears, is selected to meet the stability requirements during taxiing, which state that the nose gear must support between 5 and 20% of the entire weight. As explained in detail in [16], the angle of the tip back, given in

Fig. 4.1, must be less than the angle formed by the vertical passing through the main gear and the aircraft's most aft center of gravity. The overturn is maintained above 25° and below 63°, shown in Fig. 4.2. The landing gear geometrical parameters are shown in Table 4.1 and the detail of CAD drawings are open publicly here: https://tinyurl.com/2coujqho.

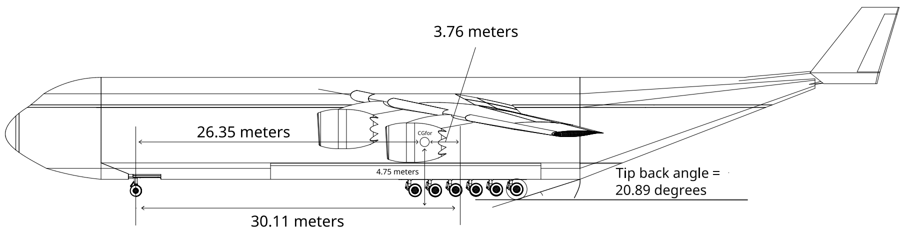

Figure 4.1: Landing gear longitudinal placement.

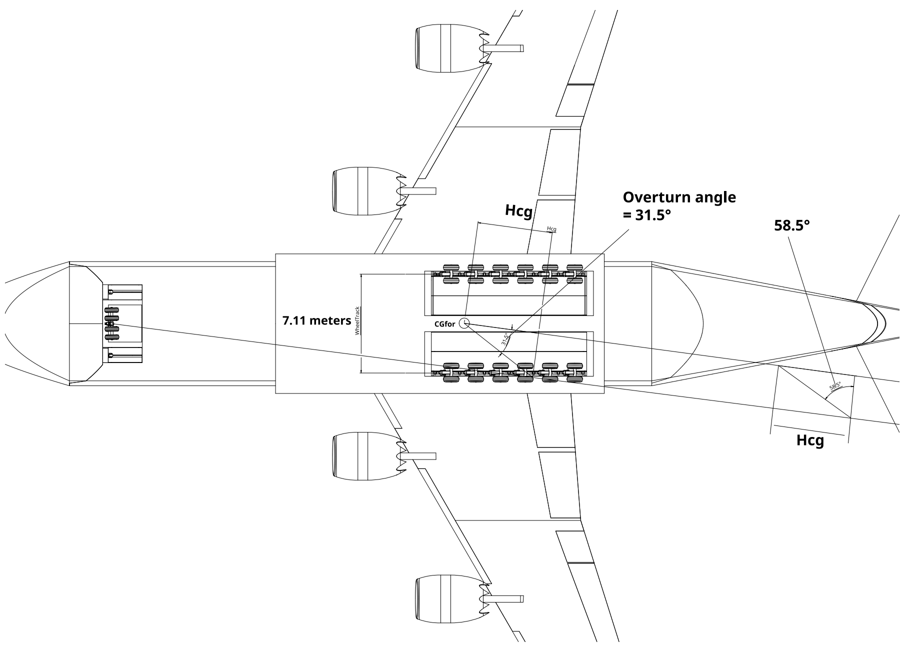

Figure 4.2: Landing gear span-wise placement.

Recalling the unique design of the Antonov An-225 Mriya, the aircraft lowers its nose gear allowing for easier loading of cargo. The aircraft's front can lower into a stable position, making loading easier, by retracting the nose gear. During this operation, extra support struts are deployed to provide the necessary stability and guarantee the plane stays balanced. The only parts of the airplane keeping it suspended are these support struts when the nose gear is fully retracted and lifted off the ground. At this point, the aircraft has a cargo ramp that extends from the front, making it easy to load big, heavy objects. This Mriya-inspired system makes it possible to handle cargo effectively without sacrificing the stability of the airplane. Nose gear retraction and support struts for cargo loading are given in Fig. 4.3.

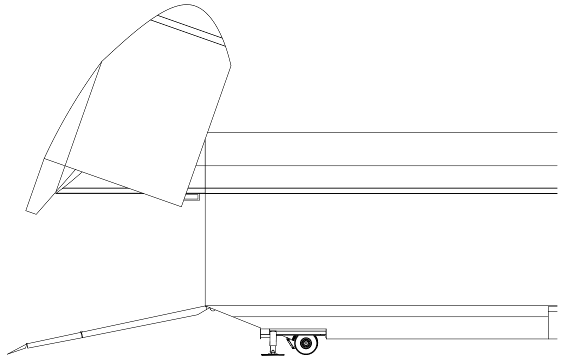

Figure 4.3: Support struts for cargo loading.

4.2 Tire and Wheel Sizing

During takeoff and landing procedures, the tires play a vital role in bearing the aircraft's heavy weight. Tire selection must be done carefully in order to ensure that the tires can support the heavy loads encountered during these flying phases, preventing collapse and potentially catastrophic consequences.

Table 4.2: Static loads of each landing gear.

Parameter	Nose	Main
MTOW (Newton)	$5,399,944$	
Static Load (%)	12.5	87.5
Max Static Load (N)	674992.99	4806344.76
Min Static Load (N)	593599.17	4724950.94

Tire load calculations are usually performed using established methods, as those described in Raymer [2]. The maximum weights that the tires must withstand are calculated using many parameters, including aircraft weight, wheel base, and wheel load geometry. Maximum and minimum static load of each gear are given in Table 4.2. The tires are selected by applying the methodology described in [2], with information obtained from `https://tinyurl.com/29vk9b62`. You can locate them in Table 4.3. Also stated in the [2], tire sizes from similar designs can be replicated for early conceptual design, or a statistical method can be applied.

Table 4.3: Tire and wheel sizing.

Parameter	Nose	Main
Tire Width (mm)	375.412	456.184
Tire Diameter (mm)	1068.832	1214.374
Wheel Diameter (mm)	508	660.4

4.3 Shock Absorber

During landing operations, the landing gears are subjected to significant stresses and vibrations. Strong shock absorbers with the ability to absorb and release energy are essential for controlling these disruptions and reducing oscillations and deformations.

BUING will use an advanced landing gear system with oleo-pneumatic shock absorbers for both the main and nose landing gear components, taking suggestions from the highly regarded C-5 Galaxy and Antonov An-225 Mriya design. Pneumatic spring systems and hydraulic dampening mechanisms are combined in this tried-and-true configuration to provide excellent performance in a variety of operating environments. It aims to provide consistent and dependable performance throughout every phase of flight operations by utilizing this tried-and-true design.

Table 4.4: Oleo outer diameter.

Landing Gear	Diameter (mm)
Nose	291.592
Main	252.476

Stated in Raymer's Section 11.4.3, the internal pressure of compressed air applied across a piston allows the oleo to support its load. An oleo's internal pressure P is typically 1800 psi, or 12,415 kPa. The equation force = pressure $\times$ area can be used to calculate internal diameter. Since the external diameter is usually 30% bigger than the piston diameter, Raymer's Eq. 11.13 can be used to approximate the external oleo diameter. Table 4.4 provides the calculated external diameters of the nose and main gear oleo.

4.4 Gear Retraction and Storage

With the Antonov An-225 Mriya as guidance, the landing gear system's retraction and storage mechanisms have been carefully considered in order to achieve maximum performance and safety under a variety of operating circumstances.

4.4.1 Nose Gear Retraction

The aircraft's nose gear retracts in the direction of the rear, as shown in Fig. 4.4. Comparing this retraction direction to forward retraction, there are a number of benefits. A simpler mechanism is usually needed when the nose gear retracts backward, which can improve reliability and make maintenance simpler. Aerodynamically speaking, backward retraction causes less disruption to the airflow, which may increase fuel efficiency while in flight. Because the gear retracts backward and away from the impact direction, it also helps to lessen the chance of shearing during landing. Furthermore, the aircraft achieves better weight distribution and a more balanced center of gravity by retracting the gear toward the rear, which can improve flying stability.

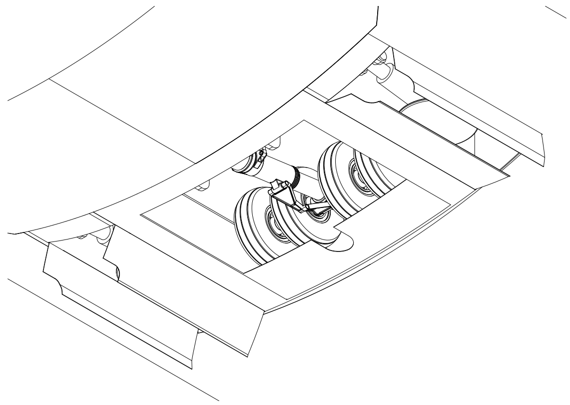

Figure 4.4: Nose gear storage.

4.4.2 Main Gear Retraction

The main landing gear retracts inside the aircraft's fuselage, shown in Fig. 4.5, attempting the design of the landing gear on the An-225 Mriya. The main landing gear retracts by rotating around its connection points and folding inward toward the fuselage's midline. This arrangement helps to maintain the aircraft's aerodynamic cleanliness while in flight by making the most use of the space inside the landing gear bays and making it easier to store the landing gear inside the aircraft's structure.

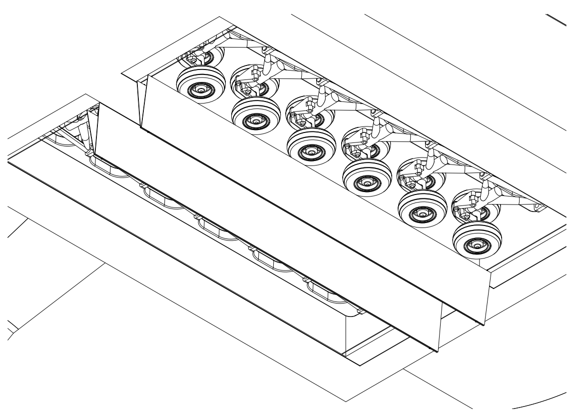

Figure 4.5: Main gear storage.

The goal is to achieve robustness, dependability, and aviation standard compliance in the landing gear retraction and storage systems by implementing these design ideas from the An-225 Mriya landing gear system. Depicted in Fig. 4.6 is the landing gear retraction sequence.

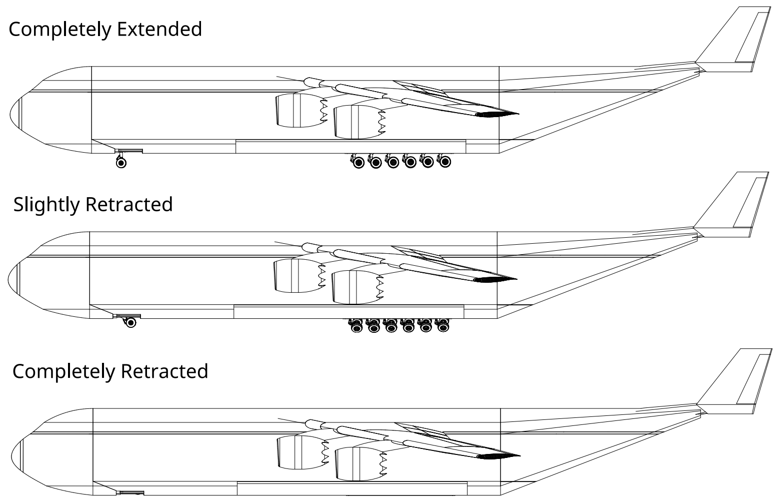

Figure 4.6: Landing gear retraction sequence.

CHAPTER 5 COCKPIT AND AVIONICS

5.1 Cockpit Arrangement

Based on Roskam's [6] and Gudmundsson's [13] works, the BUING cockpit layout takes ergonomics and human aspects into account. Its layout, intended for use on bomber and cargo aircraft, maximizes the performance of the pilot, co-pilot, and crew over extended flight duration. Reference eye point is used to calculate sitting inclinations and measure distances from reference eye point to flight control and instrument panel. The cockpit arrangement is depicted in Fig. 5.1. The CAD drawings are open publicly at `https://tinyurl.com/24koyp77`.

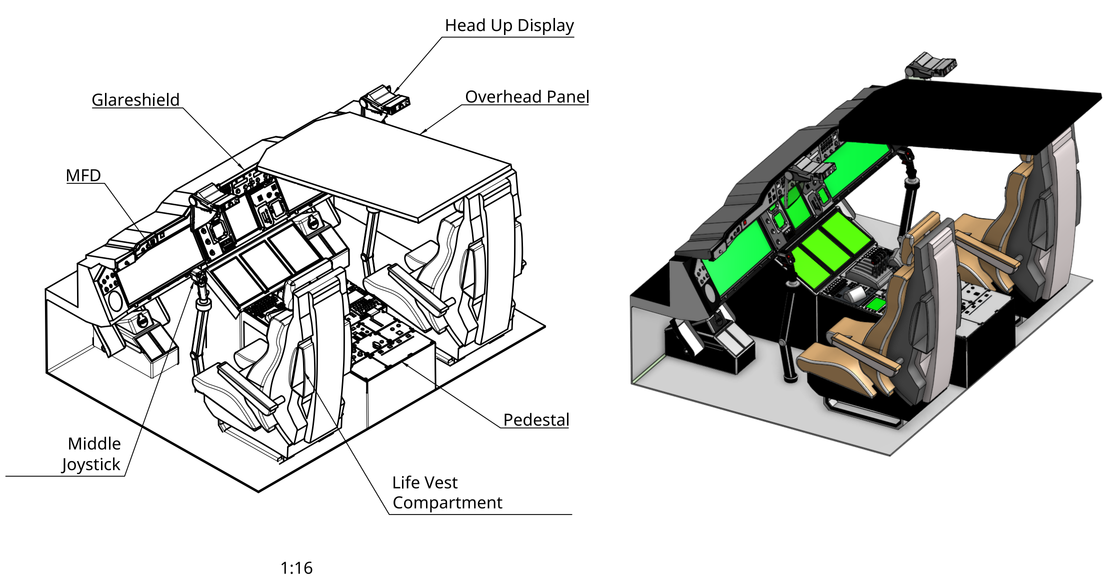

Figure 5.1: Cockpit arrangement.

5.2 Seat Arrangement

Seat design and distances to the flight control and instrument panel are also based on the works of Roskam [6] and Sadrey [16]. By applying the ergonomic cockpit arrangement, BUING intended to support the crew's work by reducing unnecessary movement to reach the control or instrument panel. The reference eye point is used as the starting point for drawing lines and calculating distances to the instrument panel, rudder pedal, and middle joystick of the flight control system. The configuration of the seats and controls is inspired by the works of Roskam. Figs. 5.2, 5.3 & 5.4, respectively, shows the layout of the instrument panel and seat control as well as the distance and space between the seats. .

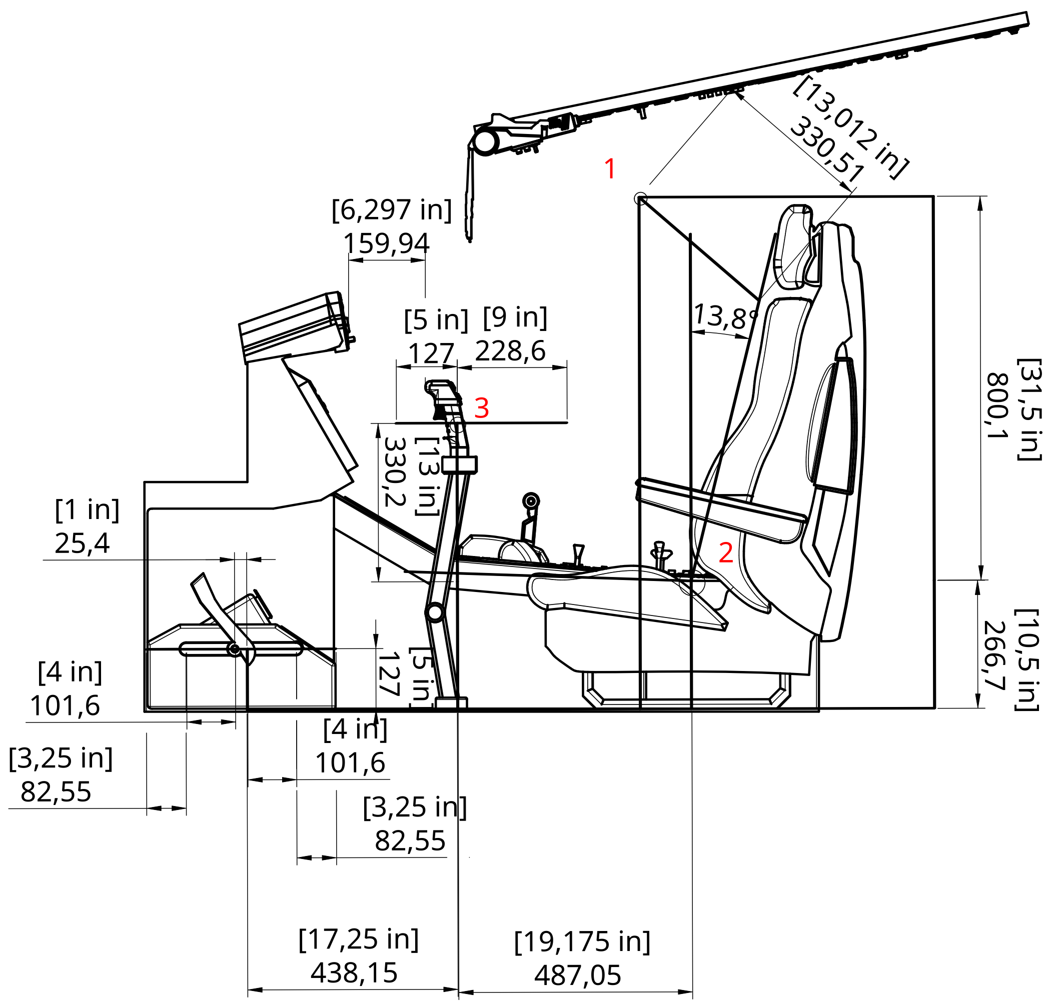

Figure 5.2: Seat to flight control and instrument panel arrangement in millimetre; (1) pilot eye position, (2) neutral seat reference point, (3) yoke reference point arc.

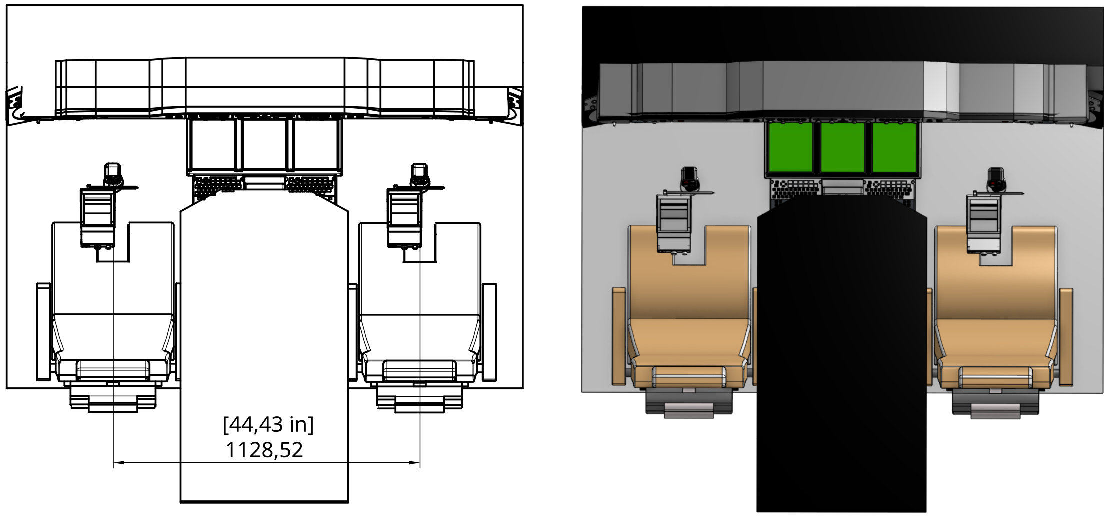

Figure 5.3: Seat distance (in mm).

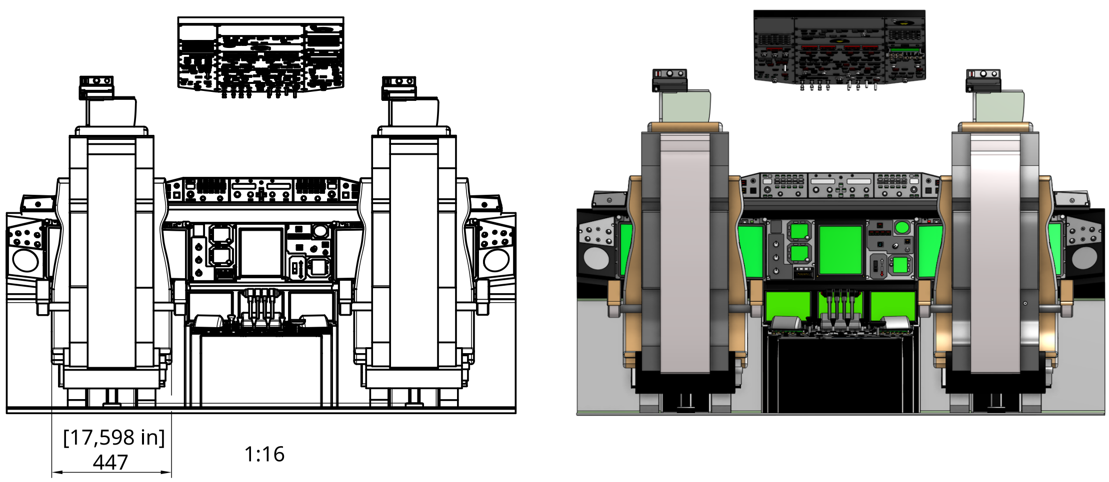

Figure 5.4: Seat width (in mm).

5.3 Crew's Visibility Optimization

Assuring the crews have unobstructed vision following Visual Flight Rules (VFR) allows them to keep an ideal viewpoint of the aircraft's surroundings from both a vertical (downward and upward) and horizontal (port and starboard) standpoint. This visibility is essential for the pilot to be able to see the ground path during important stages including takeoff, landing, and taxiing referring on Airworthiness Standard: AS 580 B. Optimized BUING visibility Pattern is shown in Fig. 5.5. The method used is by drawing manual angles through Onshape.

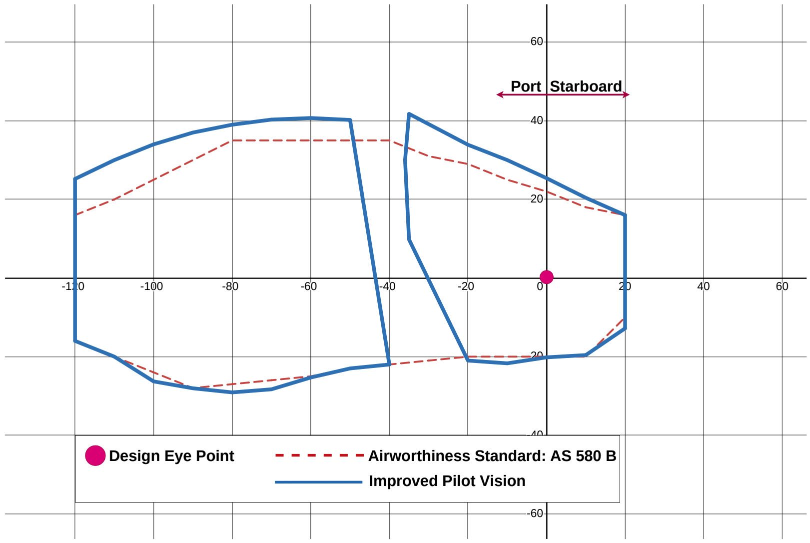

Figure 5.5: Optimised visibility pattern from port side.

5.4 Flight Crew's Outside Visibility

As stated in [13] regarding the ideal pilot field of view, optimizing the flight crew's exterior visibility is crucial for safe operations, especially during crucial stages such as takeoff, taxiing, and landing. The vertical side view visibility is shown in Fig. 5.6, and horizontal view in Fig. 5.7.

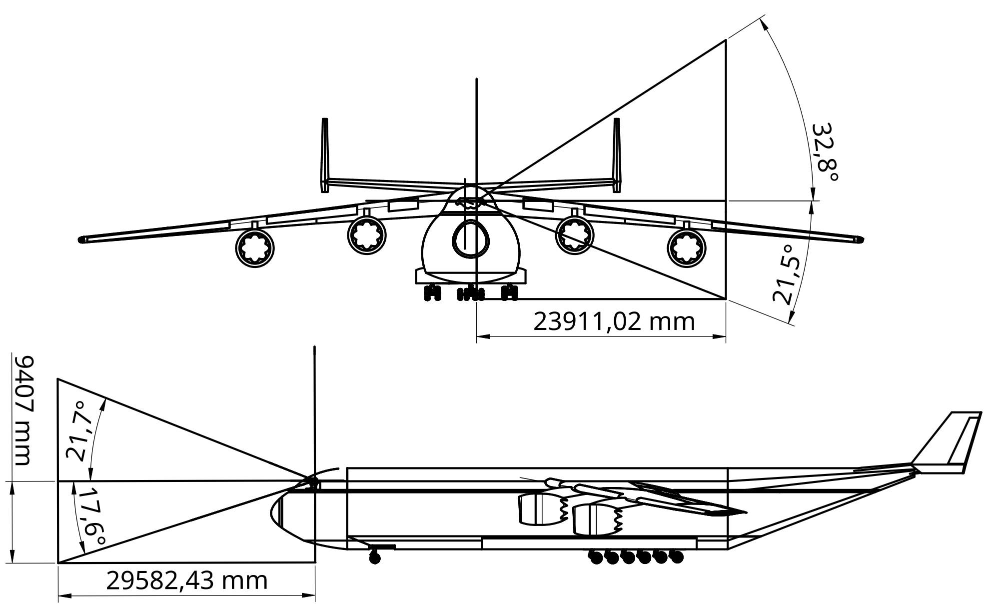

Figure 5.6: Side and forward vertical visibility.

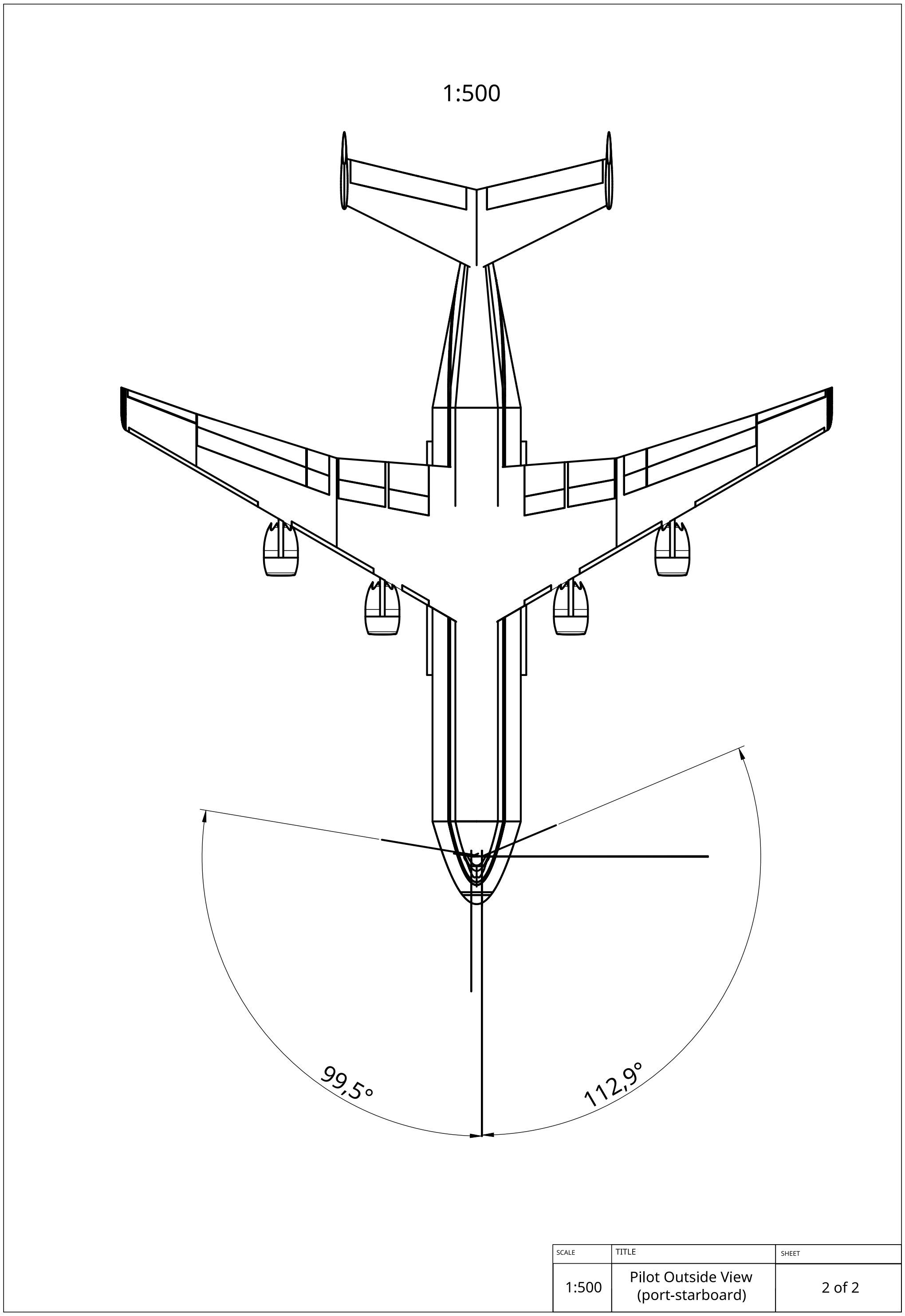

Figure 5.7: Horizontal side view.

5.5 Avionics Integration

To reduce flight crew fatigue, BUING employs an Integrated Avionics System with a glass cockpit. To keep the heavy-lift aircraft airworthy throughout the duration of the objectives, BUING integrates conventional avionics with both military and civil avionics. The proposed Avionic system are shown in Tables 5.1, 5.2, 5.3, 5.4. The selection of the flight management system and the flight control system are expected to support autopilot operations.

Table 5.1: Avionics list: Part 1

Required System	Product	Brand
Weather radar GPS / Navigation Systems INS TACAN Flight Management	Flight2 avionics system	Collinsaerospace
Flight Control System	FCS-7000 Flight Control system	Collinsaerospace
Multi functional display (LCD)	MFD-4820 Large Area Display	Collinsaerospace
Head Up Display	LiteWave ® Head-Up Display	BAE Systems
Terrain radar	AN/APN-209	Raytheon
VHF/UHF Radio Transceiver, Communication Systems	AN/ARC-210 radio system	Collinsaerospace

Table 5.2: Avionics list: Part 2

IFF Transponder	AN/APX-119 Identification Friend or Foe (IFF) transponder	Raytheon
SATCOM	IRT NX SATCOM System for Iridium ®	Collinsaerospace
Video Cameras	Taxi-Aid and Landscape Camera System	Collinsaerospace
	Cabin Video Monitoring System (CVMS)	
Radar/Threat warning system, Electronic Support and Protection Systems	AN/ALQ-214 Integrated Defensive Electronic Countermeasures (IDECM) system	L3HARRIS
Weapon/Countermeasures Systems	AN/ALQ-131 Electronic Countermeasures (ECM) Pod AN/AAQ-24(V) DIRCM (Directional Infrared Countermeasure)	Northrop Grumman
Electro-Optic and Infrared Systems	LITENING Advanced Targeting Pod	Northrop Grumman
Load Planning and Management Systems	Advanced Cargo Loading and Delivery System (ACLADS)	Collinsaerospace
Electronic Publications Bag	Electronic Cabin Bag (ECB)	Collinsaerospace
De-Icing/Anti-Icing Systems component	Vibrating probe ice detectors and magnetostrictive ice detectors (MID)	Collinsaerospace
APU	HGT-1700	Honeywell

Table 5.3: Avionics list: part 3

Required System	Product	Brand	Advantage
Weather radar	Flight2 avionics system	Collinsaerospace	Detect dangers to flight caused by weather, traffic, topography, and navigation. automatically identified these risks and gave flight crews full situational awareness and advice on how to avoid them. Its high level of integration and commercial off-the-shelf (COTS)
GPS / Navigation Systems			
INS			
TACAN			
Flight Management			
Low-Level Wind Shear Alert System	Vaisala MIDAS IV LLWAS	Vaisala	Automated Weather Observing System (AWOS) and early identification of wind shear dangers
Flight Control System	FCS-7000 Flight Control system	Collinsaerospace	Offers a breakthrough in sustainability, redundancy, performance, and capability. significantly increases stability and safety during airdrops, air refueling, and all-in-flight activities
Multi functional display (LCD)	MFD-4820 Large Area Display	Collinsaerospace	The resistive multi-touch surface is designed to prevent accidental touchscreen activations when using gloved hands. An 8 by 20-inch monolithic liquid crystal display (LCD) is part of the MFD-4820. removes the central mullion, which can cause visual chatter or center-area blurriness in two side-by-side screens.
Head Up Display	LiteWave® Head-Up Display	BAE Systems	With LiteWave, pilots may move around in their seats more comfortably without worrying about losing sight of the symbolism. Pilot comfort is increased by this increased range of motion, particularly on extended flights.
Terrain radar	AN/APN-209	Raytheon	Founded on the Radar Altimeter Common Core (RACC) engine, which has been thoroughly tested in flight on the Joint Strike Fighter and fielded to customers.
VHF/UHF Radio Transceiver, Communication Systems	AN/ARC-210 radio system	Collinsaerospace	Provides capabilities defined by software. It is made to continue evolving as missions and demands do.
IFF Transponder	AN/APX-119 Identification Friend or Foe (IFF) transponder	Raytheon	Possess an adaptable, open systems architecture that allows for better safety and cooperative identification across a variety of aircraft platforms.
SATCOM	IRT NX SATCOM System for Iridium®	Collinsaerospace	The Iridium® global network of more than 70 satellites suit your demands in terms of broadband while in the air, offering less weight, drag, and power consumption together with high data throughput capacity.

Table 5.4: Avionics list: part 4

Required System	Product	Brand	Advantage
Video Cameras	Taxi-Aid and Landscape Camera System	Collinsaerospace	Increases pilot visibility outside the aircraft during taxi operations, which improves safety. A camera attached to the aircraft's vertical stabilizer offers a view of the main landing gear, wings, and fuselage, while a camera installed on the belly of the system allows a view of the nose landing gear.
	Cabin Video Monitoring System (CVMS)		The flight crew can have complete situational awareness by integrating cameras from the Flight Deck Entry Video Surveillance System (FDEVSS) into the CVMS.
Radar/Threat warning system, Electronic Support and Protection Systems	AN/ALQ-214 Integrated Defensive Electronic Countermeasures (IDECM) system	L3HARRIS	Created to resist RF-guided threats by using electronic countermeasures (ECM) that have been shown to be effective in denying, interfering with, delaying, and compromising launch and engagement sequences. Every threat is recognized, given a priority, countered, and presented to the crew members for their own safety and situational awareness.
Weapon/Countermeasures Systems	AN/ALQ-131 Electronic Countermeasures (ECM) Pod	Northrop Grumman	Uses precise parametric measurements to detect and identify known, emerging, and future dangers in a dense, complex threat environment. It then applies the best coherent and/or non-coherent jamming strategy to defeat the threat system.
	AN/AAQ-24(V) DIRCM (Directional Infrared Countermeasure)		All current infrared danger bands (I, II, and IV) are simultaneously jammed and threats are detected quickly and accurately. A single generic jam waveform is used to counter all infrared missile threats.
Electro-Optic and Infrared Systems	LITENING Advanced Targeting Pod	Northrop Grumman	High-definition digital video in color, black and white, numerous infrared bands, and advanced picture-in-picture technology that can show up to three perspectives at once
Load Planning and Management Systems	Advanced Cargo Loading and Delivery System (ACLADS)	Collinsaerospace	Load planning, weight and balance computations, and flight management system integration are all included in integrated software as a single package. integrates wireless operation with electronic monitoring to streamline labor-intensive manual procedures like preflight, loading, and airdrop operations.
Electronic Publications Bag	Electronic Cabin Bag (ECB)	Collinsaerospace	Accurate stock levels are guaranteed via real-time inventory management. With eCB, contactless interactions are safer since there are less unnecessary passenger, inventory search, and staff interactions.
De-Icing/Anti-Icing Systems component	vibrating probe ice detectors and magnetostrictive ice detectors (MID)	Collinsaerospace	Ferromagnetic materials' capacity to alter their dimensions in response to a changing magnetic field. Ultrasonically, magnetostrictive sensors vibrate at a predetermined resonance frequency.
APU	HGT-1700	Honeywell	Delivers 1300 kW shaft power at only 335 kg of weight. Used primarily on the A350 XWB, it showcases a 10% reduction in specific APU fuel use as well as Carbon Monoxide emissions. Its Variable speed provides a reduced fuel burn and emissions with a lower weight on it systems. Making it the most energy efficient APU in its class.

CHAPTER 6 PROPULSION

6.1 Engine Selection

The propulsion system for BUING is carefully crafted to install four turbofan engines Rolls-Royce Trent-1000, as shown in Fig. 6.1. We've placed significant emphasis on performance, efficiency, and reliability, making the Engines Rolls-Royce Trent series the perfect fit for our needs. These engines boast impressive thrust capabilities, low specific fuel consumption, and a minimized environmental footprint, aligning perfectly with our project goals. This link `https://tinyurl.com/2yycsnqt` contains engine data set and relevant information that were used in selecting the engine.

In selecting the Engines Rolls-Royce Trent-1000 engines for BUING, several factors were taken into account. Firstly, the thrust requirement for our aircraft stands at approximately ~ 1200 kN, estimating from the initial sizing analysis in Section 1.5 for $T/W = 0.25$. Each Rolls-Royce Trent-1000 engine delivers a thrust of 360.4 kN, summing up to a total thrust of 1441.6 kN, as detailed in Table 6.1. This not only meets but exceeds our required thrust, providing us with ample power to achieve optimal performance.

6.1.1 Engine Candidates

In order to choose the best turbofan engine for BUING we had to choose a several engines which they have a thrust bigger than 100 kN. After we choose the engines that have thrust bigger than 100 kN, we start choosing the engines that have a thrust Bigger than 200 kN, and start doing performance and TSFC calculations to choose or have the best candidates for our BUING to see our spreadsheet for necessary computations.

Furthermore, we meticulously evaluated the Total Specific Fuel Consumption (TSFC) data,

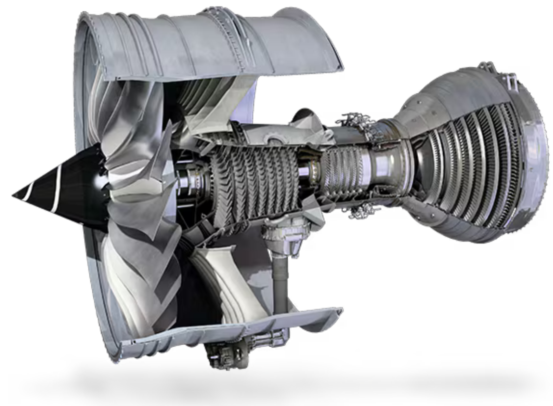

Figure 6.1: Rolls-Royce Trent-1000 [3].

Table 6.1: Rolls-Royce Trent-1000 specifications [4, 5].

Thrust (kN)	360.4
Continuous Thrust (kN)	324.36
Total Thrust (kN)	1441.6
Length (m)	4.738
Fan Diameter (cm)	285
Dry Weight (kg)	$5,936 - 6,120$
TSFC 1/h (cruising)	0.505
Bypass Ratio	≈ 10.1
Overall Pressure Ratio	$50:1$
Thrust/Weight Ratio	6.01
First Run	14 February 2006

converting $\frac{\mathrm{g}}{\mathrm{kNs}}$ to $\frac{1}{\mathrm{h}}$, to ensure that our engine selection aligns with our objectives of maximizing performance while minimizing fuel consumption. By choosing the Rolls-Royce Trent-1000 engines, we can achieve the right balance between power output and fuel efficiency.

In summary, the Rolls-Royce Trent-1000 engines emerged as the most suitable choice for BUING due to their exceptional thrust capabilities, low specific fuel consumption, and compatibility with our performance and efficiency goals.

6.2 Engine Characteristics

The Trent 1000 engine represents a pinnacle in aviation engineering, merging innovation with reliability for modern air travel demands [4]. It comprises three coaxial shafts:

- The low-pressure shaft, boasting a 2.85-meter fan powered by six axial turbines, ensures robust propulsion.
- The intermediate pressure spool, with eight axial compressors and a single turbine stage, facilitates seamless operation.

- The high-pressure compressor, driven by a solitary turbine stage, prioritizes efficiency .

An Electronic Engine Controller (EEC) ensures precise performance. Originally, Boeing considered exclusively partnering with GE Aviation for the 787's engine. However, responding to market demands, Boeing embraced diversity, allowing integration with both GE and Rolls-Royce engines, offering airlines unprecedented flexibility with necessary modifications.

The Trent 1000 program is a collaboration among six partners, sharing risks and rewards for excellence and innovation: Kawasaki Heavy Industries, Mitsubishi Heavy Industries, Industria de Turbo Propulsores, Carlton Forge Works, Hamilton Sundstrand, and Goodrich Corporation.

Inspired by predecessors like the Trent 8104, the Trent 1000 adopts a ”more-electric” engine paradigm, featuring a bleed-less design and a meticulously crafted fan for optimal airflow efficiency and increased bypass ratio. Efficiency is further improved with a high-pressure ratio and contra-rotating spools, simplifying maintenance and reducing costs. A tiled combustor highlights its commitment to emissions reduction and environmental sustainability.

6.3 Engine Performance

In our engine performance calculations, we considered Mach number, various altitude, throttle ratio, temperature ratio, and pressure ratio, in order to have the best and accurate engine performance, with low TSFC, as shown in Fig. 6.2.

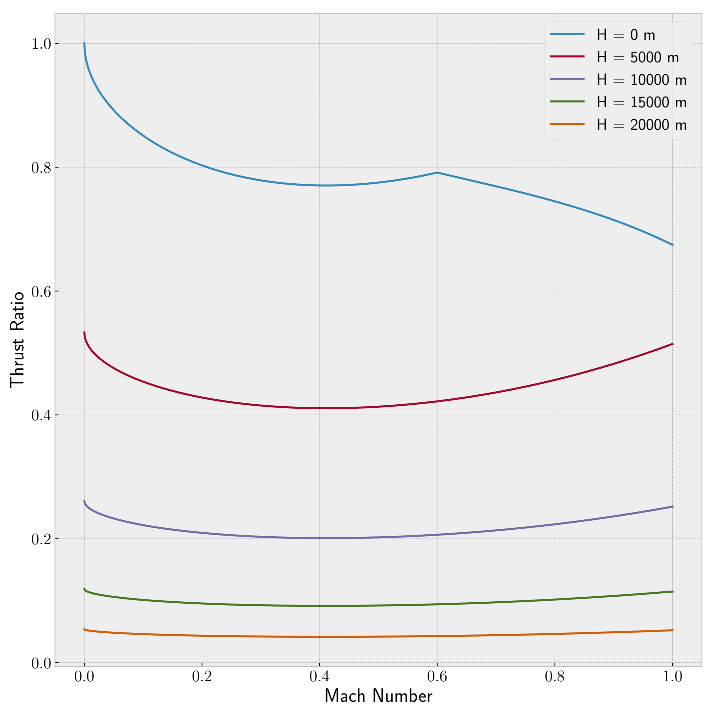

Figure 6.2: Thrust ratio vs Mach number with various altitudes.

The references [13, 17] provides methods for estimating the impact of altitude and airspeed on turbofan engine thrust. The results in Fig. 6.2 were used when computing the performance in Chapter 7.

The thrust ratio is crucial for assessing the efficiency and performance of an aircraft's propulsion system, especially at higher altitudes. As altitude increases, the thrust ratio's importance grows, affecting variables like fuel consumption, engine efficiency, and overall flight dynamics. Understanding these relationships is essential for optimizing aircraft performance and fuel efficiency across varying flight conditions.

CHAPTER 7 PERFORMANCE

7.1 Mission Profile

The mission profile of BUING, as shown in the attached Fig. 1.7, is designed for cargo aircraft and prioritizes large and heavy payloads. According to the Request for Proposal (RFP), these payloads consist of up to 330 passengers, 48 463L pallets, and three M1A2 Abrams Main Battle Tanks. The request for proposals outlines three distinct mission profiles: maximum payload of 430,000 lb (195,045 kg), transport payloads up to 295,000 lb (133,810 kg), and ferry mission.

Under normal operating conditions, BUING aircraft cruise at Mach 0.75 and climb to its cruising altitude of 31,000 feet (9,448.8 m). The aircraft then begins its descend to an alternate elevation of 15,000 feet (4,572 m) in preparation for a 100 nm (185 km) reserves cruise. If an instrument approach is required, a 45-minute loiter phase is carried out at an altitude of 5,000 ft (1,524 m) prior to landing.

This meticulously outlined mission protocol adheres to stringent operational standards and underscores BUING's capacity to fulfill diverse cargo transport requirements efficiently and reliably. The ratio $\left(\frac{w_5}{w_4}\right)$ in Table 7.1 is the residual fuel fraction after the fuel for other segments are firstly allocated and can be calculated using Eq. 7.1. This residual is the fuel portion used to calculate the range as given in the Segment 4 to 5 in the nominal mission profile given by Fig. 1.7.

$$\frac{w_5}{w_4} = \frac{\frac{w_{11}}{w_{10}}}{\frac{w_1}{w_0}\frac{w_2}{w_1}\frac{w_3}{w_2}\frac{w_4}{w_3}\frac{w_6}{w_5}\frac{w_7}{w_6}\frac{w_8}{w_7}\frac{w_9}{w_8}\frac{w_{10}}{w_9}\frac{w_{11}}{w_{10}}} \tag{7.1}$$

Table 7.1: Weight ratio for each of the segments of the mission profile. The assumed values of the weight ratio are taken from [6]— military transport aircraft. The cruising to alternate and the loitering weight ratios are calculated using the Breguet formula for jet aircraft [7].

No	Mission Segment	Symbol	Weight Ratio
1	Engine, Start, Warm-up	$\left(\frac{w_1}{w_0}\right)$	0.990
2	Taxi	$\left(\frac{w_2}{w_1}\right)$	0.990
3	Takeoff	$\left(\frac{w_3}{w_2}\right)$	0.995
4	Climb	$\left(\frac{w_4}{w_3}\right)$	0.980
5	Cruising	$\left(\frac{w_5}{w_4}\right)$	Residual
6	Descent (attempt to land)	$\left(\frac{w_6}{w_5}\right)$	0.990
7	Re-climb	$\left(\frac{w_7}{w_6}\right)$	0.980
8	Cruising to alternate	$\left(\frac{w_8}{w_7}\right)$	100 nmi
9	Loitering	$\left(\frac{w_9}{w_8}\right)$	45 minutes
10	Descent	$\left(\frac{w_{10}}{w_9}\right)$	0.990
11	Landing, Taxi, ShutDown	$\left(\frac{w_{11}}{w_{10}}\right)$	0.992

7.1.1 Maximum Payload

As seen in Fig. 1.7, BUING's mission profile is designed to comply with the requirements of cargo aircraft operations. The main mission profile described in the RFP requires an unrefueled range of at least 2,500 nm (4,630 km) on internal fuel, reserves included. The operational parameters of BUING meet and even surpass these requirements. BUING is designed to go 3,088 nm (5,720 km) at a speed 0.75 Mach while cruising at an altitude of 31,000 ft (9,448.8 m). This capability exceeds the minimal specifications outlined in the RFP, demonstrating BUING's suitability for long-haul operations.

7.1.2 Payload at 295,000 lb

Another performance that BUING need to comply based on the RFP is that, being able to reach a maximum range of 5,000 nm (9,260 km) plus reserves with a payload capacity of 295,000 lb (133,810 kg).

7.1.3 Ferry Mission

The required mission profile for BUING requires that a ferry mission must have a minimum range of 8,000 nm (14,816 km) without refueling. Surprisingly BUING exceeds this requirement due to the integration of four Rolls Royce Trent 100 engines, achieving an unrefueled range of 8,107 nm (15,014 km).

7.2 Lift and Drag Polar

Table 7.2: Parabolic lift-drag polar of BUING.

Configuration	C_{D_0}	k
Cruising	0.01941	0.04190
Takeoff	0.06117	0.04415
Landing	0.05957	0.04028

Coefficient lift C_L in Chapter 2 shows the lift and drag polar of BUING. Three configurations can be found in the referred figure that represent the aircraft: the first is for cruising, where $\delta_f = 0^o$ and $\delta_s = 0^o$; the second is for take-off, where $\delta_f = 30^o$ and $\delta_{fs} = 15^o$; and the third is for landing, where $\delta_f = 40^o$ and $\delta_s = 15^o$, each configuration with a different k and C_{D_0}.

Despite the similarity of the plot, as shown in Fig. 7.1 each describe different aspects of aircraft performance. The first one is $\left(\frac{C_L}{C_D}\right)$ ratio shows the efficiency at which an aircraft may continue to fly while using the least amount of fuel, which is an indication of the maximum endurance of the aircraft. secondly, the $\left(\frac{C_L^3}{C_D^2}\right)$ ratio corresponds to the least power needed, which is crucial for maximizing the performance of the aircraft during low-speed activities like takeoff and landing. Finally, the $\left(\frac{C_L}{C_D^2}\right)$ graph is essential for determining the aircraft's maximum range and proving that it can continue to fly for extended periods of time while using the least amount of fuel. As a result, every graph has a distinct analytical function and provides information on various aspects of aircraft performance and aerodynamic efficiency.

An aircraft's aerodynamic performance can be differentiated by comparing configurations at different δ_f and δ_s settings. The analysis indicates that the configuration with $\delta_f = 0^o$ and $\delta_s = 0^o$, known as the clean or cruising configuration, has the steepest slope with respect to the $\left(\frac{C_L}{C_D^2}\right)$ ratio. In terms of performance efficiency, this configuration is followed by the landing configuration ($\delta_f = 40^o$ and $\delta_s = 15^o$) and the takeoff configuration ($\delta_f = 30^o$ and $\delta_{fs} = 15^o$).

The main difference between these plot is how they affect the $\left(\frac{C_L}{C_{D^2}}\right)$ ratio when the aircraft is in cruise, which is directly related to its maximum range. Better aerodynamic efficiency is indicated by the clean configuration's noticeable slope rise, which is essential for improving the aircraft's range. The excellent lift-to-drag characteristics, which are essential for extended flight operations, are the source of this efficiency.

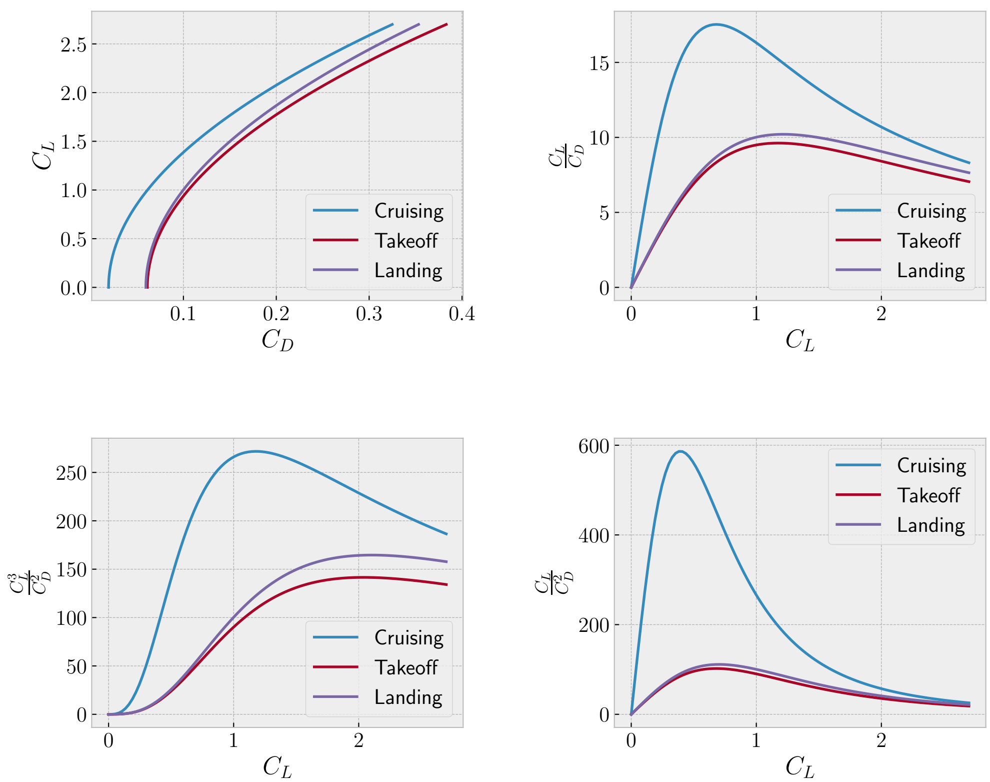

Figure 7.1: Aerodynamics coefficient ratios.

7.3 Payload Range

The relationship between the BUING aircraft's payload (kg) and operational range (km) at both the 550,453 kg Maximum Takeoff Weight (MTOW) and the 205,453 kg Extended Maximum Takeoff Weight (EMTOW),is shown in Fig. 7.2. The maximum payload that the aircraft can accommodate is 195,000 kg, when carrying a full payload, the airplane may travel a maximum of 5,720 km from point A to point B (red line). Then, the section from point B to point C (purple line) shows a decrease in payload and an increase in the overall fuel load of the aircraft, allowing the aircraft to reach a range of 12,000 km. Lastly, the area between points C and D (green line) represents the ferry range, which is 15,014 km for an airplane with a maximum fuel load of 234,455 kg.

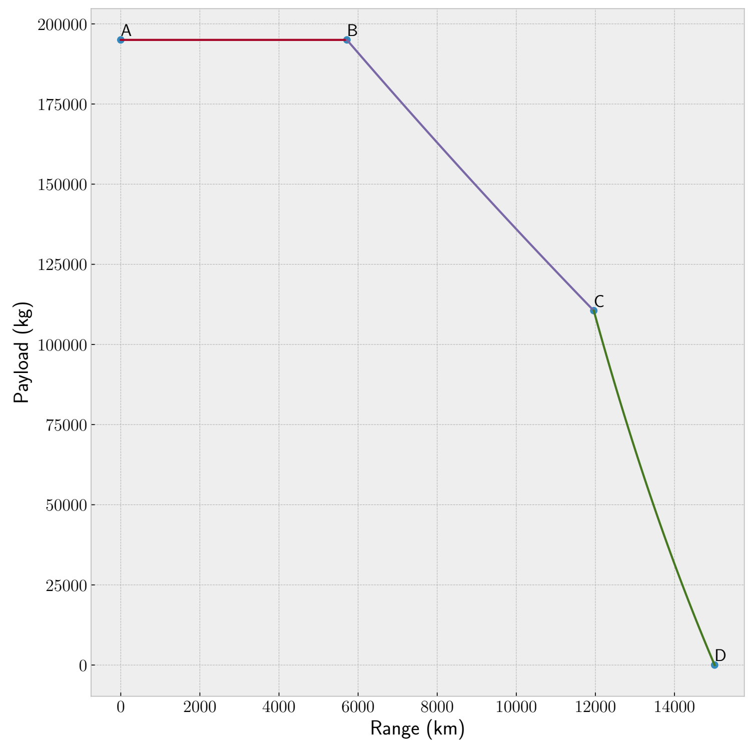

Figure 7.2: Payload range.

7.4 Airfield Performance

Airfield Performance is referring to the operating capabilities of fixed-wing and helicopter aircraft, with an emphasis on their effectiveness and economic viability in a range of airfield conditions. This section provides an overview of the airfield performance of the BUING aircraft, highlighting three important factors: Balanced Field Length (BFL) Take-off Distance, and Landing Distance [2]. These parameters are analyzed at various elevations in relation to sea level in order to offer a comprehensive plot of the operational flexibility and limitations of the aircraft.

7.4.1 Balance Field Length

The RFP specifies 9,000 feet (2,743 meters) as the Balanced Field Length (BFL) that BUING must meet; however, BUING's BFL is 3,170 meters, which is greater than the RFP.

The given plot also shows operational capability at various airport altitudes, from Sea Level (blue line) to 1,500 meters above sea level (orange line). Multiple lines, indicating different airport elevations relative to sea level and deviation temperatures in Kelvin between ISA + $\Delta 0$ and ISA + $\Delta 20$, are shown in Fig. 7.3. These depictions provide an information of the aircraft's performance characteristics at various temperatures and altitudes.

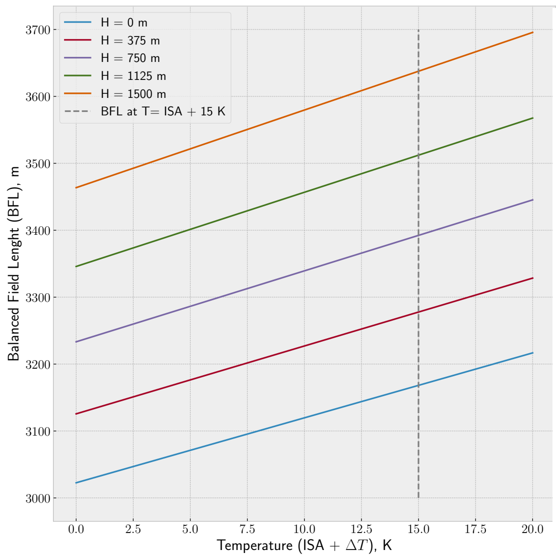

Figure 7.3: Balanced Field Length (BFL).

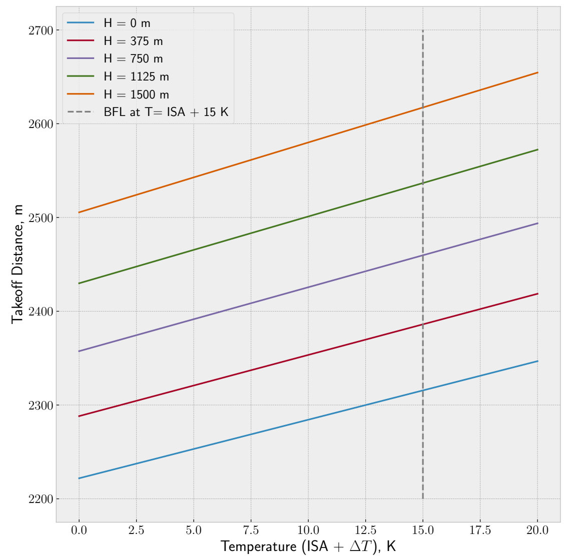

Figure 7.4: Take-off distance.

7.4.2 Take-off Distance

Fig. 7.4 provides an explanation of the takeoff distance characteristics of BUING aircraft at various heights and temperature variances. In particular, a takeoff configuration with a C_L of 2.5 is used to calculate the takeoff distance for BUING. The plot indicates that, given ISA + $\Delta 15$ circumstances, the computed takeoff distance for BUING is 2,611 m at Sea Level. The figure also shows the entire range of takeoff distances for different airport altitudes, from Sea Level to 1500 meters, and includes temperature variations from ISA + $\Delta 0$ to ISA + $\Delta 20$, respectively.

7.4.3 Landing Distance

Fig. 7.5 provides a plot representation of the BUING aircraft's landing distance using a landing configuration with 10% landing thrust. The landing distance for BUING is 630 meters. Furthermore, the figure illustrates the range of airport heights and the related temperature fluctuations shown in Kelvin units.

This plot representation, which takes into consideration important variables including thrust settings and atmospheric circumstances, offers insightful information about the performance characteristics of the BUING aircraft during the landing phase. The observed variations in airport temperatures and elevations highlight how crucial it is to take these factors into consideration when evaluating an aircraft's operational capability in various airfield conditions.

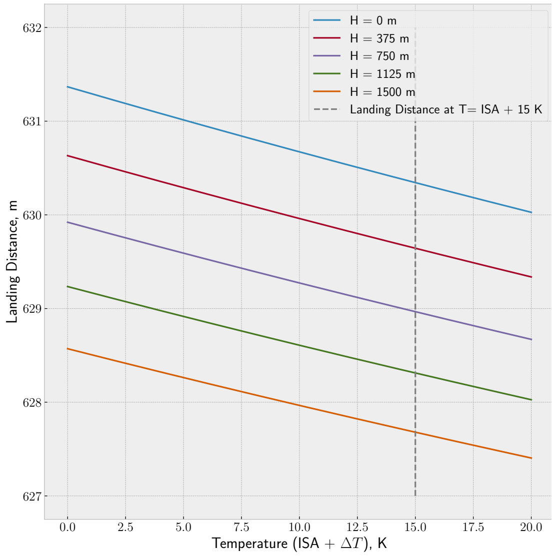

Figure 7.5: Landing distance.

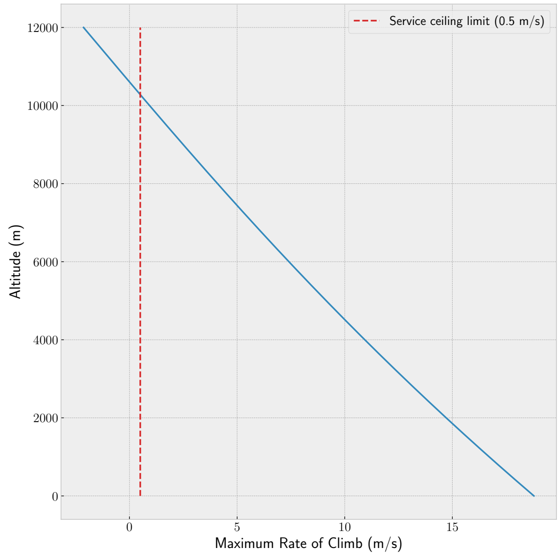

Figure 7.6: Service ceiling.

7.5 Service Ceiling

Maximum altitude at which an aircraft is able to maintain level flight is known as the ceiling altitude. Because of the lower air density and lower atmospheric pressure at higher altitudes, the airplane can run on less engine power, which saves fuel. This characteristic has a significant impact on fuel efficiency.

The maximum necessary service ceiling for any flight weight is defined in the Request for Proposal (RFP) to be at least 43,000 feet (13,106.40 m). With reference to Fig. 7.6, the BUING aircraft's service ceiling is 33707 ft (10,274 m) at a rate of climb of 0.5 meters per second and 75% of its maximum take-off weight (MTOW). The graphic provides a thorough picture of the aircraft's performance capabilities at altitude by further outlining distinct service ceilings associated with varying rates of climb.

CHAPTER 8 STABILITY

8.1 Empennage Design

The design of the empennage plays a significant importance role in the trim,stability and control of the aircraft. The empennage contributes significantly to longitudinal stability by counteracting pitching moments generated during flight and facilitating lateral and directional stability, crucial for maintaining straight and level flight. Given the typically larger wings and higher lift coefficients inherent in BUING designs, the empennage must effectively counteract the increased pitching moments and yaw in tendencies encountered during various flight phases, from take-off and landing to high-lift configurations.

The chosen tail configuration is an H-tail empennage configurations shown in Fig. 8.1 and it necessitates careful consideration of performance objectives, aerodynamic efficiency, and operational requirements. The H-tail configuration is also used by the largest cargo aircraft in the world, which is the AN-225 Mriya [18]. The H-tail empennage design stands as a cornerstone of stability engineering in aircraft design, offering a nuanced balance of longitudinal, lateral, and directional stability crucial for safe and predictable flight. By virtue of its configuration, the H-tail empennage enhances longitudinal stability through careful placement of horizontal stabilizers, strategically positioned behind the center of gravity. The H-tail design typically offers a larger usable cargo area between the horizontal stabilizers compared to other tail configurations [13]. This allows for greater flexibility in arranging and securing payloads of various sizes and shapes. In this case, the spacious cargo area between the horizontal stabilizers can accommodate the large dimensions of the M1 Abrams tanks and the numerous pallets, enabling efficient loading and securing of the cargo without compromising structural integrity. Moreover, the H-tail empennage

Table 8.1: Comparison stabilizer with similar.

Parameter	C-5 M Super Galaxy	AN-225 Mriya	BUING
CHT	0.20	0.15	0.5
CVT	0.05	0.10	0.08
LHT	12.19 m	13.72 m	12.95 m
LVT	9.14 m	10.67 m	9.88 m

design bolsters lateral stability by countering adverse roll tendencies. Through symmetric placement of horizontal stabilizers relative to the aircraft's longitudinal axis, the H-tail configuration effectively mitigates roll disturbances induced by asymmetric aerodynamic forces, such as those experienced during crosswinds or maneuvering. This inherent lateral stability fosters a wings-level orientation, reducing the need for continuous corrective inputs and promoting smoother, more stable flight trajectories.

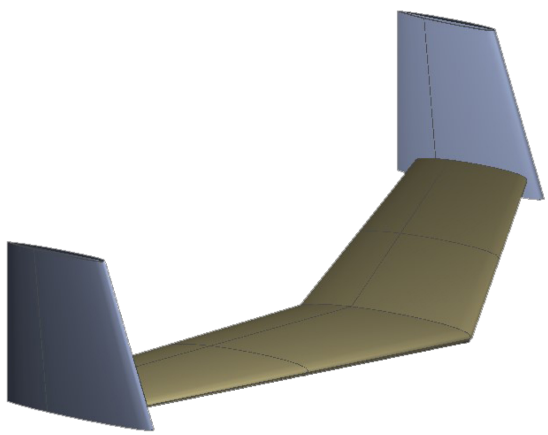

Figure 8.1: H-Tail design.

8.1.1 Stabilizer Sizing

To properly size the horizontal and vertical stabilisers, a thorough study of critical geometric characteristics was required, particularly volume ratios and moment lever arms between the tail aerodynamic centre and the aircraft's centre of gravity. Despite the availability of historical data on these factors, much of it had become obsolete. As a result, trade studies were conducted to determine the volume ratios and moment lever arms for both the horizontal and vertical stabilisers. Comparative tail sizing was performed to estimate tail volume ratios, and the moments arms of similar aircraft to BUING are shown in Table 8.1.

By using the Langley symmetrical supercritical airfoil with max thickness 11% at 40% chord it offers the BUING design a great advantage in achieving optimal aerodynamic, performance, especially in configurations where high lift coefficients and efficient low-speed operation are

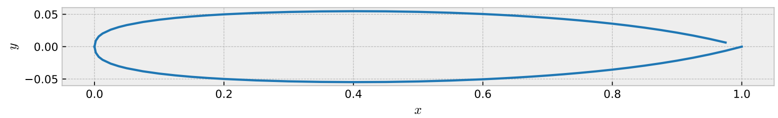

Figure 8.2: Langley symmetrical supercritical airfoil.

Table 8.2: Horizontal stabilizer parameters.

Parameter	Value
b	27 m
S_{HT}	162 m^2
λ	0.6
AR	4.50
V_{HT}	453.33 m^3
M_{GC}	6 m

paramount. The Langley SC airfoil is optimized for high Reynolds number performance and is known for its delayed shock wave formation and reduced wave drag at transonic speeds. The geometry of the airfoil is shown in Fig. 8.2.

The horizontal tail design parameter was constructed through a comparison study of sizing from other military cargo aircraft shown in Table 8.1. By angling the horizontal tail up, the aircraft improves its inherent stability against rolling motions. This is especially critical for heavy-lift aircraft, which frequently transport huge, heavy payloads. It was chosen to include a horizontal tail dihedral angle $\Gamma = 3°$, which offers a fair mix of stability and maneuverability. It reduces the destabilizing effects of side gusts and turbulence encountered during flight, allowing the aircraft to maintain a more regular and predictable attitude.

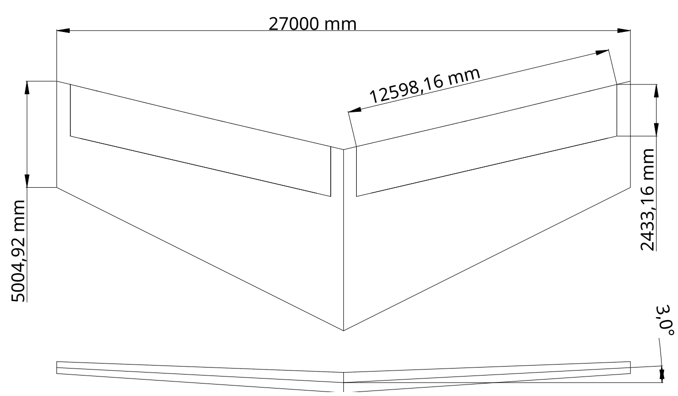

Figure 8.3: Geometry of the horizontal stabilizer.

Table 8.3: Vertical stabilizer parameters.

Parameter	Value
b	$8\,\mathrm{m}$
S_{HT}	$38\,\mathrm{m}^2$
λ	0.58
AR	1.68
V_{VT}	$9.13\,\mathrm{m}^2$
M_{GC}	$4.75\,\mathrm{m}$

8.1.2 Vertical Stabilizer

A preliminary design phase estimate of SVT was selected. This was repeated until the stability derivatives fell within Raymer's suggested ranges. This estimate was put to the test while figuring out where to place the engines on the wing so that the rudder could counteract yaw caused by an inoperable engine. A vertical tail area of $38\,\mathrm{m}^2$ was the consequence. The BUING vertical tail, which is essential for yaw stability and control, is carefully crafted to guarantee peak performance within the aircraft's operating limitations. The vertical tail, also known as the vertical stabiliser, prevents the aircraft from yawing or swinging side to side by providing stability in the yaw axis. Its dimensions and form are precisely that is shown in Fig. 8.4 to produce enough aerodynamic forces to offset yawing moments brought on by things like aircraft sideslip, crosswinds, and asymmetric engine thrust. The summary of the vertical tail parameter is shown in Table 8.3.

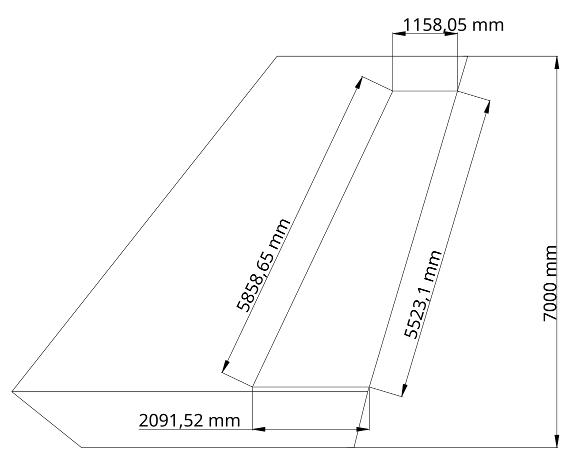

Figure 8.4: Geometry of the vertical stabilizer.

8.2 Control Surface Sizing

The BUING used a variety of control surfaces, including elevators, rudders, and ailerons, to maintain aircraft control. All of these controls were sized using Raymer's conceptual design technique [2]. All the sizing calculations are designed for a maximum deflection of 25 degrees for elevators, rudders, and ailerons. While maintaining the restriction of a maximum 25 degrees deflection for control surfaces, these proportions provide for steady flight and control authority. By having balance surface area and efficacy to obtain accurate handling characteristics, which are especially important while navigating difficult terrain or transporting large cargoes. Furthermore, moment lever arms are carefully chosen to retain aerodynamic efficiency while providing adequate control authority for both horizontal and vertical stabilizers. The scaled dimensional drawings of the control surfaces are shown in 8.4 and 8.3

8.3 Trim Analysis

The trim condition of an aircraft is an important part of longitudinal static stability, since it ensures that the aircraft can maintain a desired equilibrium state without continuous control inputs from the pilot. Longitudinal trim assessments were carried out at take-off, cruise, and landing conditions by solving the trim equations. The lift increment and pitching moment contribution from the flaps were considered during takeoff and landing. The pitching moment around the aerodynamic centre was modified for sweep, taper, and twist. Trim analysis charts were created for take-off, cruise, and landing, and are shown in Fig. 8.5. The goal is to achieve zero pitching moment about the centre of gravity during cruise without any tail angle of incidence.

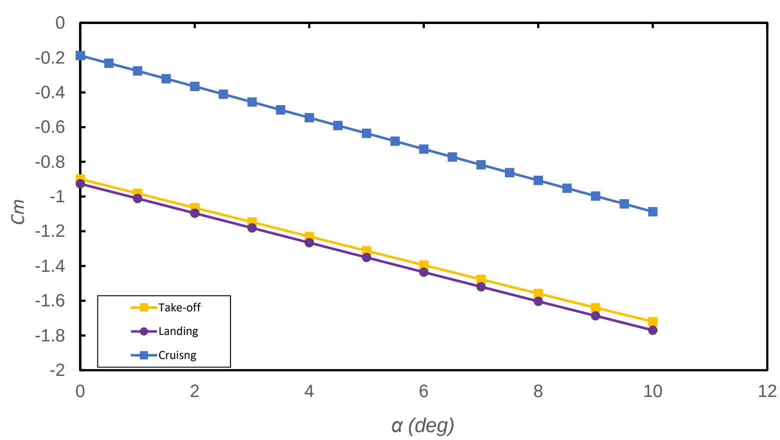

Figure 8.5: Trim diagram

8.4 Stability Derivatives

8.4.1 Longitudinal Stability Derivatives

The Longitudinal Stability and Control Derivatives play a critical role in defining the dynamic response and handling characteristics of the BUING design. These derivatives encapsulate the

Table 8.4: Longitudinal stability derivatives.

Derivative	Value
C_{M_α}	-4.5832
C_{M_q}	-27.864
C_{L_α}	4.9788
C_{L_q}	15.39

Table 8.5: Static margin and Neutral Point.

Parameter	Value		
Neutral Point	Static Margin	Forward CG	Aft CG
15.133 63 m	92.06%	37.91 m	26.88 m

aircraft's inherent stability, controllability, and maneuverability in longitudinal motion, encompassing parameters such as pitch stability, elevator effectiveness, and dynamic response to control inputs. The Longitudinal Stability and Control Derivatives are presented at cruising condition in the Table 8.4.

Since C_{M_α} is negative, the aircraft is longitudinally statically stable. The pitch stiffness (ratio of C_{M_α} to C_{L_α}) determines how stable the aircraft is, i.e. its static margin. Furthermore, with a forward CG of 37.91 metres and an aft CG of 26.88 metres, the aircraft has a significant static margin of 92.06%, shown in Table 8.5, ensuring a balanced and predictable response to flight inputs. Furthermore, the neutral point, located at 15.13 metres, demonstrates the great attention paid to aerodynamic balance. As the magnitude of pitch stiffness increases, the static margin increases. C_{M_q} determines how changes in pitch rate affect the pitching moment of the aircraft. From Table 8.4, it shows that negative C_{M_q} is essential to meet the short period damping requirement.

8.4.2 Lateral-Directional Stability Derivatives

The Lateral-directional stability and control derivatives are fundamental parameters that define the dynamic response and handling characteristics of the BUING design in roll and yaw motions. These derivatives encapsulate the aircraft's inherent stability, controllability, and maneuverability in lateral and directional motion, including parameters such as roll damping, yaw stability, and control surface effectiveness. These derivatives are presented at cruising condition in the Table 8.6.

A negative C_{l_β} implies static lateral stability. C_{l_p} is the roll damping derivative. It is necessary for C_{l_p} to be negative to meet roll handling requirements. A positive C_{n_β} implies static directional stability. Since C_{n_r} is the yaw damping derivative, it must be negative to meet yaw to meet handling requirements from [19].

Table 8.6: Lateral-directional stability derivatives.

Derivative	Value
C_{l_β}	-0.071015
Cl_p	-0.43424
Cl_r	0.082939
Cn_B	0.098659
Cn_p	-0.011236
Cn_r	-0.11697

8.5 Handling Qualities Analysis

Handling qualities represent the integrated value of those and other factors and are defined as "those qualities or characteristics of an aircraft that govern the ease and precision with which a pilot is able to perform the tasks required in support of an aircraft role and it encompass a multifaceted assessment of its dynamic response, controllability, and pilot interface, ultimately shaping the aircraft's ease of operation, maneuverability, and overall flight performance. The handling qualities are evaluated based on MIL-F4785B [19] standards for large heavy transport aircraft. Based on this, Level1 flying qualities are desired for the BUING.

8.5.1 Longitudinal dynamic Handling Qualities Analysis

The longitudinal dynamic flying qualities is to maintain a stable and predictable longitudinal motion during various flight conditions which often operate in demanding low-speed regimes and utilize high-lift devices for enhanced lift during take-off and landing, achieving adequate longitudinal dynamic stability is paramount for safe and efficient flight operations. This dynamic stability is crucial for maintaining a steady pitch attitude, especially during critical flight phases such as climb, descent, and transitions between high-lift and cruise configurations. The dynamic characteristic has been analyzed in XFLR5 [20], from which dynamic modes were determined as well as other characteristics. The Table 8.7 shows the Level 1 requirements for longitudinal flying qualities for MTOM at trim condition. The real number shows negative value, impliying that the disturbance is dynamically damped. This behaviour for short oscillation and phugoid modes are shown in Fig. 8.6. Here the analysis was made for the dynamic behaiour of pitch angle θ at three conditions, that is trim, take-off ($\delta_s = 15$ deg and $\delta_s = 30$), landing ($\delta_s = 15$ deg and $\delta_s = 40$). Note that the stable behaviour for landing and take-off configurations was achieved when the elevator was deflected at -20 and -25 degree, respectively.

Table 8.7: Longitudinal dynamic stability analysis.

Dynamic Mode	Roots	ω_n (Hz)	ζ
Phugoid	$-0.00042 + 0.05464i$	0.009	0.008
Short	$-1.601 + -3.761i$	0.6506	0.391

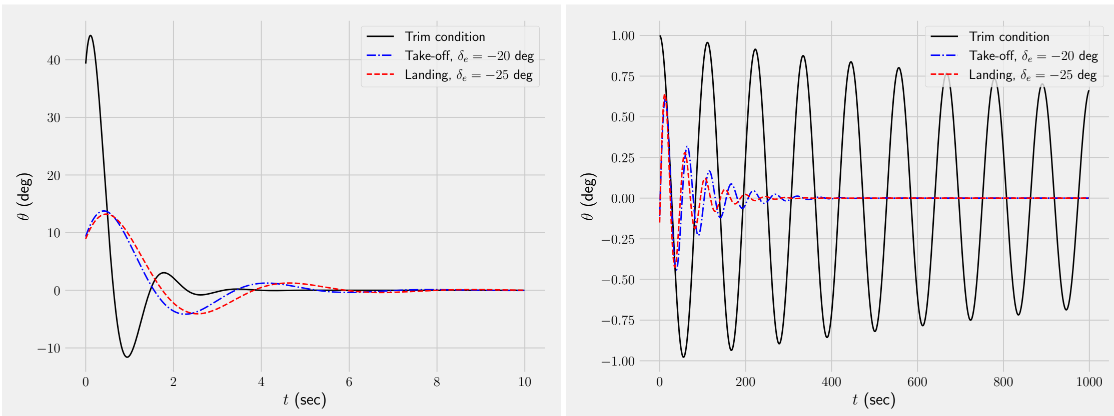

Figure 8.6: Time-variant θ for longitudinal modes. Left figure is short oscillation mode and right figures is phugoid mode.

8.5.2 Lateral-Directional Dynamic Stability Analysis

The lateral-directional dynamic stability is a pivotal aspect of flying qualities for BUING as a Heavy-Lift Aircraft (HLA), ensuring the aircraft's ability to maintain stable and predictable motion in roll and yaw axes during various flight conditions. It encompasses the aircraft's response to disturbances in roll and yaw, including its natural tendency to return to its trimmed condition following perturbations. A well-designed HLA should exhibit desirable dynamic stability traits in roll and yaw, including prompt response to pilot inputs, coordinated turns, and effective damping of oscillatory motions. Table 8.8 shows lateral-directional dynamic stability, has met level 1 requirements for lateral-directional flying qualities. Like the longitudinal mode, all the real number values are negative for MTOM at trim condition for roll, spiral, and dutch roll modes. Fig. 8.7 show the dynamic behaviour of roll angle ϕ for those three modes, compared with landing and take-off configurations when elevator are deployed at -20 and -25 degree. Only the spiral mode for take-off and landing configuration are unstable. Nevertheless, since it is a long-period mode, the condition is less catastrophic. The augmented control system can be used during those manuever.

Table 8.8: Lateral-directional dynamic stability.

Dynamic Mode	Roots	ω_n	ζ	T_2 (s)	τ
Roll	$-4.874 + 0.00000i$	-	-	0.142	0.205
Spiral	$-0.0001145 + 0.00000i$	-	-	6054.25	8734.43
Dutch Roll	$-0.1477 + -1.373i$	0.219Hz	0.107	-	-

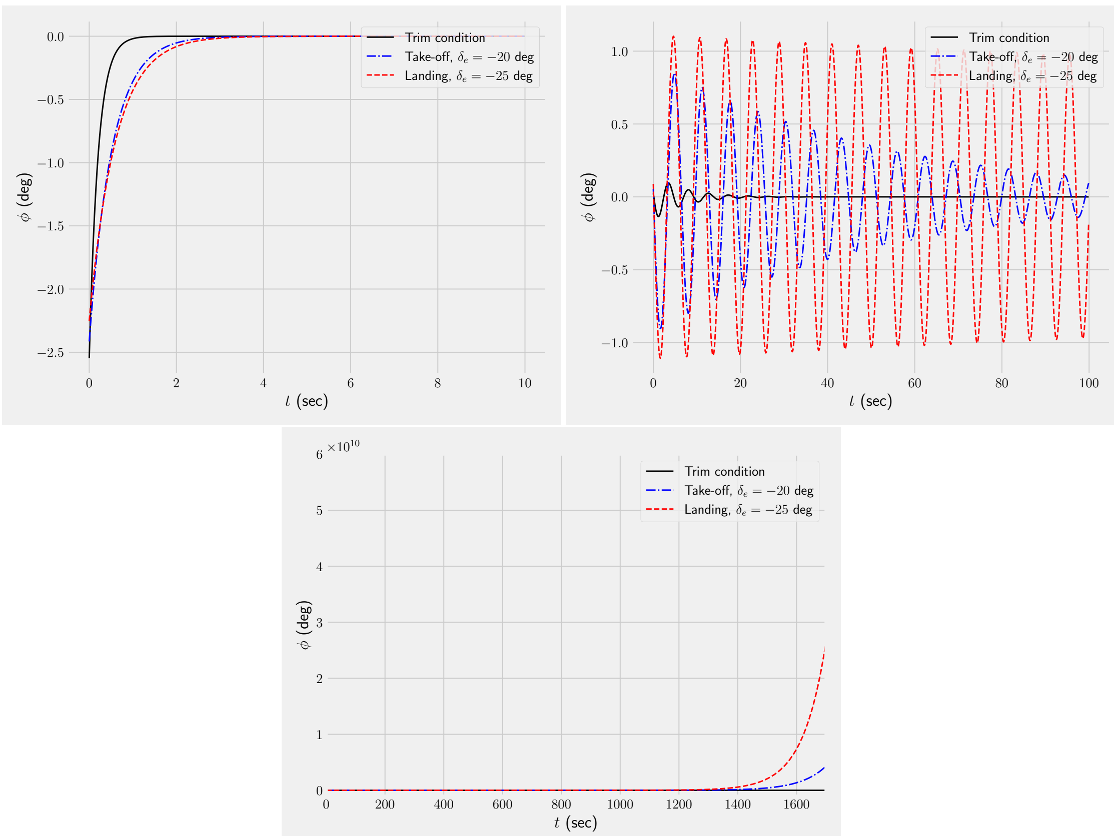

Figure 8.7: Time-variant ϕ for lateral-directional modes. Upper left figure is roll mode, upper right figures is dutch mode, and lower figure reprents spiral mode.

8.6 Weight Estimation

The concept "known weights" refers to parts and component that can either be weighed with reasonable accuracy or whose manufacturer (if the component is obtained from an outside vendor) can disclose the weight with reasonable confidence. Most of the time the weight analyst uses all three methods simultaneously, but known weights always supersede both the statistical and direct weight estimations. Engines, propellers, wheels, tires, brakes, landing gear struts, and standard parts(electronics, avionics, antennas, instruments, fasteners, etc.) are examples of components that will likely have published weights. The estimation weight techniques that are being used are Cessna's, Raymer's and Torenbeek's equations. From this three methods, Raymer's and USAF's have overestimated weight estimation, unlike Torenbeek's has the nearest weight estimation value. The breakdown weight estimations for all major fixed components are shown in Table 8.9. This data were used as the input to the XFLR5 model for the aerodynamics and stability analysis.

Table 8.9: Weight components.

No.	Component	Raymer (lb)	Torrenbeek (lb)	USAF (Ib)
1	Wing	127,318	106,042	165,481
2	Horizontal Tail	9,081	0	240,633
3	Vertical Tail	12,613	0	2,490
4	Emmpenage	21,695	23,796	60,260
5	Fuselage	42,866	0	197,116
6	Main Landing Gear	20,205	46,189	3,481
7	Nose Landing Gear	1,900	6,065	0
8	Nacelle	0	14,124	0
9	Engine Dry	79,559	79,559	79,559
10	Installed Engine	339,841	368,194	755,546
11	Fuel System	8,020	1,429	1,974
12	Flight Control System	160,960	6,769	18,067
13	Hydraulic System	6,974	1,080	1,080
14	Avionics Systems	3,086	3,086	3,086
15	Electrical System	1,454	134,538	973
16	Air Conditioning, Pressurization, and Antiicing	32,770	32,770	32,770
17	Furnishing	62,806	0	227
	Total Empty Weight	931,148	823,641	$1,608,751$

CHAPTER 9
COST ANALYSIS

In this chapter, we provide a concise summary of LCC costs and DOC. For a more comprehensive analysis and detailed calculations, please refer to the following link: `https://tinyurl.com/26wvyuxk`.

9.1 Life Cycle Cost (LCC)

Table 9.1 provides a summary of the development, test, and evaluation costs of BUING. This summary was derived using Nicolai's method [21], where the costing timeframe is set to 1998, resulting in all costs being converted to USD values of that year.

In this report, since avionics data price was not publicly available, the cost was computed using Raymer's method [2], which estimates the cost of avionics per unit mass in the year 2012. Additionally, this LCC calculation assumes the unit cost of the engine as given in [22]. An average annual inflation rate of 2% was assumed, with a total of 6 aircraft for flight tests and a production quantity of 90 aircraft for costing purposes

Table 9.1: The development, test, and evaluation cost.

Time frame for costing (Year)	1998
Annual Inflation Rate	0.02
Flight test aircraft number, QD (unit)	6
Production quantity for costing (unit)	90
Airframe engineering (USD)	3,553,538,672
Development support (USD)	730,705,244
Engines (USD)	420,095,625
Avionics (USD)	336,787,535
Manufacturing labor (USD)	1,504,460,505
Material and equipment (USD)	510,898,328
Tooling (USD)	1,639,201,363
Quality control (USD)	214,860,195
Flight test operations (USD)	177,178,899
Test facilities (USD)	0
Total DT&E Cost	9,087,726,366
Flight test aircraft (USD)	4,626,303,551

The flyaway cost is outlined in Table 9.2. These tables provide a breakdown of the flyaway cost for projected productions of 90, 180, and 270 aircraft. Amortization for each production number is set at 100%, indicating that the total cost for DT&E would be distributed across the entire projected production. To achieve a 10% profit margin, the unit price of the aircraft in 2022 may range from 480 million USD to 700 million USD, contingent upon the production quantity.

Table 9.2: Flyaway cost for nominal production of 90, 180, and 270 aircraft.

Number of nominal production	90	180	270
Engines	5,041,147,500	10,082,295,000	15,123,442,499
Avionics	5,051,813,024	10,103,626,048	15,155,439,072
Manufacturing labor (USD)	7,392,091,057	12,089,425,917	16,002,411,694
Material and equipment (USD)	4,446,634,130	7,736,675,180	10,696,736,056
Sustaining engineering (USD)	2,030,296,671	2,665,925,956	3,079,164,661
Tooling (USD)	1,759,522,353	2,405,257,589	2,847,607,988
Quality control (USD)	1,055,704,765	1,726,556,728	2,285,391,528
Manufacturing facilities (USD)	0	0	0
Subtotal for all aircraft for costing	26,777,209,500	46,809,762,417	65,190,193,498
Profit margin rate			0.1
Unit cost aircraft (USD)	297,524,550	260,054,236	241,445,161
Percentage of produced aircraft for amortization	100	100	100
Number of aircraft for amortization	90	180	270
Additional price per aircraft due ammortization (DTE Cost is given to N aircraft) (USD)	100,974,737	50,487,369	33,658,246
Final unit cost + Ammortization (USD)	398,499,287	310,541,604	275,103,407
Unit Cost + profit margin	438,349,216	341,595,765	302,613,748
Ajusted price to Y2022 (USD)	705,057,208	549,435,352	486,735,224

9.2 Direct operating cost

To gauge the direct operating cost of BUING, we employed the method outlined by Roskam [6]. Primary parameters' assumptions are detailed in Table 9.3, while the calculation summary is presented in Table 9.4. Roskam's method operates within a costing timeframe set to Year 1990, necessitating adjustments of all component costs to that year. The final DOC per flight hour was determined under the premise of operating a fleet comprising 90 aircraft.

Table 9.3: Parameters to calculate program cost (direct operating cost).

No	Parameter	Value
1	Time frame for costing (year)	1990
2	Factor of oil and lubricants	1.005
3	Flight hour/year	780
4	Block hour	11.35
5	FP (USD/gallon)	0.75
6	FD (lbs/gallon)	6.55
7	Number of crew	4
8	Crew ratio	1.5
9	Crew overhead factor	3
10	Maintenance manhours per flight hour	24
11	Indirect personnel cost factor	0.2
12	Spares cost factor	0.14
13	Depot cost factor	0.15
14	Annual inflation rate	0.02

As indicated in Table 9.4, the direct operating cost per flight hour amounts to approximately 66,000 USD in the year 2022. Detailed computations for deriving the DOC can be found in the spreadsheet linked above.

Table 9.4: Summary of the program cost (direct operating cost).

No	Cost Component	Y1990 USD	Y2022 USD
1	Fuel, oil, and lubricants	$19,719,784,064$	$37,162,733,537$
2	Direct personal, aircrews, and maintenance personnel	$2,842,184,937$	$5,356,212,884$
3	Consumable materials	$207,559,666$	$391,154,617$
4	Miscellany	$830,238,666$	$1,564,618,466$
5	Indirect personnel	$9,254,810,719$	$17,441,066,472$
6	Spares	$6,478,367,503$	$12,208,746,531$
7	Depot	$6,941,108,039$	$13,080,799,854$
	Total DOC	$46,274,053,595$	$87,205,332,361$
	DOC Per Flight Hour	$35,009$	$65,977$

BIBLIOGRAPHY

[1] GoComet. *The Critical Role Of Cargo Aircraft In The Logistics Industry - GoComet*. Mar. 2024. (Visited on 05/10/2024).

[2] Daniel P. Raymer. *Aircraft Design: A Conceptual Approach*. AIAA Education Series. Reston, VA: American Institute of Aeronautics and Astronautics, Inc, 2018. isbn: 978-1-62410-490-9.

[3] *Trent 1000*. https://www.rolls-royce.com/products-and-services/civil-aerospace/widebody/trent-1000.aspx. (Visited on 05/10/2024).

[4] "Rolls-Royce Trent 1000." In: *Wikipedia* (Mar. 2024). (Visited on 05/10/2024).

[5] "Rolls-Royce Trent." In: *Wikipedia* (Apr. 2024). (Visited on 05/10/2024).

[6] Jan Roskam. *Airplane Design*. Lawrence, Kan: DARcorporation, 2002. isbn: 978-1-884885-24-2.

[7] G. J. J Ruijgrok. *Elements of Airplane Performance*. 2009. isbn: 978-90-6562-232-7 978-90-6562-203-7 978-90-6562-204-4.

[8] *Online Materials Information Resource - MatWeb*. https://www.matweb.com/. (Visited on 05/12/2024).

[9] Michael Chun-Yung Niu. "Airframe stress analysis and sizing." In: *(No Title)* (2011).

[10] *Aerospace America May 2015: COMPOSITES VS. METALS*. https://www.omagdigital.com/article/COMPOSITES+VS.+METALS/1986792/254792/article.html. (Visited on 05/11/2024).

[11] Raghu Chaitanya Munjulury et al. "Knowledge-based flight control system and control surfaces integration in rapid." In: *Aerospace Technology Congress*. Vol. 2016. 2016.

[12] *Aircraft Door & Emergency Exit Types and Role ConsiderationsSasSofia*. https://sassofia.com/blog/aircraft-door-emergency-exit-types-and-role-considerations/. (Visited on 05/11/2024).

[13] Snorri Gudmundsson. *General Aviation Aircraft Design: Applied Methods and Procedures*. Second edition. Oxford Cambridge, MA: Butterworth-Heinemann, 2022. isbn: 978-0-12-818465-3.

[14] Harry W Slusher et al. "Aerial Refueling Equipment: Boom-Receptacle System and Interface Recommended Requirements." In: (2019).

[15] *14 CFR § 25.807 - Emergency Exits*. https://www.law.cornell.edu/cfr/text/14/25.807. (Visited on 05/11/2024).

[16] Mohammad H. Sadraey. *Aircraft Design: A Systems Engineering Approach*. Aerospace Series. Chichester: Wiley, 2013. isbn: 978-1-119-95340-1.

[17] Jack D. Mattingly, William H. Heiser, and David T. Pratt. *Aircraft Engine Design*. 2. ed. AIAA Education Series. Reston, VA: American Inst. of Aeronautics and Astronautics, 2004. isbn: 978-1-56347-538-2.

[18] "Antonov An-225 Mriya." In: *Wikipedia* (Apr. 2024). (Visited on 05/10/2024).

[19] *MIL-F-8785B (ASG), Military Specification Flying Qualities of Piloted Airplanes, August 7, 1969 | Archives and Special Collections*. https://archives.lib.purdue.edu/repositories/2/archival_objects/19000. (Visited on 05/10/2024).

[20] *Xflr5*. http://www.xflr5.tech/xflr5.htm. (Visited on 05/11/2024).

[21] Leland M. Nicolai and Grant Carichner. *Fundamentals of Aircraft and Airship Design: Aircraft Design*. Vol. 1. AIAA Educational Series. Reston, VA: American Institute of Aeronautics and Astronautics, 2010. isbn: 978-1-60086-751-4 978-1-60086-898-6.

[22] Alwyn Scott. "Japanese Airline ANA to Replace 100 Rolls Engines on 787s." In: *Reuters* (Aug. 2016). (Visited on 05/10/2024).